

**TECHNISCHE UNIVERSITÄT MÜNCHEN**

**Klinikum rechts der Isar**

**Fakultät für Medizin**

# **An innovative strategy in cancer treatment: microbeam and minibeam radiation therapy**

**Annique Cornelia Dombrowsky**

Vollständiger Abdruck der von der Fakultät für Medizin der Technischen Universität München zur Erlangung des akademischen Grades eines Doktors der Naturwissenschaften (Dr. rer. nat.) genehmigten Dissertation.

**Vorsitzende-/r:** Prof. Dr. Wolfgang Weber

**Prüfende/-r der Dissertation:**

1. apl. Prof. Dr. Thomas E. Schmid

2. Prof. Dr. Franz Pfeiffer

Die Dissertation wurde am 13.02.2020 bei der Technischen Universität München eingereicht und durch die Fakultät der Medizin am 06.10.2020 angenommen.



# Content

Abstract .....	V
Zusammenfassung .....	VII
1 Introduction.....	1
1.1 Conventional radiation therapy of cancer patients.....	1
1.1.1 The principle of conventional radiation therapy .....	1
1.1.1.1 Ionizing radiation is used for radiation therapy .....	1
1.1.1.2 Dose deposition profiles of X-rays and protons.....	2
1.1.2 Biological consequences of ionizing radiation .....	3
1.1.2.1 Biological effectiveness of X-rays and protons.....	5
1.1.3 Limitations of conventional radiation therapy .....	6
1.1.3.1 Therapeutic efficacy of conventional radiation therapy.....	7
1.2 Temporal fractionation as a therapeutic approach .....	8
1.3 Spatial fractionation as a therapeutic approach.....	10
1.3.1 The concept of spatially fractionated radiation therapy.....	10
1.3.2 Biological aspects of microbeam radiation therapy .....	10
1.3.3 Microbeam X-ray sources .....	12
1.3.3.1 Compact X-ray sources for MRT.....	14
1.3.3.1.1 The principle of inverse Compton scattering X-ray sources .....	14
1.3.3.1.2 Biological studies at compact X-ray sources for MRT .....	15
1.3.4 Proton minibeam radiation therapy .....	15
1.3.5 Therapeutic potential of spatial fractionation with X-rays and protons .....	17
1.4 Working hypothesis .....	19
2 Methods.....	20
2.1 Tumor growth delay assay in xenograft models .....	20
2.2 Histological examination of tumor xenografts.....	22
2.3 Immunohistochemical staining of $\gamma$ H2AX in tumor xenografts .....	23
2.4 Analysis of early side effects in irradiated skin .....	25

2.5	Analysis of late side effects in irradiated skin.....	27
3	Results .....	28
3.1	A proof-of-principle experiment for MRT at the Munich Compact Light Source.....	28
3.1.1	Aim and summary of the study .....	28
3.1.2	Contributions .....	29
3.1.3	Publication.....	29
3.2	Acute and late side effects after high-dose irradiation .....	40
3.2.1	Aim and setup of the study .....	40
3.2.2	Acute skin damage and late radiation-induced fibrosis and inflammation in murine ears after high-dose irradiation.....	40
3.2.2.1	Summary of the pilot study .....	40
3.2.2.2	Contributions .....	41
3.2.2.3	Publication .....	42
3.2.3	Normal tissue response depends on combined temporal and spatial fractionation of proton minibeam.....	64
3.2.3.1	Summary of the study .....	64
3.2.3.2	Contributions.....	65
3.2.3.3	Publication .....	65
4	Discussion and Conclusion.....	77
4.1	The Munich Compact Light Source as a new compact X-ray source for MRT .....	77
4.2	A mouse model for assessment of acute and late normal tissue complications after high-dose irradiation.....	79
4.3	Skin toxicity depends on spatial dose modulation and reirradiation accuracy after hypofractionated pMBRT .....	80
	Acknowledgments .....	82
	List of figures .....	83
	Abbreviations.....	84
	List of symbols.....	86
	References.....	87



## Abstract

Today, radiation therapy (RT) is a key role in cancer treatment. An innovative strategy in RT to further reduce radiation damage in the normal tissue is to spare parts of it from radiation – a method which is called spatial fractionation. The main objective of spatial fractionation is the increase of the therapeutic index of RT. This is achieved by the reduction of the irradiated volume of tissue which increases normal tissue tolerance as well as inhibits tumor growth. Currently, the X-ray microbeam radiation therapy (MRT) and the proton minibeam radiation therapy (pMBRT) are under investigation in radiobiological research.

Up to date, MRT is mainly performed at synchrotrons which have high space requirements, are cost-intensive and rarely distributed worldwide. Thus, there is only limited access for preclinical research of MRT and a prospective cancer patient's treatment. In order to overcome the synchrotron's disadvantages and to satisfy the technical requirements for MRT such as a high dose rate and a high brilliance, several compact X-ray sources were developed in recent years. The beamline at the Munich Compact Light Source (MuCLS) is an innovative compact X-ray source that generates X-rays *via* Compton scattering. First *in vitro* data showed an increased normal tissue-sparing after MRT at the MuCLS, while *in vivo* data has not been provided yet. In this doctoral thesis, the technical feasibility to inhibit tumor growth in a mouse ear tumor model was investigated after irradiation of either broadbeam or MRT at 3 Gy or 5 Gy, respectively, at the MuCLS. The results of this proof-of-principle experiment clearly demonstrated that it is technically feasible to irradiate mouse tumors with MRT at the MuCLS. Tumor growth was inhibited after broadbeam and microbeam irradiation. Thus, this proof-of-principle study introduces a novel compact X-ray source for MRT.

Using proton minibeam, several studies showed an increased sparing of the normal tissue. Therefore, pMBRT may be suitable to treat radioresistant tumors by the administration of high doses per fraction. The second part of this doctoral thesis addresses the question, which fraction size can be tolerated by the normal tissue, skin. By using the maximum tolerated dose of the skin in a mouse ear model, hypofractionated pMBRT was performed. The aim was to investigate whether the position accuracy of each fraction influences the severity of acute and late side effects. In a first pilot study, mouse ears were irradiated with four daily fractional X-ray doses from 0 Gy to 30 Gy. Acute side effects (ear thickness, erythema, desquamation) were assessed during the follow-up period of 90 days. At day 90, late side effects (collagen deposition, TGF $\beta$ 1 expression, chronic inflammation, hyperplasia, hair follicle loss) were investigated. In the second step, ear thickness and the amount of fibrotic tissue were examined in mouse ears which were irradiated with four daily fractions of pMBRT using three different fractionation schemes. These schemes differ in the reirradiation position and the dose modulation.

In summary, the X-ray pilot study demonstrated a maximum tolerated skin dose of 30 Gy per fraction. In addition, it showed that measuring the ear thickness can predict late side effects due to the dose-

dependency of acute and late side effects in the mouse ear model. Hypofractionated pMBRT provided evidence that both the reirradiation position and the dose modulation affect the severity of acute and late side effects. Despite an accurately delivered pattern with a high dose modulation is recommended, an inaccurately administered pattern of proton minibeam with a high dose modulation is superior to an accurately delivered pattern with a low dose modulation.

In conclusion, this doctoral thesis demonstrates that MRT and pMBRT could offer a completely innovative and promising way of radiation treatment.

## Zusammenfassung

Die Strahlentherapie (engl., *radiation therapy*, RT) spielt heutzutage eine entscheidende Rolle bei der Krebsbehandlung. Eine innovative Strategie in der RT die Strahlenschäden im Normalgewebe weiter zu verringern, ist die Reduktion der Strahlenexposition von Teilen des Gewebes. Diese Methode wird räumliche Fraktionierung genannt. Die Zielsetzung der räumlichen Fraktionierung ist die Erhöhung des therapeutischen Index der RT. Dies wird erreicht durch die Senkung des bestrahlten Volumens an Gewebe, was die Normalgewebetoleranz erhöht als auch das Tumorwachstum inhibiert. Im Moment stehen die Röntgen-Mikrostrahltherapie (engl., *microbeam radiation therapy*, MRT) und die Protonen-Minikanaltherapie (engl., *proton minibeam radiation therapy*, pMBRT) im Fokus der strahlenbiologischen Forschung.

Aktuell wird MRT hauptsächlich an Synchrotronen durchgeführt, welche hohe Anforderungen an Raum haben, kostenintensiv sind und weltweit nur gering verbreitet sind. Daher ist der Zugang für die präklinische Erforschung von MRT und für eine zukünftige Krebspatientenbehandlung nur limitiert möglich. Um die Nachteile von Synchrotronen zu überwinden und die technische Anforderung von MRT von einer hohen Dosisrate und hohen Brillianz zu erfüllen, wurden in den letzten Jahren mehrere kompakte Röntgenquellen entwickelt. Der Strahlengang an der Münchener kompakten Lichtquelle (engl., *beamline at the Munich Compact Light Source*, MuCLS) ist eine innovative kompakte Röntgenquelle, welche Röntgenstrahlen durch Compton Streuung erzeugt. Erste *in vitro* Daten zeigten, dass MRT an der MuCLS das Normalgewebe verstärkt schont, wohingegen *in vivo* Daten derzeit noch nicht zur Verfügung stehen. In dieser Doktorarbeit wurde die technische Durchführbarkeit einer Tumorwachstumsinhibition in einem Mausohren-Tumormodel nach Bestrahlung von homogenem Feld oder MRT mit jeweils 3 Gy oder 5 Gy an der MuCLS untersucht. Die Ergebnisse der Studie zeigten deutlich, dass es technisch machbar ist, einen Maustumor mit MRT an der MuCLS zu bestrahlen. Das Tumorwachstum wurde nach homogener Bestrahlung und MRT inhibiert. Damit führte diese Studie eine neue kompakte Röntgenquelle für MRT ein.

Bei der Verwendung von Protonen-Minikanälen zeigten mehrere Studien eine erhöhte Schonung des Normalgewebes. Deshalb könnte pMBRT für die Verabreichung von hohen Dosen pro Fraktion zur Behandlung von strahlenresistenten Tumoren geeignet sein. Im zweiten Teil dieser Doktorarbeit wird die Frage beantwortet, welche Fraktionsgröße von dem Normalgewebe, der Haut, toleriert werden kann. Die maximal tolerierbare Dosis der Haut in einem Mausohren-Model wird anschließend für die hypofraktionierte pMBRT verwendet. Die Zielsetzung war zu untersuchen, ob die Positionsgenauigkeit jeder Fraktionen den Schweregrad von akuten und chronischen Nebenwirkungen beeinflusst. In einer ersten Pilot Studie wurden Mausohren mit vier täglichen Röntgen-Fraktionsdosen von 0 Gy bis 30 Gy bestrahlt. Die akuten Nebenwirkungen (Ohrdicke, Rötung, Krustenbildung) über einen Zeitraum von 90 Tagen beobachtet. Am Tag 90 wurden die späten Nebenwirkungen (Kollagenablagerung, TGF $\beta$ 1 Expression, chronische Entzündung, Hyperplasie, Haarfollikelverlust) untersucht. In einem zweiten

Schritt wurden die Ohrdicke und die Menge an fibrotischen Gewebe in den Mausohren analysiert, welche mit vier täglichen Fraktionen von pMBRT in drei verschiedenen Fraktionierungsschemas bestrahlt wurden. Diese Schemas unterscheiden sich sowohl in der Bestrahlungsgenauigkeit und der Dosismodulation.

Zusammenfassend lässt sich sagen, dass die Röntgen-Pilotstudie eine maximale Toleranzdosis von 30 Gy pro Fraktion ergab. Zudem zeigte sie, dass die Messung der Ohrdicke späte Nebenwirkungen vorhersagen kann, weil sowohl akute als auch späte Nebenwirkungen eine Dosisabhängigkeit im Mausohren-Model zeigten. Hypofraktionierte pMBRT lieferte den Beweis, dass sowohl die Bestrahlungsgenauigkeit als auch die Dosismodulation den Schweregrad von akuten und späten Nebenwirkungen beeinflusst. Obwohl ein genau verabreichtes Muster mit einer hohen Dosismodulation zu empfehlen ist, ist ein ungenau verabreichtes Muster von Protonen-Minikanälen mit hoher Dosismodulation einer genauen Bestrahlung mit niedriger Dosismodulation vorzuziehen.

Schlussfolgend zeigt diese Doktorarbeit, dass MRT und pMBRT eine völlig neuartige und vielversprechende Art der Strahlentherapie darstellen können.

# 1 Introduction

## 1.1 Conventional radiation therapy of cancer patients

Cancer is one of the leading causes of death [1]. Half of all men and women will develop cancer during their lifetime with an increasing incidence over the next decades due to sociodemographic changes [2]. In Germany, approximately 25 % of people suffering from cancer will die [2]. The main cancer entities are breast, prostate, colon, and lung [2]. Malignant tumor's treatment typically involves surgery, chemotherapy and/or radiation therapy (RT) [1]. RT is applied for approximately 50 % of all cancer patients [1]. Therefore it is one of the main used treatment modalities [1,3]. RT is advantageous over surgery and chemotherapy because it is non-invasive and preserves the organ structure [4]. RT can be used for palliative management of cancer patients [3] but it contributes also towards 40 % of curative treatment [1]. Therapeutic radiation can be delivered from both inside and outside the patient referred to as brachytherapy and external-beam radiotherapy (EBRT), respectively [1]. In brachytherapy, a radioactive source is placed within or very close to the tumor treating small volumes with a heterogeneous dose distribution [5]. EBRT delivers radiation from conventional irradiators, e.g. electron linear accelerators (LINAC) [6]. It produces a homogenous (broadbeam, BB) dose to a large volume [5]. EBRT is the most commonly used modality for cancer treatment [1,7]. The overall aim of any RT is the destruction of tumor cells by delivering a maximum dose while sparing the normal tissue by delivering a minimum dose [1].

### 1.1.1 The principle of conventional radiation therapy

#### 1.1.1.1 Ionizing radiation is used for radiation therapy

Ionizing radiation (IR) describes the ability to eject an electron from an atom or molecule leading to ionization of the atom or molecule itself [8]. Moreover, IR deposits locally large amounts of energy which facilitates the break of chemical bonds between atoms [8]. IR can be subdivided into electromagnetic and particulate radiation [8].

Electromagnetic radiation includes X-rays and gamma rays, but also radio waves and visible light [8]. The latter two have longer wavelengths and thus lower photon energies [8]. That makes them incapable to break atomic bonds [8]. X- and gamma rays are only shortly penetrating [9]. They are able to induce a high degree of damage in biological structures close to the skin entrance [9]. In contrast, particulate radiation emitted by charged particles such as protons, neutrons and charged ions such as carbon [8] is able to induce a localized ionization or excitation of biological tissue [10]. Protons have high penetration power and produce a high degree of damage in deep tissue layers [8].

For local tumor treatment, most types of RT utilize IR in the form of X-rays [11]. X-rays were discovered by the German physicist Wilhelm Conrad Röntgen in 1895 [1]. Already one year later, X-rays were therapeutically implemented by Émil Grubbé who treated a cancer patient [12]. With the discovery of radium by Marie and Pierre Curie in 1898, the use of IR for cancer treatment gained more and more relevance in the late 19<sup>th</sup> century [12]. In addition to X-rays, EBRT is also carried out with particles such as protons [13] or carbon ions [1]. Despite the technological advantages in the last years, the equipment for the production of particle RT remains more expensive than for X-rays limiting their widespread clinical use [1].

In the following chapters, the focus is placed on EBRT with X-rays and protons.

#### 1.1.1.2 Dose deposition profiles of X-rays and protons

X-rays and protons exhibit different advantages and disadvantages for RT due to their different dose deposition profiles. The different spatial distribution of the physical dose of X-ray beams and proton beams is schematically illustrated in Figure 1. In this scheme, a tumor is located in a depth of 10 cm to 15 cm [14].

For RT using X-rays, the maximum energy (red color) is deposited close to the entrance surface (skin) [15] and thereby induces damages in plenty of healthy tissue cells in front of the tumor [6]. This can induce severe side effects in the patient [6]. With increasing depth into the tissue, the delivered dose of X-rays decreases almost exponentially reaching a low level in the depth of the tumor [6]. There is still an energy deposition behind the tumor [6]. For EBRT, clinical X-rays with an energy of 8 MeV were used having their maximum dose at a depth of 2 cm to 3 cm of soft tissue [6]. However, the energy at 25 cm is only about one-third of the maximum [6].

In contrast to X-rays, protons exhibit the inverted dose distribution profile of X-rays [6]. Protons deposit only a very low dose in shallow depths of the healthy tissue [13]. Then the dose increases dramatically to the maximum deposited energy at the so-called Bragg peak with a sharp dose fall-off afterward [13]. The range of protons in the patient's body is a result of the linear stopping power which is defined as the energy withdrawal *via* Coulomb interactions with electrons within the tissue [16]. The location of the Bragg peak can coincide with the tumor location according to the chosen energy of protons [13]. The use of monoenergetic proton beams is not desirable for RT due to the longitudinally narrow Bragg peak [17]. However, by the use of protons with different energies a spread-out Bragg peak (SOBP) can be generated enabling the dose coverage of the whole treatment volume [13]. Therefore, the use of protons allows a better conformal tumor treatment than X-rays [13].

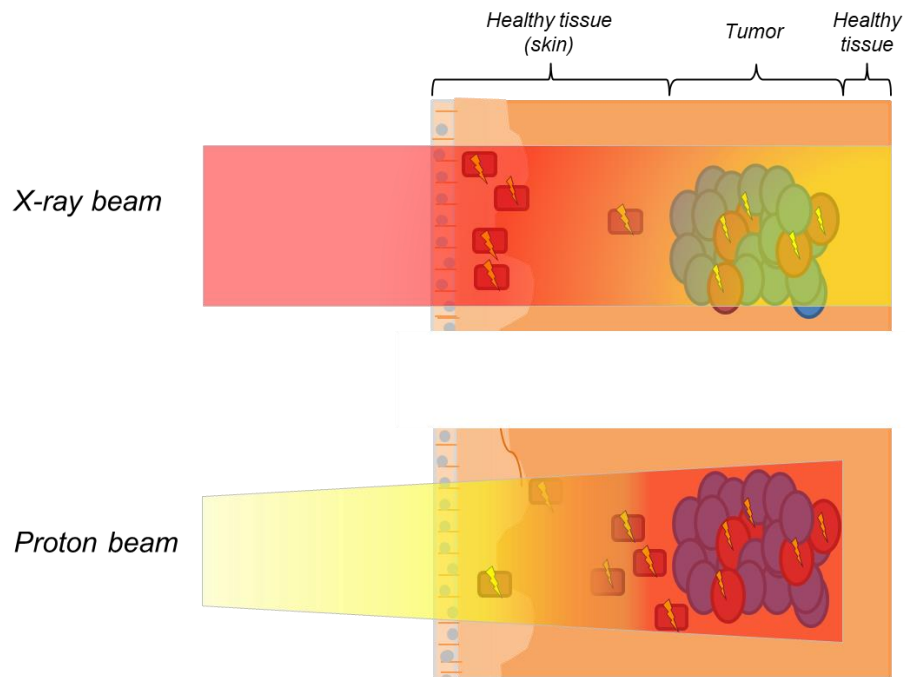


**Figure 1. Schematic illustration of the dose deposition profile of X-rays (top) and protons (bottom) in a tissue with a tumor (blue cells) located in a depth of 10-15 cm.** Radiation in the form of X-rays or protons is generated by an external source on the left (not shown). High radiation energy (dose) is depicted as red, medium energy is orange, and low energy is yellow. Radiation-damaged cells of the tumor and the healthy tissue are marked by a yellow flash.

### 1.1.2 Biological consequences of ionizing radiation

The main target of IR is the DNA, but also the RNA and proteins within a mammalian cell were hit [18]. Breaks of the DNA backbone are the most critical initiator of a biological effect [8]. They are the focus of this chapter.

Several biological effects can result from IR. IR produces a wide range of different DNA lesions such as base damages, DNA single-strand breaks (SSB), DNA double-strand breaks (DSB) and DNA crosslinks [18]. One Gray (Gy) of X-rays can induce  $10^5$  ionizations within the nucleus of mammalian cells [18] which forms about 40 DSBs, 1000 SSBs and 3000 damaged base pairs [19]. These DNA damages can be produced by either a direct or an indirect action leading to overall cell damage [18]. In the direct action, secondary electrons were formed after the absorption of radiation energy [8]. These secondary electrons interact with the DNA and produce a biological effect [8]. Charged particles operate dominantly *via* the direct action [8]. In the indirect action, secondary electrons interact with water molecules or other organic molecules within the cell and produce free radicals [8,10]. Free radicals such as hydroxyl (OH) or alkoxy groups are short-living and highly reactive due to their unpaired electron [10]. This unpaired electron reacts with other DNA molecules causing structural changes [10]. For OH radicals, structural changes can appear within a diffusion depth of 4 nm [18] which is twice the diameter of the DNA helix [8]. The indirect action is mainly performed by X-rays [8].

The radiosensitivity of cells depends on the cell cycle phase in which they are irradiated [20]. The cell cycle of mammalian cells consists of the G1 and the G2 phase for cellular growth, the S phase for DNA amplification, and the M phase for mitosis [21]. The G2 phase is a radiosensitive phase, followed by the G1 and the S phase with increasing radioresistance [22]. M-phase cells are the most sensitive ones [21]. Before entry into the M phase, different checkpoint inhibitors control the integrity of the DNA [21]. A cell cycle exit allows for the repair of possible radiation-induced DNA damages [21]. For fast proliferating cells such as tumor cells, many cells are in the M phase for cell division facilitating a higher radiosensitivity [21]. After irradiation, tumor cells keep on proliferation due to their lack of checkpoint inhibitors [23]. Their reduced repair capacity [23] leads to an accumulation of DNA damages which may culminate in tumor cell death [21]. For normal tissue cells, many cells arrest in a non-proliferation state (G0) making them highly radioresistant [21]. When radiation-induced damage is irreparable, normal tissue cells activate cell death pathways [21].

After radiation exposure, the fate of the irradiated cell depends on the efficiency of DNA repair mechanisms. DSBs are especially the most challenging radiation-induced aberrations [19] because they destabilize the genome more than SSBs [21]. If unrepaired, a DSB leads to cell death [24]. Therefore, their repair is essential for viability [19]. There are two different pathways for DNA damage repair: the homologous recombination (HR) and the non-homologous end-joining (NHEJ) [19]. HR requires an undamaged DNA template containing a homologous DNA sequence, e.g. on a sister chromatid [25]. HR occurs predominantly in the S and the G2 phase of the cell cycle [25]. In contrast to HR, NHEJ is conducted independently of a DNA template and the cell cycle phase [25]. However, it is especially important in the G1 phase [26]. NHEJ has an increased susceptibility to error repairing of radiation-induced DNA damages [25].

A misrepair of the DNA damage can result in a viable cell harboring genomic instability which in turn may lead to a malignant transformation [25] followed by carcinogenesis. Alternatively, a misrepaired or unrepaired DNA damage can lead to cell death *via* the generation of lethal chromosome aberrations or the direct induction of apoptosis [25]. If the DNA damage is adequately repaired, the cell survives and continues proliferation into daughter cells without chromosomal changes [25]. An accurate repair of DNA damages is more prevalent in normal tissue cells owning efficient repair mechanisms [1]. Contrary to that, malignant tumor cells developed mechanisms to bypass DNA damage repair mechanisms such as HR or NHEJ [1]. A fail of DNA repair mechanisms in tumor cells leads to an accumulation of DNA mutations followed by cancer cell death [1].



As a result, cycling tumor cells are more sensitive against IR than normal tissue cells [20]. There is a dominant killing of tumor cells which makes RT advantageous over other treatment modalities [20]. In summary, the cell cycle phase and the ability to activate repair mechanisms determine the effectiveness of RT. The radiation dose needs to be high enough to induce a sufficient amount of irreparable DNA damages in malignant cells in order to eliminate the tumor [11]. In addition, the radiation dose needs to be low enough to induce only a reasonable sublethal amount of DNA damages in normal tissue cells allowing efficient repair and ongoing proliferation without chromosomal changes [11].

#### 1.1.2.1 Biological effectiveness of X-rays and protons

The biological effectiveness of IR depends on the number of ionization events [8]. It can be differentiated between sparsely and densely IR [8]. Sparsely IR is referred to as a low number of well-separated ionizing events while densely IR describes a high localized number of ionizing events [8]. The density of ionization in radiation tracks is described by the linear energy transfer (LET) [15]. Sparsely IR (or low LET) has a low probability to cause a DSB [8]. In contrast, densely IR (or high LET) produces DSBs with a high probability [8]. Examples for low LET are protons and X-rays and for high LET heavier ions such as carbon [27].

The ionizing potential of X-rays and particles is directly correlated with the biological effectiveness: the more ionizing events are produced, the more the LET rises, the more cell killing is generated per Gray [15]. However, there is maximum biological effectiveness when radiation has a LET of 100 keV/ $\mu\text{m}$  because of the coincidence between the diameter of the DNA helix and the average separation of ionizing events [8].

The kind of DNA damage also depends on the LET and therefore determines the biological effectiveness. Low LET radiation induces DNA damages by the indirect way of interaction with biomolecules (as described in chapter 1.1.2) [28]. Therefore, only simple DNA damages such as a single DNA lesion within a few turns of the DNA helix appear [28]. The direct way of action is primarily done by charged particles with a high LET [8,28]. They can directly deposit their energy into the tissue generating more complex and clustered DNA damages such as DSBs, SSBs, oxidative clustered lesions, or base damages [28]. Complex DNA lesions are difficult to repair resulting in a higher biological effectiveness of high LET radiation [29].

The relationships between the number of ionizing events, LET, DNA damage and biological effectiveness are depicted in Figure 2. X-rays and protons are the focus of this doctoral thesis. Calculating their relative biological effectiveness (RBE), protons and X-rays demonstrate almost the same biological effect with an RBE of 1.1 [27]. However, in the last years, proton's RBE of 1.1 is being questioned regarding new models which suggest a higher RBE at the SOBP [27].

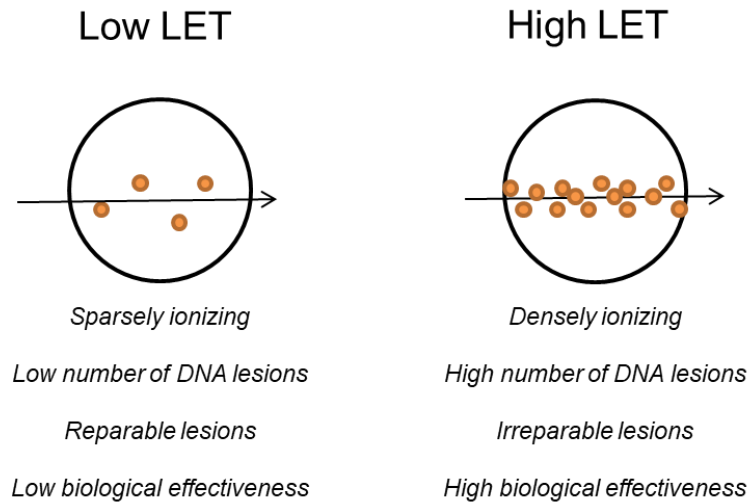


**Figure 2. Illustration of the biological effectiveness of radiation in dependence of their linear energy transfer (LET).** On the left, low LET radiation produces sparsely ionizing events that generate only a low number of reparable DNA lesions. Therefore it has a low biological effectiveness. On the right, high LET radiation ionizes densely the matter within a cell producing a high number of irreparable DNA lesions which lead to a high biological effectiveness.

### 1.1.3 Limitations of conventional radiation therapy

Radiation treatment of cancer patients is mostly hampered by undesired side effects [30]. This is justified by the delivery of unacceptable radiation doses to the normal tissue which lies in the beam track [30]. The normal tissue is capable of repairing radiation-induced damages by efficient repair mechanisms [19,31]. However, when DNA damages are irreparable, normal cells go into cell death [19,31]. This radiation-induced morbidity of normal tissue cells limits the delivered dose to the tumor and hence hinders the efficacy of RT in controlling tumor growth [11]. As a consequence, the aim of any RT schedule is to achieve the best possible therapeutic outcome while harming the normal tissue as little as possible [31].

Radiation-induced tissue injury can be classified into two categories: (1) early and (2) late side effects. Early side effects manifest transiently after a few weeks while late side effects establish possibly irreversibly after 6 months to years after completing the RT [4,32].

Early side effects are expressed as erythema and desquamation of the skin, mucositis, nausea, and diarrhea [4]. Months after high doses of IR patients develop also fibrosis, atrophy, vascular or neural damage with a high probability [4]. These late toxicities are the most crucial side effects because they dramatically influence the quality of life of cancer patients [4].

Fibrosis as a dense and excessive accumulation of collagen and other fibers is characterized by a reduced tissue flexibility and a restricted motion of joints [4]. The key regulator of fibrosis is the cytokine TGF $\beta$  [4] which promotes the activation, proliferation, and differentiation of fibroblasts into myofibroblasts [33]. Myofibroblasts are able to produce excessive amounts of collagen [33].

A further concern about RT is the radiation-induced secondary malignancy [34]. During the treatment course, radiation-induced mutations can accumulate in normal tissue cells enabling the transformation of a normal cell into a malignant tumor-forming cell in the patient's body [34]. Irradiated cells that possess DSB are the most vulnerable to malignant transformation [34]. Secondary malignancies are of high interest because of the increased life expectancy of cancer survivors whose number continues to rise [34]. RT accounts only for approximately 5 % of the total treatment-related secondary malignancies [34]. Nowadays, about 18 % of cancer survivors develop a secondary malignancy after surviving the primary treated tumor [34].

#### 1.1.3.1 Therapeutic efficacy of conventional radiation therapy

Monitoring of late toxicities is crucial in assessing the therapeutic benefit of treatment because of the irreversibility of late side effects [32]. The therapeutic benefit is measured by using sigmoidal dose-response curves [32]. Both the probability of tumor cure and the likelihood of developing normal tissue toxicities increase with increasing total radiation dose [32]. Dose-response curves for normal tissue responses have a threshold at low doses which produce no reaction, and at high doses, which produce the maximum toxic reaction [32]. A sigmoidal shape of dose-response curves was also observed for tumor tissue which responds earlier to an applied dose leading to a shift of the curve to lower doses [32].

The therapeutic benefit can be determined by the therapeutic index, which is expressed by the ratio of the median toxic dose to the median effective dose [35]. The difference between the tumor control dose and the tissue tolerance dose is described by the therapeutic window [15]. With respect to a dose-response curve, the maximum radiation dose which is tolerated by the normal tissue and achieves a reasonable tumor response can be fixed [15]. With an increased distance between both curves for tumor control and normal tissue response, the therapeutic window widens and consequently the therapeutic benefit for the patient increases [15]. However, radioresistant tumors such as glioma respond only to higher doses than their radiosensitive counterparts, leading to close proximity of both dose-response curves for tumor control and normal tissue complications [36]. A reduction of the therapeutic window can also occur, if radiosensitive normal tissues, such as the spinal cord, are exposed which surround the tumor target [36]. These narrow therapeutic windows of conventional RT demand a radiation technique with increased normal tissue-sparing which allows the widening of the therapeutic window [36].

## 1.2 Temporal fractionation as a therapeutic approach

In history, radiation was usually delivered as large single-dose exposures [12]. As a result, the tumor cure rate was unsatisfying and the severity of side effects extremely high [12]. The first revolutionary experiment was conducted by Claudius Regaud in 1911 showing the sterilization of ram's testes after

three irradiations in an interval of 15 days [12]. He did not observe the desquamation of the skin which was a surprising result compared to single-dose irradiations in this time [37]. Afterward, dose fractionation evolved by empirical clinical experiments [37]. In 1920, the first cancer patients were cured with fractionated radiotherapy (XRT) [12]. This was the breakthrough of XRT bringing it into the clinic [12]. By the 1960s standard clinical dose fractionation varied widely between different treatment centers [37]. They lasted between 3 and 8 weeks [37]. Nowadays, XRT uses typically daily fractions of 1.2 Gy to 3 Gy delivered over several weeks [12]. They result in a reduced level of normal tissue complications [12]. Multi-fractionated delivery of IR can be grouped into two more treatment schedules: (1) hyperfractionation and (2) hypofractionation. In contrast to conventional XRT giving one fraction per day, five days a week, over 3-7 weeks [38], hyperfractionated schedules consist of smaller fractional doses and an increased number of fractions per day usually 6 h apart [12]. Hyperfractionation is defined as 0.5 Gy to 2.2 Gy given in two fractions per day, 2-5 days a week, for 2-4 weeks [38]. Hypofractionation applies higher doses per fraction (3 Gy to 20 Gy) given for 1-3 days [38].

The use of hypofractionation gained more interest in the last years since conventional XRT showed a low rate of 20 % to 30 % of erased tumor growth [39]. Sometimes tumors even regrew again [39]. High fractional doses were delivered e.g. in stereotactic body RT allowing a great dose-volume sparing [40]. Hypofractionation is suitable for the treatment of tumors lying in sensitive regions because side effects such as catastrophic neurological complications can be avoided [41]. Hypofractionation maximizes also the local tumor control [40]. Tumor eradication is mediated by an increased infiltration of immune cells, e.g. cytotoxic T cells in colon cancer [42]. This increased immunity does not occur in hyperfractionated regimes [43]. In the United States, the abundance of hypofractionation increased from 6 % to 14 % within 9 years [44]. Also, the combination of hypofractionated regimes and protons with a pivotal dose deposition profile is under investigation, e.g. for prostate cancer [44].

In general, the advantageous effect of XRT is the reduced total lethality of normal tissue cells around the tumor when single doses were subdivided into multiple fractions [20]. This normal tissue-sparing effect can be explained by the four Rs of radiobiology:

- (1) Repair of sublethal cellular damage in normal tissue [12]
- (2) Repopulation of normal tissues with healthy cells which migrate into irradiated areas [12]
- (3) Redistribution of tumor cells from radioresistant (S phase) into radiosensitive (G2-M phase) phases of the cell cycle [12]
- (4) Reoxygenation of hypoxic (radioresistant) areas of the tumor [12].

Temporal fractionation is subject to the principle that the repair of injured normal tissue cells occurs between two fractions [39]. The repair capacities of normal tissues are considered to be different depending on their proliferation statuses [8]. Therefore, normal tissues can be subdivided into two groups: (1) Highly proliferative tissue and (2) slowly proliferative tissues. Highly proliferative tissues such as skin, hair, mucosae or intestinal epithelium react within a few days [8,37]. They are called early responders [8,37]. The central nervous system (spinal cord), bones, and kidney proliferate slowly and hence respond only after months or years [8,37]. They are called late responders [8,37].

The repair capacity influences also the dose given within a certain time which is required to compensate for proliferation (repopulation) [8]. The total time of XRT is conventionally between 6 and 8 weeks [8]. This is not long enough to trigger proliferation in late-responding tissue (low sparing effect) but it is able to induce repopulation in early-responding tissues (large sparing effect) [8]. This sparing effect can be directly assigned to the radioresistance of cell cycle phases [8].

Early-responding tissues are composed mainly of rapidly proliferating cells equally distributed in all cell cycle phases with a huge portion of S phase cells [8]. Late-responding tissues possess mainly slowly proliferating cells which are in the early G1 or the G0 phase [8]. Cells in S, G0 or G1 phases are considered to be radioresistant [21,22]. Cells in radiosensitive phases were selectively damaged and leave cells in more radioresistant cell cycle phases behind [37]. Exemplarily, one cell of the early-responding tissue in the S phase is alive after irradiation due to radioresistance producing new daughter cells [8]. Meanwhile, other cells are in more radiosensitive phases of the cell cycle and are killed by the dose fraction [8]. These dead cells were replaced by the fast proliferating cells which were in the S phase before. Therefore, the early tissue stays intact and less radiation-induced damage occurs. For late-responding tissues, a high amount of radioresistant G0 and G1 phase cells survive the dose fractions while some cells in radiosensitive phases were killed. These cells were slowly replaced by cells in the G0/G1 phase. Consequently, this leads to high radiation-induced damage in late-responding tissues. Normal tissue cells proliferate at equal rates which keeps them synchronized [8]. In contrast to normal tissues, tumor cells are also fast proliferating cells that cycle at highly variable rates [37]. Therefore, they become asynchronized [37] and are consequently more prone to cell death.

In conclusion, the overall time and fraction size need to be optimized according to the sparing of tissues with respect to their repair capacities [8]. Moreover, by dividing a single dose into multi-fractions the normal tissue can be spared due to time for repair of sublethal damage and the triggering of repopulation between the fractions [8]. It can also abrogate tumor growth because of reoxygenation and reassortment of cells into radiosensitive cell cycle phases between the fractions [8]. XRT widens the therapeutic window.

## 1.3 Spatial fractionation as a therapeutic approach

### 1.3.1 The concept of spatially fractionated radiation therapy

Spatially fractionated RT delivers a single high-dose fraction by subdividing a large treatment area, as commonly used in conventional RT, into several smaller fields [45]. There are two different kinds of spatially fractionated RT depending on the size of the irradiated field: (1) microbeam radiation therapy (MRT) and (2) minibeam radiation therapy (MBRT) [46]. Both approaches use an array of planar, quasi-parallel beams [47] in order to deliver an inhomogeneous dose profile with steep dose gradients [45]. The inhomogeneous dose profile composes of regions with high doses (*peak region*) and regions with low doses (*valley region*) [46]. The peak region is generated by beams with a width of 25  $\mu\text{m}$  to 100  $\mu\text{m}$  in MRT, and 500  $\mu\text{m}$  to 700  $\mu\text{m}$  in MBRT [36,46]. Each micro- or minibeam delivers a maximum dose ( $\geq 100$  Gy [48]), which is named the *peak dose* [48]. The dose between the beams, the so-called *valley dose* [48], is created by the scattering of X-rays and secondary electrons from the neighboring peak regions [49]. Valley doses are typically below the tissue tolerance dose [50] of 5 Gy to 20 Gy [51]. Spatially fractionated RT can also be characterized by the *center-to-center (ctc) distance*, which describes the spatial separation of two adjacent beams, and the *peak-to-valley dose ratio (PVDR)*, which gives the ratio between the peak dose and the valley dose [48]. The ctc distance is normally between 100  $\mu\text{m}$  and 400  $\mu\text{m}$  in MRT [49], and 600  $\mu\text{m}$  and 3 mm in MBRT [46,52]. The PVDR ranges usually between 10 and 100 [53]. It is determined by the physical parameters of the collimator used for generating the micro-/minibeam pattern (beam width, ctc distance, collimator thickness, collimator surface) [51]. Moreover, the PVDR depends on the spectrum of the radiation modality [54], the depth in the target [54], the composition of target material [41] and the amount of scattering material [55].

Several MRT and MBRT experiments have been conducted either theoretically or experimentally with deuterons [56,57], X-rays [52], oxygen [58], carbon ions [58] and protons [48,59]. In the following chapters, MRT using hard X-rays with an energy higher than 10 keV [60] and MBRT with protons are further discussed.

### 1.3.2 Biological aspects of microbeam radiation therapy

Historically, the concept of MRT can be traced back to GRID therapy invented by the German radiobiologist Alban Köhler in 1909 [61]. He applied X-rays with an energy of 50 keV to 150 keV onto a grid of iron wires which targets a tumor region with millimeter-wide X-ray beams [61,62]. Back then, one of the main risks of RT was extensive radiation damages in the skin and subcutaneous tissue [63]. Köhler's GRID therapy was able to reduce these side effects after irradiation of deep-seated tumors [63] with a field size of 1  $\text{cm}^2$  [48].

Investigating the relation between treatment volume and tissue tolerance, Zeman *et al.*, (1959) transferred the GRID therapy to a microscopic scale [57]. They found out that the mouse brain tolerates much higher doses of 11,000 Gy when the deuteron beam has a thinner diameter of 25  $\mu\text{m}$  as if 300 Gy are delivered in a 1000  $\mu\text{m}$  wide beam [57]. This experiment revealed for the first time the dose-volume effect which is still a matter of intensive research. The dose-volume effect says that the tissue tolerance increases when the field size is decreased [48]. In 1992, Slatkin and coworkers suggested a therapeutic intent of the microbeam-based approach [64].

In MRT, the combination of spatial fractionation and sub-millimetric fields increases the normal tissue tolerance [48] as observed by the group of Laissue in 1995. They found that skin entrance doses up to 5,000 Gy do not induce brain tissue necrosis [62]. A tissue-sparing effect has also been observed *in vitro* [51]. A few years later, Laissue *et al.* highlighted the second benefit of MRT. MRT can extend the survival of tumor-bearing rats after irradiation using 25  $\mu\text{m}$  wide beams [65]. This can be attributed to the inhibition of tumor growth *in vivo* [66-68]. The anti-tumor efficacy was confirmed for different tumor entities such as the brain [67-74], breast [75] and squamous epithelium [76]. Moreover, these findings indicate that the biological effect of MRT is different in normal tissue and tumor tissue [63] which allows the increase of the therapeutic index [70].

Some biological mechanisms conveying the increased therapeutic efficacy of MRT are suggested but not understood in all details:

- (1) Preferential damage of immature, disordered blood vessels in the tumor compared to mature, structured vessels in the normal tissue [66]
- (2) Differential modulation of the immune system within the tumor compared to that in the normal tissue [77]
- (3) Improved regeneration of the normal tissue due to communication between irradiated and unirradiated neighboring cells (Bystander effect) [78]
- (4) Hyperplasia and migration of normal tissue cells in the valley region replace lethally injured cells within the peak region [79]

The high therapeutic efficacy of MRT can be attributed, at least partly, to the destruction of blood vessels. Normal vessels possess a mature and intact structure while tumor vessels show an immature and chaotic structure without the periendothelial layer [66]. Additionally, similar-sized vessels are homogeneously spread over the normal tissue in contrast to a heterogeneous arrangement of vessels in the tumor with different diameters [80]. In addition, the high peak doses of MRT can only transiently increase the permeability of blood vessels in the normal tissue [81]. A fast recovery of these blood vessels occurs [81]. In contrast, tumor vessels along the microbeam track are damaged leading to a lack of oxygen and nutrients within the tumor which cumulates into shrinkage of the tumor [66,82].

The second hypothesized mechanism of MRT suggests an impact on the immune system. This is based on the finding that MRT changes the expression of many different genes involved in tumor immunity and inflammation [83]. This MRT-mediated gene expression differs from the gene expression of homogeneously irradiated tumors [83]. A differential gene expression was also observed between tumors and normal tissues after MRT [77]. However, the total number of modulated genes after MRT is lower in tumors (1.8 %) than in normal tissues (5 %) [77]. The immune profile of mammary tumors was extensively studied. The number of immune cells infiltrating the mammary tumor vary between BB and MRT [84]. There was a high number of T cells after MRT and high numbers of both neutrophils and macrophages after BB [84]. The number of eosinophils is not increased while eosinophil recruiting molecules are differentially regulated after MRT and BB of mammary tumors [85]. Both direct effects of MRT can also be accompanied by an indirect effect, also referred to as the radiation-induced bystander effect (RIBE). RIBE is conducted *via* soluble cytokines or a direct cell-cell-communication [78] between neighboring irradiated and unirradiated cells [86]. This communication takes place over a distance of up to several millimeters *ex vivo* [87]. As a response to RIBE, apoptosis, reactive oxygen species (ROS) [88] or micronuclei can be induced in normal tissue [89]. RIBE is also detected in out-of-field organs *via* the transfer of signals through the blood [90].

The therapeutic efficacy of MRT can be optimized by varying different physical parameters. In order to achieve the best combination of normal tissue-sparing and tumor growth inhibition, the group of Slatkin compared three different beam widths (25, 50, 75  $\mu\text{m}$ ) and achieved the best compromise at 50  $\mu\text{m}$  [73]. Moreover, the PVDR determines the biological effectiveness of MRT and MBRT [91]. The PVDR should be as high as possible in the normal tissue [92]. This means the valley dose should be kept slightly below the tissue tolerance dose [91]. The PVDR should be as low as possible in the tumor so that the valley dose can inhibit the DNA repair mechanisms [91]. This implies that the valley dose is also a critical determinant for normal tissue-sparing [92]. The valley dose determines the cell survival between the beams and preserves the tissue architecture [69]. As an example, a valley dose below the threshold dose of 45 Gy avoids moist desquamation [75].

### 1.3.3 Microbeam X-ray sources

The therapeutic efficacy of MRT is based on the delivery of high peak dose regions alternated with low valley dose regions [46]. A prerequisite for this dose inhomogeneity is a sharp dose fall-off between peak and valley regions generating a high PVDR [93]. Critical parameters of radiation sources required to achieve a high PVDR are:

- (1) High dose rate [36,47]
- (2) X-ray energies <200 keV [93]
- (3) Low beam divergence [94].



The use of a high dose rate is necessary in order to avoid detrimental blurring of microbeams due to cardiovascular movements [95]. This is an issue especially for narrow microbeams [93]. Moreover, respiratory motion can cause a 50 % decrease in the PVDR at low dose rates [53]. However, extremely high dose rates are difficult to achieve with conventional X-ray tubes [96].

The energy of X-rays influences the degree of lateral scattering of secondary electrons and the penetration depth. The threshold energy of X-rays for MRT is set to 200 keV [93]. Beam energies higher than 200 keV scatter highly laterally [36] and have a high penetration depth [97]. A High lateral scattering of secondary electrons leads to an increase of the beam penumbra [96]. In addition, the valley dose increases which lowers the PVDR and spares the normal tissue [98]. As an example, 200 keV X-rays increase the thickness of 30  $\mu\text{m}$  wide beams by an additional 30  $\mu\text{m}$  [99]. Due to these dose tails extending into the valley regions beam energies higher than 200 keV are unacceptable for MRT [93,100]. Beam energies below 200 keV show a low lateral scattering [41] but penetrate only in shallow depth of the irradiated tissue [36]. A low lateral scattering leads to a sharp dose fall-off [41]. However, a low penetration depth limits the dose delivery to the tumor [46,93] and constrains the treatment to superficial tumors situated in a depth of 2 cm to 6 cm under the skin [101,102]. Nevertheless, energies below 200 keV are a good compromise between penetration depth and sharpness of the photon beam penumbra [55]. Beam energies of 200 keV can be produced by the most conventional orthovoltage tubes but not by clinically used megavoltage X-ray tubes such as the LINAC [96].

Currently, only synchrotron radiation facilities fulfill the criteria for MRT of a high dose rate [103] and a minimal beam divergence [102] which results in an ultra-high flux [104]. The European synchrotron radiation facility (ESRF) produces an X-ray spectrum with energies between 50 keV and 500 keV and has a mean energy of 100 keV [91]. Dose rates of synchrotrons vary between 20 Gy/s and 100 Gy/s at the National Synchrotron Light Source (NSLS) [75,105] and 8 kGy/s to 16 kGy/s at the ESRF [103].

Although synchrotrons provide all the required beam properties for MRT, only a few centers exist worldwide [47]. The reasons for that are high construction costs [106], high maintenance costs [95] and the need for large areas [95], due to a high circumference [107]. As an example, the circumference of the ESRF is about 800 m [107]. Due to these disadvantages, the performance of MRT with synchrotron-generated X-rays is very limited. MRT is currently only available in preclinical studies at 3<sup>rd</sup> generation synchrotrons sources [102] such as the NSLS, the ESRF and the Australian Synchrotron [108]. In order to get a widespread application of MRT in medicine and science, new attempts have been made for building up an X-ray source which makes MRT available in a more room-sized and cost-effective way.

### 1.3.3.1 Compact X-ray sources for MRT

In 2013, Hadsell and coworkers built a carbon nanotube (CNT) X-ray source which delivers 2 Gy/min of 160 kVp X-ray microbeams to the target [104]. Shortly afterward, several groups published compact X-ray sources addressing also the issues of synchrotrons:

- (1) A French group published the concept of an inverse Compton scattering source (ICS), the ThomX machine [109].
- (2) Bartzsch *et al.* developed a collimator that can be incorporated into a conventional X-ray tube [110].
- (3) The group of Pfeiffer characterized the performance of the beamline of the Compact Light Source in Munich in Germany (MuCLS) [111].
- (4) Bartzsch *et al.* invented the concept of a line focus X-ray tube (LFXT) [95].

#### 1.3.3.1.1 *The principle of inverse Compton scattering X-ray sources*

The ICS or the Compact Light Source (CLS) is an emerging compact X-ray source. The inverse Compton scattering process describes the collision of a high-energetic electron beam and a low-energetic laser pulse [111]. This leads to the backscattering of the laser beam as hard X-rays [109]. Other concepts of compact X-ray sources use high-field magnets and synchrotrons use permanent-magnet undulators [109]. In contrast to that, laser undulators are installed at the ICSs which enables them to produce electron energy in the range of keV [109,111]. It allows also to scale down the circumference of the electron storage ring from several hundreds of meters, as in synchrotrons, to a few meters [109,111]. The concept of the inverse Compton scattering is utilized in the ThomX machine in France [109] and the MuCLS [111].

The MuCLS was installed in April 2015 at the Technical University of Munich [111]. It was originally manufactured and provided by Lyncean Technologies Inc., USA [111]. On the example of MuCLS having a size of  $2 \times 7 \text{ m}^2$  [112], a total flux of  $9.6 \times 10^9$  photons/s and an X-ray energy between 15-35 keV [111], an ICS allows the performance of MRT at a room-sized X-ray source. The technical features of the MuCLS are comparable to that of the ThomX machine producing X-rays with an energy of 80 keV and a flux of  $10^{12}$ - $10^{14}$  photons/s [109]. Both ICSs produce X-ray energies which are slightly below but in the range of the mean energy of synchrotron-generated X-rays of 70 keV to 120 keV [48,69]. However, the dose rates of 1 Gy/min at the MuCLS [112] and 0.5 Gy/s at the ThomX [109] are quite lower as achieved at synchrotrons with ultra-high dose rates [103]. The flux of synchrotrons is in the range of  $10^{14}$  photons/s [95] which is higher compared to ICSs such as the MuCLS with a flux of  $10^{10}$  photons/s [111,112]. However, the reduced costs and low space requirements [112] of an ICS are advantageous over large and expensive synchrotron radiation facilities.

### 1.3.3.1.2 Biological studies at compact X-ray sources for MRT

So far, biological studies using MRT were conducted at only two novel compact X-rays sources: (1) the CNT X-ray source and (2) the MuCLS. In comparison to studies at synchrotrons characterized by a higher dose rate and consequently a high peak dose, the biological effects of MRT were reproduced, at least partly, at compact X-ray sources. Irradiation of glioblastoma-bearing mice at the CNT X-ray source showed that MRT can slightly reduce tumor growth at low peak doses of 48 Gy [113,114]. Furthermore, it can significantly shrink the tumor at higher peak doses of 72 Gy to a similar extent as conventional BB at 10 Gy [113,114]. At the MuCLS, so far only *in vitro* experiments were performed. Burger *et al.*, (2017) observed an increased sparing of normal tissue cells suggested by a lower number of chromosome aberrations after MRT compared to BB at the MuCLS [112]. However, an *in vivo* trial was not performed at the MuCLS up to now.

### 1.3.4 Proton minibeam radiation therapy

A counterpart of X-ray MRT is X-ray MBRT which was proposed for the first time by Dilmanian *et al.* in 2006. It has been shown that unilateral MBRT using 680  $\mu\text{m}$  wide X-ray beams was well tolerated by the healthy brain tissue [93]. Therefore, X-ray MBRT seems to have a similar tissue-sparing effect as X-ray MRT [91]. Furthermore, MBRT is superior to MRT in dose rate and X-ray energy. Since minibeam possess an increased field size [48]), a high dose rate can be used which is not possible with microbeams [48]. Consequently, the increased dose rate reduces the risk of beam blurring from heard pulsation [91]. In addition, MBRT allows the use of highly penetrating photon energies [91]. For MBRT, Prezado *et al.*, (2009) recommended the double X-ray energy of 350 keV to 400 keV as it is used in MRT [91]. MBRT using 400 keV achieves the lowest entrance dose in the normal tissue when the same integral dose within the tumor is deposited as for lower beam energies [46,91]. The reason for that is the higher penetration depth of 400 keV X-rays [91]. They can be generated at specially tailored X-ray machines without the need for synchrotrons [91].

While spatially fractionated RT can be applied using X-rays, also proton microchannel radiation therapy (pMRT) or proton minibeam radiation therapy (pMBRT) can be performed. Protons exploit multiple Coulomb scattering [115], which means that proton beams get wider when they pass through the tissue [14]. With increasing depth in tissue and in proximity to the tumor the broadening proton beams merge and produce a solid beam [14]. Simulations of the dose profile of pMBRT showed a uniform dose within the tumor (brain) and a well-segmented dose in the normal tissue [115]. The homogenous dose delivery to the tumor leads to a comparable tumor control rate as conventional proton RT [14]. In addition, the spatial fractionation of pMRT in shallow tissues (skin) is similar to X-ray MRT, suggesting the maintenance of the tissue-sparing effect [14,59].

pMRT is based on the principles of the proton sieve pattern irradiation from 1972 [116]. *In vitro* studies showed a significant reduction of inflammatory markers and cytogenetic damage, and an enhanced viability of the normal skin compared to BB X-ray treatments [14] and homogenous proton irradiation [117]. In addition, the sparing of 3D skin tissue was in a similar range for pMRT and X-ray MRT with regard to viability and genetic damage [118].

The teams around Yolanda Prezado and Günther Dollinger published the concept of pMBRT [14,48]. pMBRT is able to achieve PVDRs very similar or higher than normally used in X-ray MRT [48]. First *in vivo* data confirmed that sub-millimetric proton beams abrogate the normal tissue toxicity in the skin [119]. This experimental study used the mouse ear as a measure of the normal tissue-sparing effect [119]. The mouse ear has a thickness of around 250  $\mu\text{m}$ , is easily accessible and therefore allows to quantify early side effects such as redness (erythema), ear swelling (thickness, inflammation) and the formation of a crust (desquamation) [119]. Next, investigation of the tissue damage in each tissue layer on the way to the tumor in a theoretical model of a tumor treatment demonstrated a correlation between the maximum ear thickness and the diameter of proton minibeam [120]. Tissue damage depends on the increasing proton beam size with a threshold beam diameter of 1 mm [120]. Beam diameters  $>1$  mm increase dramatically the ear thickness and the skin score (sum score of desquamation and erythema) [120]. The use of beams in the sub-millimeter range ( $<1$  mm) at the skin entrance is suggested [120]. Furthermore, proton beams arranged as hexagonal or quadratic pencil beams produce the highest sparing of normal tissue in the entrance channel [121]. Compared to these arrangements, the tissue-sparing effect of planar beams was lower but still more pronounced than BB radiation [121].

While the previously mentioned studies considered only the tissue toxicity and set homogenous dose coverage of the tumor as a prerequisite, the effectiveness in tumor shrinkage of pMBRT was evaluated only by Prezado *et al.* in 2018. The group confirmed the tumor regression in 22 % of irradiated tumor-bearing rats after inhomogeneous tumor irradiation using pMBRT [122]. They questioned the paradigm of the necessity of a homogeneous tumor dose coverage [122]. At the moment, the literature discusses controversially whether a homogeneous tumor irradiation is necessary for tumor ablation [14,122]. However, tumor response after an inhomogeneous dose distribution within the tumor seems to be even as effective as a homogenous dose distribution [122]. This debate is also valid for X-ray MBRT keeping the microbeam pattern when passing the tissue, leading to an inhomogeneous dose coverage of the tumor.

### 1.3.5 Therapeutic potential of spatial fractionation with X-rays and protons

The treatment of radioresistant tumors, tumors close to radiosensitive organs and tumors in children is still compromised despite both the reduction of the dose to organs-at-risk and the tumor dose conformation have notably improved by technical progress in the last years [122]. Therefore, novel treatment strategies such as MRT and MBRT were rediscovered at the turn of the century. Even back then, MRT and MBRT were known to dramatically increase the tolerance of normal tissues [62,123] accompanied by an effective tumor growth inhibition [66,68,80]. Because of this, MRT and MBRT are suggested to increase the therapeutic index [47,66,75,122] as indicated by a study of Dilmanian *et al.*, (2002) showing a 5-fold higher therapeutic efficacy of MRT than BB [69]. This was also shown for pMBRT by Prezado *et al.*, (2018).

In the future, spatial fractionation could be used for cancer treatment of children and young adults [107] in which the sparing of the normal tissue is even more important than in adults. Moreover, MRT and MBRT allow for the deposition of an extremely high dose within radioresistant tumors [91]. Brain tumors such as glioblastoma, which are radioresistant and one of the most aggressive tumors [122], are especially in the focus of MRT [36,46,62,70,73,80,81,124] and pMBRT research [122]. Other research groups suggest superficial tumors in organs such as skin, breast, and bone as potential targets of MRT [107].

In order to achieve cancer treatment in clinical practice, multi-fractions of MRT delivered from multiple ports are supposed to optimize the valley doses to tolerable doses for normal tissue and even toxic doses for the tumor [50]. This is achieved by cross-fired/interspersed or interlaced microbeams [107] which were introduced by Bräuer-Krisch *et al.*, (2005), and Dilmanian *et al.*, (2006). Both approaches differ in the production of a solid beam within the tumor. The method suggested by Bräuer-Krisch *et al.* crossfires thin (25  $\mu\text{m}$ ) microbeam arrays from two lateral directions without producing a solid beam within the tumor by halving the beam spacing [50]. With this, outside the tumor, the valley dose remains below the tissue tolerance dose but the valley dose exceeds this dose (small PVDR) within the tumor exerting a tumoricidal effect [50]. Tumor ablation was more effective in cross-planar treated animals than in unilateral treated ones suggesting a higher therapeutic index of cross-planar MRT [75].

In contrast to the cross-fired approach, interlaced MRT uses thicker beam widths of 680  $\mu\text{m}$  [93] or 950  $\mu\text{m}$  [41]. Irradiation from two orthogonal ports allows for the accurate delivery of a homogeneous dose (solid beam) to the target (tumor) [93]. It maintains simultaneously the dose inhomogeneity (non-interlaced beams) in the surrounding normal tissue [93]. The utilization of interlaced arrays is also termed “microradiosurgery” [41]. First *in vivo* experiments showed that the low valley dose of interlaced beams with a thickness of 680  $\mu\text{m}$  [93] and 950  $\mu\text{m}$  [41] still preserves the sparing of the brain tissue [93]. This study could not show any evident tumor cell killing [93]. However, the coworkers of Prezado *et al.* figured out that interlacing beams of 640  $\mu\text{m}$  are able to increase the

lifespan of tumor-bearing rats at four different doses, respectively, compared to unilateral MBRT at peak doses up to 180 Gy and corresponding valley doses up to 16 Gy [36]. Increasing the number of ports from two to four produces highly confined damage in the brain and at the same time a sparing of the unilaterally irradiated normal brain [102]. Similar attempts were also made for proton beams achieving a homogeneous dose inside target volume by the cross-fired approach [125].

Furthermore, temporal fractionation is a key part of clinical RT. Contrary to the previously mentioned studies in which fractions from different ports were applied on the same day [36,68], the question raises what happens, if MRT or MBRT were applied consecutively on different days. In 2009, Serduc *et al.* investigated the lifespan of tumor-bearing animals after applying three daily fractions of X-ray MRT trilaterally [73]. They irradiated animals perpendicularly on the first day [73]. On the second day, animals were treated in an anteroposterior direction, and on the third day, they were placed vertically, perpendicularly to the beam [73]. In each fraction, animals were exposed to 50 microbeams with a width of 50  $\mu\text{m}$  leading to overlapping arrays in the target volume [73]. As a result of this trial of a combined spatial and temporal fractionation, the survival of tumor-bearing animals was significantly extended by 216 % compared to untreated animals [73]. However, tumors were not completely ablated [126]. In line with this, hypofractionated regimes of pMBRT were suggested in 2015 which allow the delivery of ultra-high doses and increase the benefit of the tissue-sparing effect in proximal tissues [127]. So far, no trial was conducted investigating the side effects in the normal tissue after hypofractionated irradiation of MRT or MBRT.

A further approach published in 2018 is spiralMRT. SpiralMRT irradiates the target continuously with one single microbeam while the target is moved spirally (rotated or/and translation along the rotation axis) [128]. The advantages of spiralMRT include the reduction of the entrance dose due to an increase of the overall beam entrance surface [128]. Additionally, spiralMRT is less sensitive against cardiosynchronous movements of the target volume regarding microbeam blurring and complete irradiation of all parts of the target [128]. One step forward to clinical implementation is the motion-guided microbeam irradiator to minimize the motion-induced beam blurring of thin microbeams at low dose rates at the compact X-ray source [53].

## 1.4 Working hypothesis

Spatial fractionation by MRT and MBRT conveys an increased tolerance of the normal tissue and ensures an even more efficient tumor growth inhibition as conventional RT. This allows for the delivery of high doses to the tumor with less concern about clinical side effects. Therefore, X-ray MRT and pMBRT play an especially pivotal role in current studies. However, the clinical widespread of X-ray MRT is hampered because of the limited accessibility to synchrotrons for preclinical studies as well as for future clinical trials worldwide. Therefore, the radiobiological examination of MRT is restricted to compact X-ray sources with the potential for higher availability. One part of the presented work is the investigation of the tumoricidal effect of monochromatic X-ray MRT at the beamline of a compact X-ray source, named Munich Compact Light Source (MuCLS). Based on previous studies at the MuCLS, the tissue-sparing effect could be confirmed *in vitro* [112] as obtained at synchrotrons [51]. Furthermore, recent literature suggests also a tumoricidal effect at alternative compact X-ray sources [113,114]. Therefore, this thesis demonstrates the first *in vivo* study at the MuCLS investigating the MRT-mediated growth inhibition of head and neck cancer which was subcutaneously implanted into mouse ears.

In the literature, the superior role of protons over X-rays in cancer treatment is controversially discussed because of their cost intensity and their advantageous dose deposition profile lowering the normal tissue damage proximal and distal to the tumor. Therefore, pMBRT enables the use of a temporally hypofractionated regime which could enable an increased benefit of the normal tissue. The second part of this doctoral thesis addresses the question, if the benefit of the skin from fractionated pMBRT might depend on the reirradiation accuracy of each fraction. For comparison of different fractionation schemes, acute and late side effects were monitored for a period of 150 days. As a prerequisite, a dose-response curve was established delivering four high-dose X-ray BB fractions daily to healthy mouse ears. Ear swelling, erythema, and desquamation were assessed as acute side effects, while chronic side effects such as fibrosis and inflammation were histopathologically quantified 92 days post-irradiation.

## 2 Methods

### 2.1 Tumor growth delay assay in xenograft models

The tumor growth delay (TGD) assay is one of the most popular endpoints of cancer RT [129] for comparing the anti-tumor efficacy of different treatment modalities [130]. It represents the difference in tumor volume doubling time between treated and untreated individuals [129]. The volume of untreated tumors increases rapidly at a relatively uniform rate from injection on [8]. Irradiation of tumors at low doses of IR leads to a temporary tumor retardation [8]. Afterward, the treated tumor regrows again [8] at a similar regrowth rate [129] or lower than that of their untreated counterparts [131]. Comparing the differential growth behavior of treated and untreated tumors, the growth delay equals the time (in days) after treatment which is necessary for the treated tumor to regrow to a specified size, e.g. to the 5-fold size which was irradiated before [8]. TGD assay usually starts at a tumor size of approximately 50-200 mm<sup>3</sup> [130] or a diameter of 2-4 mm in mice [8] and ends at a volume of 1.5 to 2 cm<sup>3</sup> [130].

Another important endpoint of *in vivo* tumor radiobiology is the tumor control (TCD<sub>50</sub>) assay which determines the dose (tumor control dose 50%, TCD<sub>50</sub>) at which 50 % of the tumors are locally controlled in their growth [8]. Since the TCD<sub>50</sub> assay depends on the inactivation of clonogenic cells (cancer stem cells) [15,132], recurrent tumor growth can be traced back to the clonal expansion of one single cell [133]. This contrasts the TGD assay which measures the bulk killing of non-clonogenic and clonogenic cells [15]. The TGD assay does not guarantee a controlled tumor growth because only one survived clonogenic cell can lead to a tumor regrowth [134]. In order to determine the mean curative radiation dose (TCD<sub>50</sub>) [133], tumors of equal size were grouped and irradiated with graded doses ranging from low doses, which slightly inhibit tumor growth, to large doses which induce a local tumor control [8]. The TCD<sub>50</sub> assay represents the gold standard assay as it is the most clinically relevant assay for curative cancer RT [15]. However, the TGD assay is the most frequently used approach in therapeutic studies [135] because it is standardized, less labor-intensive and cost-effective [15]. In many instances, the results of the TGD assay are in line with TCD<sub>50</sub> studies [136].

For studying the anti-tumor efficacy of treatment modalities, there is a variety of mouse models available which include syngeneic models, genetically engineered mouse (GEM) models and xenograft models [130]. The syngeneic tumor model reflects a mouse tumor growing in a mouse of that strain in which the tumor originally grew and from which it was isolated [130]. The main advantage of syngeneic models is the immune competency [130] reflecting the interaction between tumor cells and a fully competent immune system [137]. However, tumors are not as chronically inflamed and not as genetically complex as human tumors [137]. This is because of the rapid growth of syngeneic tumors and a lower tumor mutation burden [137]. Moreover, the homology between



mouse and human is limited [130] because the murine and the human immune system differ [137]. Therefore results from syngeneic mouse models do not recapitulate human clinical data hampering the transferability to clinical settings for humans [130]. The syngeneic model costs low and is reproducible [130]. However, due to its low human relevance, syngeneic models were replaced widely by GEM or human xenograft models [137].

The second approach studying anti-tumor therapies is the GEM model which develops spontaneously cancer in an orthotopic tumor site due to the introduction of one or more genetic mutations [137]. The GEM models reflect the carcinogenesis with an intact and fully competent immune system and they have still a non-human like immune system [137]. Moreover, it recapitulates the whole human genetic complexity [137] and a more physiologically relevant tumor microenvironment (TME) [137]. However, GEM models are highly time-consuming and expensive with unexpected phenotypes [137].

In xenograft models, human tumor cells rise to tumors within a murine environment resembling a histology similar to that of the parent tumor in the donor patient [130,135]. A prerequisite for the human tumor establishment in mice is an immune deficiency which avoids the rejection of foreign cells [138]. In contrast to syngeneic models, xenograft models reflect the genetic complexity of human tumors while their main disadvantage is the lack of the immune system [137]. However, the absence of immune reactions in xenograft models simplifies the complex situation in immunocompetent humans or animals [137]. Furthermore, the human TME, e.g. stromal components, can also not totally be reproduced in complexity by xenograft models [137] since it is still rodent and leads to non-species-specific interactions [137]. Therefore, it is less realistic for human settings [138]. The TME in humans can be better recapitulated [137] by using patient-derived tumor cells instead of established human cancer cell lines in xenograft models [138]. For patient-derived xenograft models, biopsies of primary or metastatic solid tumors were implanted as pieces or single-cell suspensions into immunodeficient mice reproducing the human TME architecture [137]. However, the TME is still rodent and this model does still not show an inflammatory response [137]. A big challenge is also the change of tumor characteristics when they were transplanted [139]. Another approach to humanize xenograft models is the injection of patient-derived peripheral blood or bone marrow cells allowing the restoration of the immune response to the tumor [138]. Despite several disadvantages, the therapeutic efficacy of RT is most widely studied in human tumor xenograft models yet [135,138] because they enable a cheap and fast screening of anti-cancer therapies [137].

For xenograft models, several mouse strains are available [139]. The first established immunocompromised mouse was the “nude” mouse lacking the thymus and T lymphocytes which mediate the adaptive immune response [139]. As a second, severe combined immunodeficient (SCID) mice were developed [139]. Several mutations were introduced in SCID mice leading to a disordered development and maturation of functional B and T cells [139]. Crossbreeding of the SCID mouse and the non-obese diabetic (NOD) mouse established the NOD/SCID mouse model which harbors multiple defects in the innate and the adaptive immune system [139]. Both the SCID mice and

the NOD/SCID mice allow a better tumor engraftment, but they are more radiosensitive than nude mice [139]. Nude mice are well characterized and facilitate an easy detection and size measurement of subcutaneous (s.c.) tumors [139]. Therefore, s.c. implants were the primarily used side of injection for cancer research in xenograft (or syngeneic) mouse models in earlier days [130]. However, it changed to more implantation into orthotopic sites nowadays [130]. Orthotopic injection sites are more superior to s.c. tumor nodules because the tumors grow in their tissue of origin where the previous primary tumor was located in the patient [130], e.g. breast cancer cells were injected into the breast tissue. The tissue of origin possesses a specified niche which facilitates tumor growth [140]. However, the technical feasibility of surgeries is complex and time-consuming [130]. And the TME is rodent and therefore less comparable to humans [130]. Moreover, the tumor growth behavior is difficult to follow leading to survival as the main endpoint of orthotopic mouse models instead of tumor shrinkage [130].

For this doctoral thesis, the TGD assay was performed by using the human xenograft model in which the established squamous tumor cell line FaDu was subcutaneously injected. Thereto, a suspension of FaDu cells and Matrigel® providing substrates for growth promotion and tumor development [141] was injected under the skin of the right mouse ear. Irradiation took place at a maximum length of 2 mm and a maximum width of 1.8 mm. In a pilot study, tumors were irradiated with BB X-rays at the small animal radiation research platform, the SARRP. This pilot study provided the minimum integral dose of 3 Gy and the maximum integral dose of 5 Gy for the TGD assay at the MuCLS, a compact X-ray source for MRT. The proof-of-principle study at the MuCLS was conducted for assessment of the anti-tumor activity of MRT at both integral doses. Volume changes of the FaDu tumor were evaluated for 40 days by using a caliper. After the follow-up period, tumors were resected for histological analysis which is introduced in chapters 2.2 and 2.3.

## 2.2 Histological examination of tumor xenografts

The standard stain for histological studies is the hematoxylin-eosin (H&E) stain in blue and pink color. Hematoxylin is a basic dye that is positively charged after oxidation to hematein [142]. It is responsible for the blue coloring of nuclear material [142]. Eosin is a negatively charged acid dye that colors cytoplasm and extracellular matrix pink [142].

In the here presented work, the histology of FaDu tumor sections irradiated at the MuCLS was analyzed with regard to tumor size and tumor composition after H&E staining.

## 2.3 Immunohistochemical staining of $\gamma$ H2AX in tumor xenografts

Immunohistochemistry (IHC) is a widely used approach for the determination of the antigen distribution within a tissue of interest [143]. Nowadays, this approach is mainly used as a routine tool for diagnostic and pathological examination of cancer in clinical settings [143]. However, the principle of IHC exists since the 1930s [143].

IHC utilizes the specificity of immunoglobulin molecules (antibody) which are part of the adaptive immune response [144]. The adaptive immune response defends naturally the host against several foreign substances (antigens) such as pathogens by the production of antigen-targeting antibodies [144]. As soon as a pathogen infects the host, a cocktail of antibodies is produced by host B cells for defense [144]. These antibodies differ in their chemical structure and therefore belong to different classes like G, M, A, D or E [144].

For IHC the natural situation is imitated by the synthetization of antigens [144]. This resembles the naturally occurring structure [144]. Synthesized antigens were injected into host animals such as sheep, goat or rabbits that produce antibodies targeting this antigen [144]. Then, antibodies that were secreted into the bloodstream can be used for IHC staining after affinity-purification [144]. Affinity-purification isolates selectively the specialized antibodies [144]. Antigens can either be targeted by monoclonal or polyclonal antibodies which differ in the number of specificities [144]. A polyclonal antibody detects specifically more than one antigen which is in contrast to a monoclonal antibody [144].

IHC staining bases on the following principle as illustrated in Figure 3. A target antigen within the sample of interest (cells, tissue) is recognized by the primary antibody which in turn is recognized by a secondary antibody. The secondary antibody can be directly or indirectly labeled (not shown in Figure 3) with a dye for visualization.



**Figure 3. Principle of immunohistochemical staining** of an antigen (blue) on a glass slide (grey) targeted by a primary antibody (green) and a directly labeled secondary antibody (orange).

Prior to the antigen detection *via* antibodies, the samples need to be prepared. First, after sampling of the tissue, the preservation of the tissue morphology and the antigens or proteins of interest is done by fixation [144]. Fixation cross-links proteins *via* methylene bridges [144]. It is conventionally done by the use of formalin or formaldehyde [144]. Second, the tissues need to be transferred into a cuttable and storable form by either freezing or embedding into paraffin [144]. Frozen or paraffin-embedded tissues share the common feature that they facilitate the cutting of tissues into thin sections of several microns [144]. This makes them highly penetrable for antibodies and optically transparent for microscopic analyses [144]. Both techniques own different advantages and disadvantages. Frozen sections are easily made, fast to cut, preserve the antigen, but are storable for only a short period of time [144]. Paraffin-embedded sections require a time-consuming embedding step but are stable for a very long time [144].

The workflow of the IHC staining of formalin-fixed paraffin-embedded tissue sections comprises the following steps:

- (1) Rehydratization/remove of paraffin
- (2) Blocking of endogenous sources of non-specific staining
- (3) Permeabilization/antigen retrieval
- (4) Incubation with primary antibody
- (5) Wash for removal of non-specifically bound antibodies
- (6) Incubation with secondary antibody
- (7) Wash for removal of non-specifically bound antibodies
- (8) Incubation with detection reagents or counterstaining with DNA-intercalating dyes [144].

For specific visualization of the antigens, unspecific background staining needs to be reduced. Permeabilization of the sample facilitates the penetration of both primary and secondary antibody [144]. Unspecific antigen recognition by antibodies can be avoided by blocking endogenous enzymes and nonspecific targets [144]. Furthermore, washing steps remove non-specifically bound antibodies [144].

For antigen unmasking (antigen retrieval) two ways are possible. It can be done either by heat (95 °C) or by an enzymatic process that uses enzymes such as trypsin, pepsin or proteinase K [144]. If enzymes were used, physical damage of the tissue needs to be prevented which makes the tissue unusable for IHC staining [144]. Moreover, the right enzyme concentration and right treatment time need to be evaluated in advance [144]. In contrast to that, the heat-mediated antigen retrieval is much more user-friendly, less labor-intensive, and possesses a lower risk for damage [144]. However, some antigens suffer from high temperatures during antigen unmasking [144].

For visualization of the antigen, the labeling of the secondary antibody is necessary. This can be done directly or indirectly. The direct technique labels the primary antibody [144]. The indirect detection technique uses a secondary antibody with a color-generating tag [144]. For labeling, a color-generating tag can be a fluorescence dye such as Fluorescein isothiocyanate (FITC) or an enzyme that converts a colorless chemical compound into a colored label [144]. Conventionally, the naturally occurring horseradish peroxidase is used as an enzyme converting the chromogenic substrate DAB (3,3'-diamino-benzidine) into a brown color [144].

A commonly used antigen for radiation-induced DSB is the protein  $\gamma$ H2AX. H2AX is a variant within the histone H2A family which evolved highly conserved from plants to humans [145]. The Greek letter gamma ( $\gamma$ ) refers to the phosphorylation which was first discovered after  $\gamma$ -ray irradiation [145]. After radiation treatment of a cell, the H2AX molecule is phosphorylated by kinases [145]. This is one of the first events happening within minutes after exposure and reaches its maximum 30 min post-irradiation [145]. Moreover, phosphorylation of H2AX occurs close to the DSB site which is then followed by the formation of a focus composing of hundreds of  $\gamma$ H2AX molecules [145]. This focus facilitates the opening of the chromatin structure enabling the DSB repair [145]. Due to the direct correlation of the location of a DSB and  $\gamma$ H2AX response,  $\gamma$ H2AX was suggested as a universal biomarker for DSB in radiobiological studies [145].

To examine the location and the characteristics of the microbeam pattern after irradiation at the MuCLS, the DSB marker  $\gamma$ H2AX was immunohistochemically stained on FaDu tumor sections in the presented thesis. For antigen detection, the chromogenic substrate DAB was used.

## 2.4 Analysis of early side effects in irradiated skin

Radiation induces a wound within the healthy tissue due to damage to normal tissue cells [146]. Closure of the wound follows a specific sequence of events that can be subdivided into inflammation, tissue formation and tissue maturation [146].

The initial tissue damage after radiation exposure produces secondary electrons and ROS which damages cell membranes and the DNA [147]. This acute damage promotes the production of activating signals (inflammatory cytokines) by keratinocytes, fibroblasts and endothelial cells that recruit inflammatory cells *via* transendothelial migration from the circulation to the irradiated tissue [147]. The infiltration of immune cells is accompanied by blood vessel dilation which causes redness (erythema) [146]. First, granulocytes, macrophages, and lymphocytes remove the damaged tissue cells and polymorphonuclear leukocytes phagocytize debris and bacteria [146]. Second, the wound is closed after the proliferation and migration of keratinocytes [146].

The first (acute) side effect of RT is erythema but also hair follicle loss and desquamation [148]. Erythema occurs in three waves [148]. The first wave occurs within minutes to hours post-irradiation [148] due to the dilatation of capillaries [149]. Sometimes it can be accompanied by an increased vascular permeability [149]. The second wave develops after one week which can further culminate into persistent, late erythema at week 8 to 10 [148]. The main erythematous reaction is caused by inflammation secondary to the death of basal cells [150]. Desquamation is caused by a rapid proliferation of basal cells [147] which allows for the healing of the wound [146]. It is mostly dry at first [147]. It can further progress into moist desquamation after high doses of radiation [148] because the basal cell proliferation is not able to compensate for the radiation-induced cell killing in the basal layer [147]. When repopulation fails an acute ulcer can occur [146].

The severity of erythema and desquamation (acute dermatitis) can be assessed by different clinically used scoring systems. The most commonly applied scoring system is the National Cancer Institute's Common Terminology Criteria for Adverse Events (CTCAE) [151]. The severity of acute dermatitis can be graded on a linear scale from grade one to grade four [151]. Grade 1 dermatitis is characterized by mild erythema or dry desquamation [151]. With grade 2 the severity of erythema increases to 'moderate to brisk' [151]. Patients with grade 3 show confluent moist desquamation and with grade 4 the skin is necrotic or ulcerated [151]. In the last years, the scoring systems were further developed with defined increments smaller than 1 as used in CTCAE [151]. This represents sensitive changes in the severity [151]. There are the Oncology Nursing Society, the Douglas & Howler, and the Radiation Dermatitis Severity scoring systems with increments of 0.5 or 0.25 [151]. However, the clinical rating of the severity of radiation dermatitis is not routinely done according to a gold standard [151].

In this doctoral thesis, a self-designed scoring system was applied for the assessment of the severity of erythema and desquamation. In order to avoid inter-observer variations because of the missing routing experience of the examiners, a non-linear scoring system was developed for erythema. Mild erythema was graded as 0.5, definite erythema was graded as 1.5 and severe as 3. This scoring system avoids the over-evaluation of mild erythema because the difference between the grades 'no' (grade 0) and 'mild' (grade 0.5) is not always easy to discriminate. The difference between definite (grade 1.5) and severe (grade 3) erythema is more obvious. Therefore the scale is linear again. The scoring system for desquamation was linearly scaled because of a Yes-No decision. It grades the severity as dry (grade 1), crust (grade 2) and moist (grade 3). The erythema score and the desquamation score were summed up to the acute reaction score (skin score).

In this doctoral thesis, the erythema and desquamation were scored after hypofractionated X-ray RT. As a second endpoint, the ear swelling as a marker for inflammation was investigated at regular intervals by measuring the thickness of the ear with a caliper. Furthermore, ear thickness was measured after hypofractionated pMBRT.

## 2.5 Analysis of late side effects in irradiated skin

Side effects that occur month or years after treatment and persist over a long time (irreversible) are referred to as chronic [152]. Chronic side effects include the development of fibrotic tissue [153]. This process is mainly characterized by a massive production of extracellular matrix proteins such as collagen [4]. Collagen fibers can be stained by modified Masson's Trichrome (MT) [154]. The MT staining is a three-color stain composing of modified Weigert's hematoxylin (nuclei staining), acid fuchsin (cytoplasm stain) and methyl blue (collagen stain) [154]. The use of three dyes allows the differentiation between important morphological keys: Keratin and muscle fibers are colored red, cytoplasm and adipose cells in light red, cell nuclei in dark brown to black, and collagen fibers in blue [154]. Another simple and sensitive staining method of collagen fibers uses Picrosirius red [155]. This is a strong, anionic dye with sulfonate groups that is able to react with cationic collagen fibers [155]. This reaction creates different colors under polarized light which is useful for the quantification of collagen fibers according to the orientation of the collagen bundles [155]. Therefore, Picrosirius red staining corresponds to the thickness and packing of collagen fibers [155]. The Picrosirius red stain is used as a routine staining method because it stains thin collagen fibers intensely and it does not fade [156] which contrasts the MT staining [157].

The development of fibrosis is mediated by an inflammatory process that starts immediately after RT and turns into a chronic process [152]. The deposition of collagen fibers is driven by the expression of TGF $\beta$ 1 [4]. TGF $\beta$ 1 activates fibroblasts and enhances the production of extracellular matrix proteins [152]. In patients, fibrosis is also characterized by the formation of edema (lymphedema) [152]. Edema is caused by a dysfunction of the cutaneous lymphatic system [158]. This abnormal buildup of fluid in the body is also associated with inflammation [159]. Next to fibrosis, the loss of hair follicles and glands is chronically [152].

In this doctoral thesis, the amount of fibrotic tissue was quantified in ear sections after Sirius Red staining. This was done either after around 90 days upon X-ray hypofractionation or after around 150 days post-hypofractionated pMBRT.

Furthermore, chronic inflammation was assessed according to a scoring system comprising three grades. Grade 0 describes no relevant infiltration of neutrophils, no vasodilation or edema. Grade 1 is characterized by extravascular neutrophils and mononuclear cells. Grade 2 shows a multifocal to diffuse appearance of neutrophils and mononuclear cells. 92 days after X-ray hypofractionation ear sections were blindly and independently assigned to the inflammation grades 0 to 2. Furthermore, 92 days after X-ray hypofractionation the number of TGF $\beta$ 1-expressing cells was quantified in sections of murine ears. Sections were immunohistochemically stained by using antibodies targeting the antigen TGF $\beta$ 1. The principle of immunohistochemistry is explained in chapter 2.3. Moreover, the lack of hair follicles was quantified.

## 3 Results

### 3.1 A proof-of-principle experiment for MRT at the Munich Compact Light Source

#### 3.1.1 Aim and summary of the study

In recent years, several compact X-ray sources were developed and it was investigated if they are suitable for the performance of MRT. It was suggested that compact X-ray sources are able to replace large synchrotron radiation facilities in the future in order to bring MRT closer to radiobiological researchers and prospective clinical trials. However, technical challenges such as dose rate and X-ray energy limit the widespread use of compact X-ray sources up to now (more details in chapter 1.3.3.1). So far, only the CNT X-ray source and the MuCLS are installed and accessible for preclinical MRT studies. Previous work at the CNT X-ray source demonstrated that MRT inhibits tumor growth at lower dose rates of 1.2 Gy/min and thus lower peak doses [113,114]. In this doctoral thesis, the aim was to prove the ability of the MuCLS producing monochromatic and spatially fractionated X-rays to slow down tumor growth in a mouse ear model.

In a pilot study at the conventional X-ray tube SARRP, a dose-response curve of FaDu tumors inoculated into mouse ears was established. It shows that tumor growth is controlled at 6 Gy, while the growth slows down from 3 Gy on. Therefore, a dose range between 3 Gy and 5 Gy was determined for the proof-of-principle study at the MuCLS. The results of the proof-of-principle study showed tumor growth retardation after MRT and broadbeam radiation. The staining of the DSB marker  $\gamma$ H2AX confirms the microbeam pattern of 50  $\mu$ m width and proves the successfully targeted irradiation of FaDu tumors in mouse ears. The tumor inoculation rate of FaDu tumor cells is about 87 % in the pilot study, while 77 % of animals develop a tumor in the MuCLS study, which was well in line with the literature [160].

In conclusion, this proof-of-principle study at the new compact X-ray source, the MuCLS, demonstrated for the first time an anti-tumor efficiency in a preclinical setting using MRT at low dose rates and low X-ray energies. The highly innovative MuCLS overcomes some drawbacks of commonly used synchrotron radiation facilities regarding space requirements and costs. In addition, MRT studies at the MuCLS pave the way for a more widespread and detailed preclinical research on the mechanisms of MRT and will enable the irradiation of cancer patients in a clinical setting in the future.



### 3.1.2 Contributions

I established the method of tumor cell inoculation in our animal facility. For all parts of this study, I prepared the tumor cells for tumor cell inoculation, and Marlon Stein and Prof. Dr. Thomas Schmid supported me in tumor cell injection. I planned the execution of the pilot experiment at the SARRP, the TGD study at the MuCLS and the histological study in collaboration with Dr. Karin Burger (physical part).

I conducted the pilot experiment at the SARRP including whole-body irradiations prior to tumor cell injection, tumor size measurements, irradiation, and aftercare. Prof. Dr. Jan J. Wilkens and Dr. Karin Burger helped to irradiate tumors in the proper size at the SARRP. For the study at the MuCLS, I transported the animals between the animal facility and the location of the MuCLS in Garching. I anesthetized the mice for tumor irradiation. Prof. Dr. Thomas Schmid, Marlon Stein, and Ann-Kristin Porth helped me to fix the mice ears for tumor irradiation. Irradiation at the MuCLS was performed by Dr. Karin Burger, Benedikt Günther, and Dr. Martin Dierolf. The aftercare and tumor size measurements were done by me with the support of Marlon Stein and Ann-Kristin Porth. For the histology study, tumor size measurements were performed by Ann-Kristin Porth and me. Irradiation at the MuCLS was conducted by Karin Burger and me with the support of Benedikt Günther and Dr. Martin Dierolf. I did the tumor excision and fixation. Cutting tumor slices and staining of  $\gamma$ H2AX was performed by the Research Unit Analytical Pathology at the Helmholtz Center Munich (Dr. Annette Feuchtinger).

For all parts of this study, I performed data analysis and interpretation. Moreover, I designed all figures, illustrations, and tables and I wrote the manuscript. All co-authors, especially Dr. Karin Burger, Prof. Dr. Thomas Schmid, and Prof. Dr. Jan J. Wilkens contributed to the scientific discussion and data interpretation.

### 3.1.3 Publication

The data were presented in the following original peer-reviewed research article on October 26<sup>th</sup> in 2019 in the Journal 'Radiation and Environmental Biophysics'.

#### ***A proof of principle experiment for microbeam radiation therapy at the Munich compact light source***

Annique C. Dombrowsky, Karin Burger, Ann-Kristin Porth, Marlon Stein, Martin Dierolf, Benedikt Günther, Klaus Achterhold, Bernhard Gleich, Annette Feuchtinger, Stefan Bartzsch, Elke Beyreuther, Stephanie E. Combs, Franz Pfeiffer, Jan J. Wilkens, Thomas E. Schmid

Radiat Environ Biophys. 2019

DOI:10.1007/s00411-019-00816-y



# A proof of principle experiment for microbeam radiation therapy at the Munich compact light source

Annique C. Dombrowsky<sup>1,2</sup> · Karin Burger<sup>2,3,4</sup> · Ann-Kristin Porth<sup>2</sup> · Marlon Stein<sup>1,2</sup> · Martin Dierolf<sup>3,4</sup> · Benedikt Günther<sup>4</sup> · Klaus Achterhold<sup>3,4</sup> · Bernhard Gleich<sup>4</sup> · Annette Feuchtinger<sup>5</sup> · Stefan Bartzsch<sup>1,2</sup> · Elke Beyreuther<sup>6,7</sup> · Stephanie E. Combs<sup>1,2,8</sup> · Franz Pfeiffer<sup>3,4,9</sup> · Jan J. Wilkens<sup>2,3</sup> · Thomas E. Schmid<sup>1,2</sup>

Received: 27 February 2019 / Accepted: 14 October 2019  
© Springer-Verlag GmbH Germany, part of Springer Nature 2019

## Abstract

Microbeam radiation therapy (MRT), a preclinical form of spatially fractionated radiotherapy, uses an array of microbeams of hard synchrotron X-ray radiation. Recently, compact synchrotron X-ray sources got more attention as they provide essential prerequisites for the translation of MRT into clinics while overcoming the limited access to synchrotron facilities. At the Munich compact light source (MuCLS), one of these novel compact X-ray facilities, a proof of principle experiment was conducted applying MRT to a xenograft tumor mouse model. First, subcutaneous tumors derived from the established squamous carcinoma cell line FaDu were irradiated at a conventional X-ray tube using broadbeam geometry to determine a suitable dose range for the tumor growth delay. For irradiations at the MuCLS, FaDu tumors were irradiated with broadbeam and microbeam irradiation at integral doses of either 3 Gy or 5 Gy and tumor growth delay was measured. Microbeams had a width of 50  $\mu\text{m}$  and a center-to-center distance of 350  $\mu\text{m}$  with peak doses of either 21 Gy or 35 Gy. A dose rate of up to 5 Gy/min was delivered to the tumor. Both doses and modalities delayed the tumor growth compared to a sham-irradiated tumor. The irradiated area and microbeam pattern were verified by staining of the DNA double-strand break marker  $\gamma\text{H2AX}$ . This study demonstrates for the first time that MRT can be successfully performed in vivo at compact inverse Compton sources.

**Keywords** MRT · Microbeam · Inverse Compton X-ray sources · Tumor · X-rays · Growth delay

## Introduction

Microbeam radiation therapy (MRT) is a preclinical, spatially fractionated form of radiation therapy (Slatkin et al. 1992, 1995; Laissue et al. 1998). MRT deposits very high doses, also referred to as peak dose, in parallel and

planar beams with a width of 25–75  $\mu\text{m}$  and a spacing of 100–400  $\mu\text{m}$ . Also beams with a width of 680  $\mu\text{m}$  (Dilmannian et al. 2006) or 950  $\mu\text{m}$  (Anschel et al. 2007) were able to spare normal tissue and control tumors. The deposited dose between two microbeams is lower than the tolerance dose of the normal tissue. This so-called valley dose is influenced by

✉ Thomas E. Schmid  
thomas.schmid@helmholtz-muenchen.de

<sup>1</sup> Institute of Radiation Medicine, Helmholtz Zentrum München GmbH, 85764 Neuherberg, Germany

<sup>2</sup> Department of Radiation Oncology, School of Medicine, Klinikum rechts der Isar, Technical University of Munich, 81675 Munich, Germany

<sup>3</sup> Chair of Biomedical Physics, Department of Physics, Technical University of Munich, 85748 Garching, Germany

<sup>4</sup> Munich School of BioEngineering, Technical University of Munich, 85748 Garching, Germany

<sup>5</sup> Research Unit Analytical Pathology, Helmholtz Zentrum München GmbH, 85764 Neuherberg, Germany

<sup>6</sup> Helmholtz-Zentrum Dresden-Rossendorf, 01328 Dresden, Germany

<sup>7</sup> OncoRay, National Center for Radiation Research in Oncology, Faculty of Medicine, University Hospital Carl Gustav Carus, Technische Universität Dresden, Helmholtz-Zentrum Dresden-Rossendorf, 01328 Dresden, Germany

<sup>8</sup> German Consortium for Translational Cancer Research, Deutsches Konsortium für Translationale Krebsforschung (dtk), Technical University Munich, 81675 Munich, Germany

<sup>9</sup> Department of Diagnostic and Interventional Radiobiology, School of Medicine, Klinikum rechts der Isar, Technical University of Munich, 81675 Munich, Germany

scattering of secondary electrons and photons from adjacent peaks (Sabatasso et al. 2011).

First in vitro and in vivo experiments focusing on tumoricidal effects of spatially fractionated irradiations were performed at large synchrotron radiation facilities such as the European Synchrotron Radiation Facility in France (Regnard et al. 2008; Bouchet et al. 2010, 2016; Gil et al. 2011; Fardone et al. 2018). Owing to their ultra-high dose rates of hundreds of Gray per second and a small beam divergence, synchrotrons are particularly suited to maintain the microbeam pattern within the tissue without blurring (Bartzsch and Oelfke 2017). Synchrotron-generated X-ray MRT induces a differential radiobiological response in tumor and normal tissues. While the normal tissue is exceptionally tolerant to the high doses in the peak regions, the tumor growth is delayed and even sometimes controlled after MRT (Laissue et al. 1998; Serduc et al. 2009; Bouchet et al. 2010; Crosbie et al. 2010). The mechanisms playing a role in the differential response of tumor and normal tissue are still unknown but there is some evidence of a differential repair of the vasculature as well as bystander effects which are, at least in part, responsible for the sparing effect (Dilmanian et al. 2007).

Patients with tumors in brain or lung surrounded by radiosensitive normal tissues would especially benefit from the pronounced tissue sparing effect of MRT (Ibahim et al. 2014; Archer et al. 2017). However, the use of synchrotrons for cancer treatment with MRT in clinics is hampered by the large space requirements and their cost-intensive operation (Bartzsch and Oelfke 2017). Therefore, in recent years new compact X-ray sources were developed such as the carbon nanotube X-ray source (Hadsell et al. 2013) or the compact light source (CLS) (Eggl et al. 2016). CLSs are based on the concept of inverse Compton scattering. Inverse Compton scattering is a collision between electrons and laser photons producing nearly monochromatic X-rays. The CLS, located in Garching (Germany) and manufactured by Lyncean Technologies Inc., USA, is a compact synchrotron source producing X-rays with photon energies of 15–35 keV (Eggl et al. 2016; Burger et al. 2017). The unique features of the CLS are a small circumference of the electron storage ring of 4.6 m and a short period of the laser undulator defined by the half of the laser wavelength of 0.5  $\mu\text{m}$ , allowing a size of the source of about  $2 \times 7 \text{ m}^2$  (Eggl et al. 2016). In recent years CLS was used for pre-clinical imaging and diagnostic of pulmonary emphysema (Schleede et al. 2012b) or breast cancer (Schleede et al. 2012a) but the CLS can also be adopted for MRT due to its synchrotron-like features.

The tumoricidal effectiveness and the sparing effect of MRT at compact X-ray sources seems to be comparable to previous observations made at synchrotrons. Treatment of brain tumors with MRT generated at the carbon nanotube-based X-ray source extended the lifespan of tumor-bearing

animals compared to an untreated control group (Yuan et al. 2015). In contrast to MRT at synchrotrons using peak doses of more than 100 Gy (Fardone et al. 2018), even lower peak doses of 48 Gy or 72 Gy delayed tumor growth at compact X-ray sources (Yuan et al. 2015). At the beamline of the Munich compact light source (MuCLS), in vitro experiments showed an increased survival of normal tissue cells with a lower frequency of chromosomal aberrations following MRT compared to broadbeam irradiation (Burger et al. 2017).

Both compact X-ray sources (Jacquet and Suortti 2015) and synchrotrons (Prezado et al. 2009) produce X-rays with a mean energy in the keV range. Additionally, compact X-ray sources have the advantage of lower operational costs and a laboratory-sized scale. All these features render compact X-ray sources as suitable candidates for a future implementation of MRT into the clinics. To embed MRT in treatment plans of cancer patients, fundamental research of biological mechanisms and dose concepts of MRT is necessary. Especially, studies using animal models at easily accessible compact sources might help to understand MRT in more detail. Here, we show the first in vivo MRT experiment at the MuCLS, a compact synchrotron X-ray source, and evaluate its tumoricidal effect in a mouse model bearing a xenograft of squamous carcinoma cells. This proof of concept study introduces a compact X-ray source at which MRT can be performed now and which can be used for MRT in vivo studies in the future.

## Materials and methods

### Mouse ear tumor model

All experiments were performed using female, immunocompromised, 8–10 weeks old NMRI nu/nu mice obtained from Charles River Laboratories (Sulzfeld, Germany). Mice were hosted at the experimental sites of the Klinikum rechts der Isar in Munich according to the respective institutional guidelines and the German animal welfare regulations. The animals were kept at 20–24 °C, 45–60% relative humidity, at 12 h light–dark cycle and fed with commercial laboratory animal diet and water ad libitum. All experiments were approved by the regional animal ethics committee (project license 55.2-1-54-2531-62-2016).

Studies were carried out for the undifferentiated human head and neck cancer cell line FaDu maintained at 37 °C, 5% CO<sub>2</sub> in Dulbecco Modified Eagle's Medium with 1000 mg/ml glucose (Sigma-Aldrich Chemie GmbH, Munich, Germany). The media was supplemented with 10% FBS (Roche AG, Grenzach-Wyhlen, Germany), 2 mM L-glutamine, 1 mM sodium pyruvate, 1% Penicillin/Streptomycin (all Sigma-Aldrich Chemie GmbH, Munich, Germany) and

10 mM HEPES (Thermo Fisher Scientific, Germering, Germany).

The mouse ear tumor model was originally established by the group of Suit et al. in 1965 and recently published as suitable model for low energy irradiation by Beyreuther et al. (2017). In order to suppress the immune response, 2–4 days before tumor cell injection nude mice were whole-body irradiated in a specifically designed cage which allows only a two dimensional movement of the mouse. Whole-body irradiation took place with 4 Gy of 200 kVp 15 mA X-rays filtered by aluminum (Xstrahl Limited, Camberley, UK). Then, 1 µl/g body weight of the antibiotic Convenia (Zoetis Schweiz GmbH, Zürich, Switzerland) was subcutaneously injected into the neck. For tumor cell injection, about 100,000 FaDu tumor cells were resuspended with 50 µl Matrigel (Matrigel Basement Membrane Matrix, Corning, New York, USA). Mice were anesthetized intraperitoneally with a mixture of 1 mg/ml medetomidin, 5 mg/ml midazolam and 0.05 mg/ml fentanyl (in-house production, Klinikum rechts der Isar, Munich, Germany). About 5 µl of the ice-cooled tumor cell suspension were injected subcutaneously between the cartilage and skin at the center of the right ear. The anesthesia was antagonized by subcutaneous injection of AFN (composed of 0.5 mg/ml atipamezole, 5 mg/ml flumazenil and 3 mg/ml falozone, in-house production, Klinikum rechts der Isar, Munich, Germany). Tumor growth was measured every second day using a digital caliper of 0.01 mm accuracy (DigiMax 29422, Wiha, Buchs, Switzerland). The location of the tumor at the ear allows size measurement in three dimensions. Tumor volume was determined according to the formula  $V = \frac{\pi}{6} \times a \times b \times c$ . The length  $a$  of the tumor was defined as the size of the tumor parallel to the main blood vessels. The width  $b$  is perpendicular to the tumor length in the plane of the mouse ear. Measuring the maximum extension out of this plane, the height  $c$  was derived. Tumors with a maximum length of 2 mm and a maximum width of 1.8 mm were included into the experiment. There were no limitations regarding tumor height. A second criterion for tumor irradiation was the color of the tumor which changed from white to red once the tumor was vascularized. Only red-colored tumors were included into the experiment.

### Irradiations at a conventional X-ray tube

A pilot study was carried out to estimate X-ray doses which induce a growth delay of xenograft FaDu tumors in the ear. This study was performed at the Small Animal Radiation Research Platform (SARRP, Xstrahl Limited, Camberley, UK) using doses of 3 Gy and 6 Gy (Oppelt et al. 2015) applying 70 kVp X-rays filtered by aluminum. Tumor cells were inoculated in 8 mice from which all animals developed a tumor except one mouse. Therefore, two FaDu

tumor-bearing mice were irradiated per dose group and three FaDu tumor-bearing mice served as a control without irradiation. Irradiation took place with a dose rate of 2.4 Gy/min. For irradiations, a round-shaped field size of 4 mm in diameter was used. The distance between target and X-ray source was 350 mm. The tumor was centered in the irradiation field and homogeneously irradiated perpendicular to the plane of the mouse ear. Dose delivery was verified using a radiochromic film (Gafchromic EBT-3, Ashland, USA). Dose values refer to mean doses over the central area of the field as measured with radiochromic film (calibrated with an ionization chamber in an open field) before the actual experiment was performed.

On the day of irradiation, the tumor had to fulfill the pre-defined criteria for size and color. Tumor growth was determined during a follow-up period of about 30 days. Volume measurements were stopped earlier if one tumor dimension reached 8 mm (abort criteria). Growth delay of irradiated tumors was compared to unirradiated control tumors.

### Tumor irradiation at MuCLS and follow-up

The radiobiological effect was compared between micro-beam and broadbeam irradiation by determining the radiation-induced tumor growth delay at the MuCLS (CLS from Lyncean Technologies Inc., Fremont, USA) situated at the Munich School of BioEngineering in Garching (Germany). Tumor growth delay was compared between treated animals and one sham-irradiated animal. Tumor cells were inoculated in seven mice in total from which two animals were used as a reserve because the pre-experiment at the SARPP showed a tumor inoculation rate below 100%. For each dose group and modality, one tumor-bearing mouse was irradiated with either sham, microbeams or broadbeams at 3 Gy or 5 Gy at the MuCLS, respectively.

The CLS was operated with a mean energy of 25 keV X-rays having a bandwidth of 3.6%. The distance between the X-ray source and a dedicated irradiation system to treat the mouse ear was 4 m. Besides dose monitoring, the irradiation system comprises means for mouse positioning and maintaining the body temperature. The dose rate and the delivered dose at the plane of the ear was calculated from the measured photon flux. For this purpose, we used an in-house built, highly transmissible intensity counter (online monitor) which was placed into the beam in front of the irradiation target. The intensity counter was calibrated using a photon-counting detector (Pilatus 200 K, Dectris Ltd., Baden, Switzerland). The dose distribution of microbeam pattern (see below) including the peak-to-valley dose ratio (PVDR) was determined using radiochromic film (Gafchromic EBT-3, Ashland, UK) and accompanying Monte Carlo simulations (GEANT4). More details of the technical implementation, characterization, commissioning and dosimetry are reported

in a separate paper (Burger et al. in preparation), basic information about the MuCLS are reported in Eggl et al. (2016).

On the day of irradiation, the tumor had to fulfill the predefined criteria for size and color. Animals were anesthetized as described for tumor cell injection (see section mouse ear tumor model). All treated mice were anesthetized for a maximum time of 1 h. This time includes time for positioning of the mouse into the holder, time for positioning of the tumor within the X-ray beam, and time for irradiation. The sham-irradiated mouse was anesthetized for about 30 min and fixed in the mouse holder for 16 min. This time is in the range of the mean time of fixation of irradiated animals. The 3 Gy MRT irradiated mouse was anesthetized for 41 min with a fixation time of 25 min and 5 min for irradiation. The 5 Gy MRT irradiated mouse was anesthetized for 50 min, fixed for 29 min and irradiated for 10 min. The 3 Gy broadbeam irradiated mouse was anesthetized for 32 min, fixed in the mouse holder for 11 min and irradiated for 43 s. The 5 Gy broadbeam irradiated mouse was anesthetized for 27 min, fixed for 10 min and irradiated for 80 s.

The ear of the anesthetized mouse was fixed onto the mouse holder with removable tape (Fig. 1a). Additional heating to 32–33 °C allowed the maintenance of the body temperature of the anesthetized mouse. Tumors were positioned in the middle of the irradiation field and irradiated perpendicular to the plane of the mouse ear. A positioning system allowed for accurate placement of the tumor in the X-ray beam with a circular irradiation field of 2.3 mm in diameter. Tumor-bearing mice were randomly assigned to the following irradiation groups: sham, microbeam or broadbeam irradiation. Tumors were irradiated with an integral dose of either 3 Gy or 5 Gy. These doses for broadbeam irradiations were chosen with the aim to compare the same integrated doses for broadbeam and microbeam irradiations. Therefore, tumors were irradiated with microbeams using peak doses of either 21 Gy or 35 Gy and valley doses below 0.2 Gy, respectively. Microbeams with a width of 50  $\mu\text{m}$  and

a center-to-center distance of 350  $\mu\text{m}$  were generated using a highly absorbing tungsten collimator with a ratio of 1/7 slit to 6/7 tungsten. The irradiation pattern and dose to each irradiated tumor was verified individually by a radiochromic film (Gafchromic EBT-3, Ashland, USA) (Fig. 1b). For this, the radiochromic film was positioned behind the tumor of each mouse. Sham irradiation follows the same protocol with exception that the X-ray beam remained switched off.

Irradiations took place with a dose rate up to 5 Gy/min for broadbeam and 0.6 Gy/min for microbeams. The dose rate was measured as integrated dose rate. Since 6/7 of the broadbeam radiation field were blocked by the tungsten collimator, the integrated dose rate is a factor of 7 lower than in the broadbeam field. On top, scattering led to a slight reduction of the dose rate. The peak dose rate was in the order of 4.2 Gy/min. Hence peak dose rate and broadbeam dose rate are comparable. On average, microbeam irradiation applying an integral dose of either 3 Gy or 5 Gy took about  $5.6 \pm 0.8$  min or  $9.5 \pm 1.3$  min, respectively. For broadbeam irradiation,  $0.9 \pm 0.3$  min and  $1.2 \pm 0.4$  min were necessary for 3 Gy or 5 Gy, respectively.

After irradiation the animals were retained in quarantine during the follow-up period. Tumor growth was measured as described before (see section mouse ear tumor model). Mice were euthanized as soon as one tumor dimension reached 8 mm (Fig. 1c).

### Staining of $\gamma\text{H2AX}$ on histological tumor sections

To prove the irradiated area and microbeam pattern, tumor cells were inoculated in two additional animals which were irradiated at the MuCLS and assigned to histological analysis. Tumor sections were stained with hematoxylin and eosin (H&E). Staining of the DNA double-strand break marker  $\gamma\text{H2AX}$  was performed to verify irradiation side and pattern retrospectively. The treated animal was sacrificed 1 h after microbeam irradiation when the maximum expression

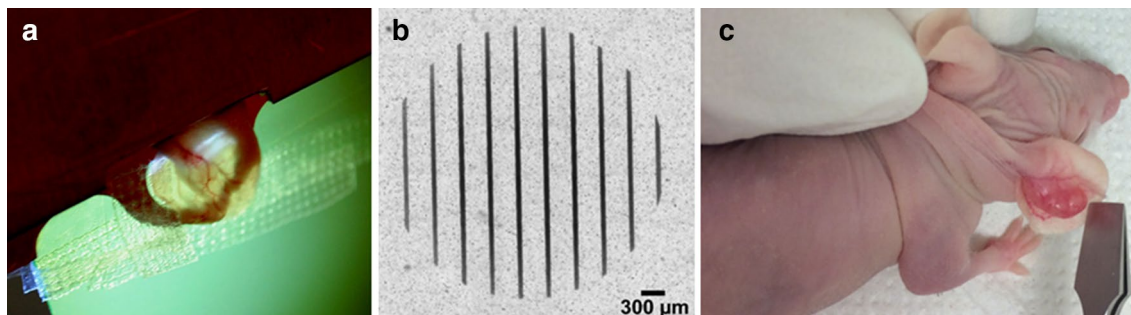


**Fig. 1** **a** Tumor-bearing mouse ear is fixed with tapes onto the holder. The FaDu tumor has a size of 2 mm in diameter and is red-colored on day of irradiation. **b** Radiochromic film placed behind the ear was irradiated using microbeams with an integral dose of 5 Gy. Micro-

beam pattern with a beam width of 50  $\mu\text{m}$  and a spacing of 300  $\mu\text{m}$  is visible. **c** Illustration of the tumor size at the end of the follow-up period of tumor growth delay experiment



of  $\gamma$ H2AX is assumed (Kinner et al. 2008). The tumor was resected and fixed in 4% (w/v) neutrally buffered formalin, embedded in paraffin and cut into 3  $\mu$ m slices for H&E staining or for immunohistochemistry. Immunohistochemical staining was performed under standardized conditions on a Discovery XT automated stainer (Ventana Medical Systems, Tucson, Arizona) using rabbit anti- $\gamma$ H2AX (1:500, NB100384, NOVUS Biologicals, Wiesbaden, Germany) as a primary antibody and Discovery Universal (Ventana Medical Systems, Tucson, Arizona) as secondary antibody. Signal detection was conducted using the Discovery<sup>®</sup> DAB Map Kit (Ventana Medical Systems, Tucson, Arizona). The stained tissue sections were scanned with an AxioScan.Z1 digital slide scanner (Zeiss, Jena, Germany) equipped with a 20 $\times$  magnifying objective.

## Results

### Pilot study for tumor growth delay after broadband irradiation at SARRP

Tumor cells were subcutaneously injected into the ear of NMRI nude mice. Tumors developed and grew to a size of 2 mm in diameter at which homogeneous irradiation took place. Changes in tumor volume were measured after both 3 Gy and 6 Gy at the SARRP. Figure 2 shows the FaDu tumor growth delay over a period of 25 days. In total, two tumors were irradiated with either 3 Gy or 6 Gy of broadband. Three mice served as controls. Control tumors had a volume doubling time of  $2.76 \pm 0.4$  days. At 3 Gy tumor growth was delayed in one of two mice. Following 6 Gy

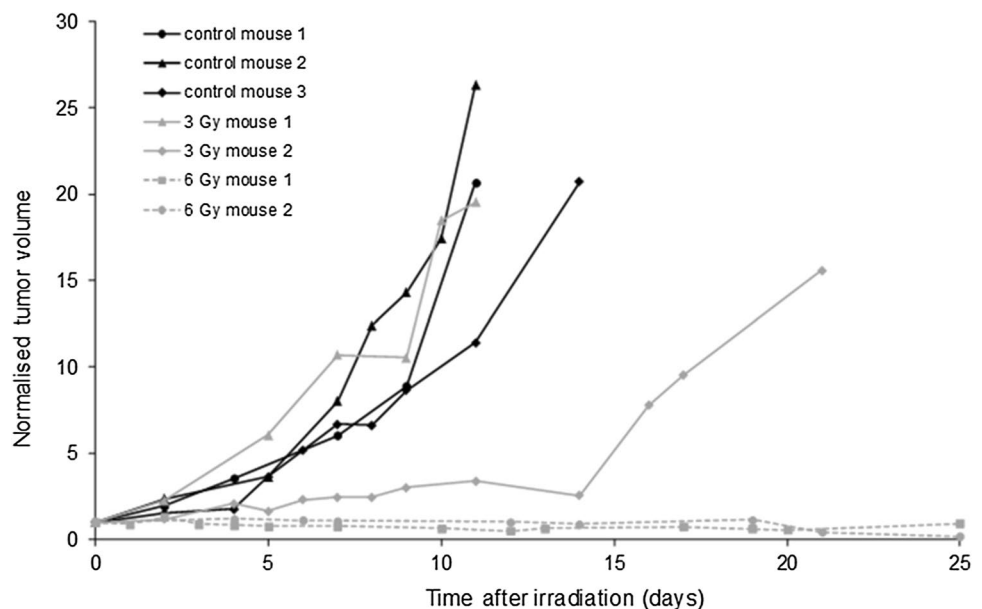
broadbeam irradiation, both FaDu tumors were controlled in their growth.

From this pre-study, we concluded that a dose between 3 Gy and 5 Gy might cause a measurable tumor growth delay at the MuCLS. X-rays of 25 keV at the MuCLS are radiobiological more effective and should therefore be able to induce a clear growth delay at 3 Gy. Furthermore, an integral dose of 5 Gy was chosen in order to have a difference of X-ray doses big enough to resolve a difference between both used doses. A dose higher than 5 Gy was not possible to choose due to the narrow dose range for tumor growth delay as shown in the pre-study. In addition, due to the higher radiobiological effectiveness of 25 keV X-rays a dose higher than 5 Gy could be able to induce a tumor control at the MuCLS which should be avoided. With the aid of the growth delay curves after broadband irradiation, the 15-fold of initial volume was used for calculation of the growth delay of irradiated tumors in comparison to the sham-irradiated tumor at the MuCLS.

### Tumor inoculation rate of FaDu tumor cells into mouse ears

FaDu tumor cells were inoculated in eight mice for the pre-experiment at the SARRP. Out of eight, only seven developed a tumor. The tumor inoculation rate is about 87%. For tumor growth delay at the MuCLS, tumor cells were inoculated in seven animals and in two additional animals for histological analysis. Out of nine mice, tumors in seven animals become visible and grew to the particular size on day of irradiation. Four tumor-bearing animals were irradiated with either broadband or microbeam, and one tumor-bearing animal was used as a sham-irradiated

**Fig. 2** Growth delay of individual FaDu tumors without irradiation (black lines) and after broadband irradiation with either 3 Gy (grey lines) or 6 Gy (grey dashed lines) using 70 kVp X-rays at the SARRP



control for studying tumor growth delay at the MuCLS. Two tumor-bearing animals were irradiated for histological analysis. In summary, tumors inoculation was successful in around 77% of all animals for irradiation at the MuCLS.

### Effect of microbeam irradiation at the MuCLS on tumor growth

Five tumors were irradiated with either sham, microbeams or broadbeam using an integral dose of either 3 Gy or 5 Gy, respectively. After irradiation, tumor growth was recorded until the tumors reached at least their 15-fold initial volume, as determined in the previous pilot study.

Figure 3 shows the tumor volume normalized to the volume on the day of irradiation over time for one mouse per treatment group. The tumor growth curves were linearly interpolated. This preliminary data indicates that growth of all irradiated tumors was delayed compared to the sham-irradiated tumor. The time reaching the 15-fold initial volume increased with increasing integrated dose from 3 Gy to 5 Gy, independently from the radiation modality. On day 21 after irradiation, the sham-irradiated tumor reached the 15-fold volume. After 3 Gy MRT and 5 Gy MRT, tumor growth was delayed and the 15-fold initial volume was reached 3.5 days and 13.5 days later, respectively, compared to the sham-irradiated tumor. For broadbeam irradiations, the 15-fold initial volume was estimated at day 30 and day 37.5 after 3 Gy and 5 Gy, respectively. This corresponds to a tumor growth delay of 9 days for 3 Gy broadbeam irradiated tumors and for 16.5 days for 5 Gy broadbeam irradiated tumors compared to sham-irradiated tumors. To conclude, these preliminary

data show that MRT can induce a tumor growth delay and MRT studies can be performed at the MuCLS now.

### $\gamma$ H2AX staining of a tumor after microbeam irradiation at MuCLS

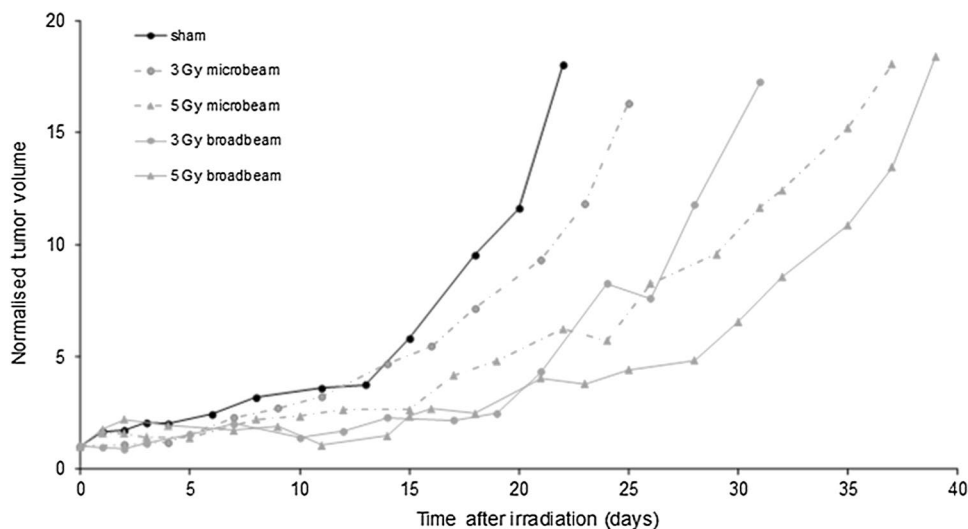
Figure 4a illustrates the FaDu xenograft tumor of one out of two animals on day of irradiation. Tumor cells were grown in nodules surrounded by matrigel, clearly separated from the surrounding tissue and above the cartilage. Figure 4b, c show exemplarily the microbeam pattern, observed 1 h after microbeam irradiation of 5 Gy. The whole area of the injection side of tumor cells mixed with matrigel was irradiated with a total of eight microbeams. The lines with  $\gamma$ H2AX stained cells clearly correlate with the used microbeam width of 50  $\mu$ m. In addition, the center-to-center distance of microbeams on the immunologically stained ear sections matches with the pattern given by the tungsten collimator (beam width of 350  $\mu$ m).

### Discussion

This in vivo study demonstrates that microbeam irradiation can be performed at the MuCLS using a compact synchrotron X-ray source. Microbeam and broadbeam irradiations at the MuCLS were able to induce a tumor growth delay in one mouse, respectively, compared to one sham-irradiated tumor using X-rays with a mean energy of 25 keV. The irradiation pattern of microbeams was confirmed by staining of  $\gamma$ H2AX.

The comparison of the tumoricidal effect between microbeam and broadbeam irradiation at the MuCLS can be done only with caution. In our proof of concept study, we used only one tumor-bearing mouse per treatment group which is

**Fig. 3** Normalized tumor volumes over the follow-up period after sham irradiation (black line), microbeam irradiation (grey dashed lines) and broadbeam irradiation (grey lines) using 25 keV X-rays at the MuCLS. One mouse per treatment was monitored until the tumor reached the 15-fold initial volume



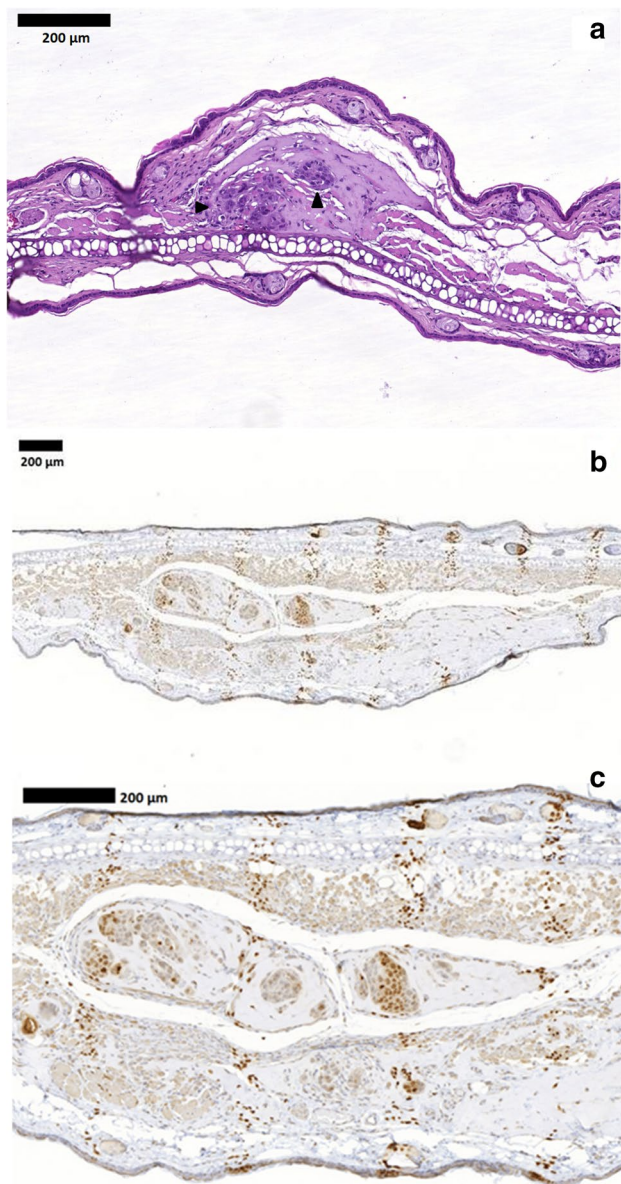


**Fig. 4** Histological analysis of FaDu tumors in mouse ears after 5 Gy microbeam irradiation at the MuCLS. Ear sections were stained with **a** hematoxylin and eosin ( $\times 10$  magnification) or **b**, **c**  $\gamma$ H2AX 1 h post-irradiation. Image **b** has a  $\times 5$  magnification. In **a** the tumor is marked by arrow heads. In **c** the same tumor as depicted in **b** is shown with a higher magnification of  $\times 10$  to illustrate the microbeam width of 50  $\mu$ m and a separation of 300  $\mu$ m. Only the part of the ear harboring the tumor is shown

not statistically representative and therefore does not allow a solid conclusion on the tumoricidal effect of MRT at the MuCLS. Nevertheless, our preliminary results give a hint that the delay of tumor growth is increased after broadbeam irradiations compared to microbeam irradiations if integral doses of 3 Gy and 5 Gy were compared. This observation is contradicted to the well-studied advantageous effect of MRT

(Dilmanian et al. 2002; Regnard et al. 2008). From a technical point of view, a possible explanation for the reduced inhibitory effect of microbeam irradiations on tumor growth could be the delivered peak and valley dose at the MuCLS. Most of the *in vivo* studies used much higher doses in the valley and peak region of around 20 Gy and several hundred Gy, respectively (Dilmanian et al. 2002; Serduc et al. 2009). At the MuCLS, FaDu tumors were irradiated with very low peak doses of either 21 Gy or 35 Gy and a quite constant valley dose below 0.2 Gy. A second important, technical parameter for tumor growth inhibition is the PVDR. The PVDR should be low in the tumor to inhibit any repair mechanisms (Prezado et al. 2009) and thus decrease the rate of tumor growth. In the MRT study of Serduc et al. (2009) PVDRs were used between 18 and 48. This is in contrast to our study at the MuCLS applying much higher PVDRs meaning a lower valley dose which might contribute to an increased DNA damage repair and therefore contribute to an increased tumor growth after microbeam irradiation. A third technical parameter influencing tumor growth inhibition could be the dose rate which was much lower (0.6 Gy/min) at the MuCLS compared to MRT studies at synchrotrons using more than 100 Gy/s (Chtcheprov et al. 2014). However, it has been shown that ultra-high dose rates ( $\geq 40$  Gy/s, FLASH) can be as efficient as conventional dose rates ( $\leq 0.03$  Gy/s) in suppression of tumor growth (Favaudon et al. 2014). Animal studies using ultra-high dose rates for MRT at synchrotrons showed a pronounced tumor growth inhibition. However, according to Favaudon et al. (2014) the low dose rate used at the MuCLS should not be the reason for the observed weak tumor growth delay after microbeam irradiation since the dose rate of 0.6 Gy/min for microbeam irradiation corresponds to 0.01 Gy/s, which is in the range of the conventional dose rates as suggested by Favaudon et al. (2014). From a biological point of view, the reduced inhibitory effect of MRT on tumor growth is in agreement with another MRT study at a compact X-ray source. It has been shown that low peak doses of 48 Gy in combination with low valley doses below 5 Gy only slightly decrease tumor growth after microbeam irradiation compared to broadbeam irradiation (Zhang et al. 2014; Yuan et al. 2015). This less pronounced tumor growth inhibition after microbeam irradiations shown in both studies at compact X-rays sources might be attributed to the absence of a direct cytotoxic effect due to a too low valley dose below 0.2 Gy at the MuCLS inducing subsequently no or only a reduced necrosis in the entire tumor. A similar conclusion was drawn in a 9L brain tumor model using even a much higher valley dose of 24 Gy (Serduc et al. 2008). In addition to that, MRT-induced tumor vascular damage can also affect tumor growth. It has been shown that peak doses of 75 Gy and 150 Gy are able to decrease the vascular density and reduce oxygenation resulting in a prominent tumor growth delay (Griffin et al. 2012). The damage of the tumor



vasculature can be long-lasting after applying an entrance dose of more than 100 Gy to tumors (Griffin et al. 2012; Bouchet et al. 2015). However, a dose of 20 Gy, which is in the range of the applied peak doses at the MuCLS, is able to induce only a transient damage of the vasculature of a xenograft tumor which subsequently recovers after some days (Kim et al. 2013). This indicates that a peak dose of 21 Gy or 35 Gy at the MuCLS could be too low for persistent damage of the tumor vasculature and thereby result in a reduced tumor growth inhibition. However, a solid conclusion of a tumor growth inhibition of microbeam irradiation at the MuCLS at 3 Gy and 5 Gy can only be drawn, if more animals will be irradiated with microbeams and broadbeams.

Furthermore, our MRT study gives a hint that there is an increased tumor growth inhibition after applying a high integral dose of 5 Gy compared to an integral dose of 3 Gy. It was measured for both treatment modalities. Although this observation cannot be proven statistically due to the low number of animals per treatment group, it is in line with the study of Dilmanian et al. (2002) demonstrating a higher tumor control after delivering of higher peak doses and using a constant valley dose.

In our study, tumors were irradiated with 50  $\mu\text{m}$  wide microbeams which were separated by 350  $\mu\text{m}$ . The paths of microbeams can be detected by staining of  $\gamma\text{H2AX}$  which is known as DNA double-strand break marker (Fernandez-Palomo et al. 2015). The width and the spacing between two adjacent microbeams agree to the  $\gamma\text{H2AX}$  positively stained paths on ear sections. The immunohistochemical staining of  $\gamma\text{H2AX}$  also shows that there is no blurring of microbeams present. Blurring of microbeams, which results in broader beam widths and lower peak-to-valley dose ratios, can happen due to respiration-induced tumor motion (Chtcheprov et al. 2014). Motion effects are more likely observed when abdominal tumors (e.g. in liver or brain) are irradiated (Serduc et al. 2010; Chtcheprov et al. 2014). At synchrotrons, motion blur can be reduced due to ultra-high dose rates of more than 100 Gy/s (Chtcheprov et al. 2014). Treating different targets, motion during microbeam irradiation at low dose rates might play an important role, which has not yet been investigated.

A technical limitation of our study was the small circular irradiation field of 2.3 mm in diameter which corresponds to the maximum tumor size plus a safety margin to irradiate. This tumor size is small compared to tumor sizes which are conventionally irradiated in tumor growth delay assays in the hind limb. Subcutaneous tumors in the hind limb have typically a size of about  $8 \times 4 \text{ mm}^2$  on day of irradiation (Zlobinskaya et al. 2014). The recently developed mouse model for growth delay studies of small subcutaneous tumors is the mouse ear tumor model where tumor cells were injected subcutaneously in the ear. This mouse ear tumor model allows the irradiation of tumors with a minimum size

of 2 mm (Oppelt et al. 2015). Moreover, mouse ears have the advantage of a small thickness of about 215–250  $\mu\text{m}$  (Girst et al. 2016; Dombrowsky et al. 2019) which allows penetration of low energy X-rays and thus, the treatment of shallow-seated tumors. In previous studies, the mouse ear tumor model showed a stable and high tumor take rate (Beyreuther et al. 2017). A tumor take rate of around 100% has been recorded after inoculation of FaDu cells combined with pure matrigel (Beyreuther et al. 2017). In our pilot-study, we observed a quiet high tumor take rate of 87.5%. However, it was reduced to 77% in the growth delay study at the MuCLS. This difference could be explained by failure in handling such as a lower injected cell concentration or inadequate mixture of cell suspension before injection. A well-known drawback of the FaDu tumor mouse ear model is a high risk of secondary tumors (Beyreuther et al. 2017). In our study, secondary tumors developed at neck or base of the right ear in 20% of all inoculated mice.

It has been shown that tumor growth can be delayed within a dose range of 3.8 Gy to 7.9 Gy after 200 kV X-rays (Beyreuther et al. 2017). In line with these results, our study at the MuCLS demonstrates that doses of 3 Gy and 5 Gy of broadbeam irradiations seems to be able to delay tumor growth at the considerably lower X-ray energy of 25 keV. However, a reliable conclusion can only be drawn as soon as more animals will be irradiated. The single sham-irradiated tumor at the MuCLS reached the 15-fold initial volume on day 21 after irradiation. In contrast to that, at the SARRP control tumors reached the abort criterion on day 12 for the latest. The slower tumor growth in the MuCLS study might be ascribed to a stressful handling due to transportation from the animal house to the radiation facility and vice versa. Another reason for a disturbed tumor growth could be the animal housing under quarantine conditions after irradiation at the MuCLS.

The low dose rate of compact X-ray sources is often discussed as a restriction of performing MRT in mouse models (Yuan et al. 2015; Bartzsch and Oelfke 2017). The CLS can be operated with a dose rate of 0.6 Gy/min for MRT which is in a comparable range of other novel compact microbeam sources, such as the carbon nanotube-based irradiator with a dose rate of 1.2 Gy/min (Yuan et al. 2015). Due to recently installed system upgrades at the MuCLS, higher dose rates are expected for future experiments. Nevertheless, the feasible dose rates of compact X-ray sources are much lower than the ultra-high dose rates of hundreds of Gray per second typically used in MRT studies at synchrotron facilities (Fardone et al. 2018). Despite the much lower dose rate at the MuCLS, our study gives a hint that the tumor volume growth could be reduced after microbeam irradiation at both 3 Gy and 5 Gy. Most previous experiments on the dose rate showed that dose rate effects become relevant for dose rates below 1 Gy/min (Joiner and Van der Kogel 2009) and

exposure time above around 10 min. For this reason, dose rate effects play a negligible role in our experiment at the MuCLS. For future studies, further technical improvements which are partially already implemented should achieve an increase in size of the irradiation field, higher dose rates and peak doses for comparable MRT studies at compact X-ray sources and synchrotron facilities.

In conclusion, this proof of principle experiment introduces a novel compact X-ray source for preclinical MRT studies. The tumoricidal effect of MRT, even at low peak and valley doses, delivered by the CLS can be expected but needs to be proven with a higher number of animals. These findings deliver important insights into the necessary dose delivery of microbeam irradiations at compact microbeam sources.

**Acknowledgements** This work has been supported by the Deutsche Forschungsgemeinschaft (MAP C.3.4, CALA) Cluster of Excellence: Munich-Centre for Advanced Photonics as well as the Munich School of BioEngineering of the Technical University of Munich. This work was also supported by the Centre of Advanced Laser Applications with respect to resources necessary for and at the Munich Compact Light Source.

## Compliance with ethical standards

**Conflict of interest** The authors declare they have no actual or potential competing financial interests.

**Ethical approval** All applicable national and institutional guidelines for the care and use of animals were followed. All procedures performed in this study involving animals were in accordance with ethical standards of the institution at which the study was conducted (project license 55.2-1-54-2531-62-2016).

## References

- Anschel DJ, Romanelli P, Benveniste H, Foerster B, Kalef-Ezra J, Zhong Z, Dilmanian FA (2007) Evolution of a focal brain lesion produced by interlaced microplanar X-rays. *Minim Invasive Neurosurg* 50:43–46. <https://doi.org/10.1055/s-2007-976514>
- Archer J, Li E, Petasecca M, Dipuglia A, Cameron M, Stevenson A, Hall C, Hausermann D, Rosenfeld A, Lerch M (2017) X-ray microbeam measurements with a high resolution scintillator fibre-optic dosimeter. *Sci Rep* 7:12450. <https://doi.org/10.1038/s41598-017-12697-6>
- Bartzsch S, Oelfke U (2017) Line focus X-ray tubes—a new concept to produce high brilliance X-rays. *Phys Med Biol* 62:8600–8615. <https://doi.org/10.1088/1361-6560/aa910b>
- Beyreuther E, Bruchner K, Krause M, Schmidt M, Szabo R, Pawelke J (2017) An optimized small animal tumour model for experimentation with low energy protons. *PLoS One* 12:e0177428. <https://doi.org/10.1371/journal.pone.0177428>
- Bouchet A, Lemasson B, Le Duc G, Maisin C, Bräuer-Krisch E, Siegbahn EA, Renaud L, Khalil E, Rémy C, Poillot C, Bravin A, Laissue JA, Barbier EL, Serduc R (2010) Preferential effect of synchrotron microbeam radiation therapy on intracerebral 9L gliosarcoma vascular networks international. *J Radiat Oncol Biol Phys* 78:1503–1512. <https://doi.org/10.1016/j.ijrobp.2010.06.021>
- Bouchet A, Serduc R, Laissue JA, Djonov V (2015) Effects of microbeam radiation therapy on normal and tumoral blood vessels. *Phys Med* 31:634–641. <https://doi.org/10.1016/j.ejmp.2015.04.014>
- Bouchet A, Brauer-Krisch E, Prezado Y, El Atifi M, Rogalev L, Le Clec'h C, Laissue JA, Pelletier L, Le Duc G (2016) Better efficacy of synchrotron spatially microfractionated radiation therapy than uniform radiation therapy on glioma. *Int J Radiat Oncol Biol Phys* 95:1485–1494. <https://doi.org/10.1016/j.ijrobp.2016.03.040>
- Burger K, Ilicic K, Dierolf M, Gunther B, Walsh DWM, Schmid E, Ettl E, Achterhold K, Gleich B, Combs SE, Molls M, Schmid TE, Pfeiffer F, Wilkens JJ (2017) Increased cell survival and cytogenetic integrity by spatial dose redistribution at a compact synchrotron X-ray source. *PLoS One* 12:e0186005. <https://doi.org/10.1371/journal.pone.0186005>
- Chitchev P, Burk L, Yuan H, Inscoc C, Ger R, Hadsell M, Lu J, Zhang L, Chang S, Zhou O (2014) Physiologically gated microbeam radiation using a field emission X-ray source array. *Med Phys* 41:081705. <https://doi.org/10.1118/1.4886015>
- Crosbie JC, Anderson RL, Rothkamm K, Restall CM, Cann L, Ruwamura S, Meachem S, Yagi N, Svalbe I, Lewis RA, Williams BRG, Rogers PAW (2010) Tumor cell response to synchrotron microbeam radiation therapy differs markedly from cells in normal tissues. *Int J Radiat Oncol Biol Phys* 77:886–894. <https://doi.org/10.1016/j.ijrobp.2010.01.035>
- Dilmanian FA, Button TM, Le Duc G, Zhong N, Pena LA, Smith JA, Martinez SR, Bacarian T, Tammam J, Ren B, Farmer PM, Kalef-Ezra J, Micca PL, Nawrocky MM, Niederer JA, Recksiek FP, Fuchs A, Rosen EM (2002) Response of rat intracranial 9L gliosarcoma to microbeam radiation therapy. *Neurooncology* 4:26–38
- Dilmanian FA, Zhong Z, Bacarian T, Benveniste H, Romanelli P, Wang R, Welwart J, Yuasa T, Rosen EM, Ansel DJ (2006) Interlaced X-ray microplanar beams: a radiosurgery approach with clinical potential. *Proc Natl Acad Sci USA*. <https://doi.org/10.1073/pnas.0603567103>
- Dilmanian FA, Qu Y, Feinendegen LE, Pena LA, Bacarian T, Henn FA, Kalef-Ezra J, Liu S, Zhong Z, McDonald JW (2007) Tissue-sparing effect of X-ray microplanar beams particularly in the CNS: is a bystander effect involved? *Exp Hematol* 35:69–77. <https://doi.org/10.1016/j.exphem.2007.01.014>
- Dombrowsky AC, Schauer J, Sammer M, Blutke A, Walsh DWM, Schwarz B, Bartzsch S, Feuchtinger A, Reindl J, Combs SE, Dollinger G, Schmid TE (2019) acute skin damage and late radiation-induced fibrosis and inflammation in murine ears after high-dose irradiation. *Cancers*. <https://doi.org/10.3390/cancers11050727>
- Ettl E, Dierolf M, Achterhold K, Jud C, Gunther B, Braig E, Gleich B, Pfeiffer F (2016) The Munich compact light source: initial performance measures. *J Synchrotron Radiat* 23:1137–1142. <https://doi.org/10.1107/s160057751600967x>
- Fardone E, Pouyatos B, Bräuer-Krisch E, Bartzsch S, Mathieu H, Requardt H, Bucci D, Barbone G, Coan P, Battaglia G, Le Duc G, Bravin A, Romanelli P (2018) Synchrotron-generated microbeams induce hippocampal transections in rats. *Sci Rep* 8:184. <https://doi.org/10.1038/s41598-017-18000-x>
- Favaudon V, Caplier L, Monceau V, Pouzoulet F, Sayarath M, Fouillade C, Poupon MF, Brito I, Hupe P, Bourhis J, Hall J, Fontaine JJ, Vozenin MC (2014) Ultrahigh dose-rate FLASH irradiation increases the differential response between normal and tumor tissue in mice. *Sci Transl Med* 6:245–293. <https://doi.org/10.1126/scitranslmed.3008973>
- Fernandez-Palomo C, Mothersill C, Bräuer-Krisch E, Laissue J, Seymour C, Schültke E (2015)  $\gamma$ -H2AX as a marker for dose deposition in the brain of Wistar rats after synchrotron microbeam radiation. *PLoS One* 10:e0119924. <https://doi.org/10.1371/journal.pone.0119924>
- Gil S, Sarun S, Biete A, Prezado Y, Sabés M (2011) Survival Analysis of F98 glioma rat cells following minibeam or broad-beam

- synchrotron radiation therapy. *Radiat Oncol* 6:1–9. <https://doi.org/10.1186/1748-717x-6-37>
- Girst S, Greubel C, Reindl J, Siebenwirth C, Zlobinskaya O, Walsh DW, Ilicic K, Aichler M, Walch A, Wilkens JJ, Multhoff G, Dollinger G, Schmid TE (2016) Proton minibeam radiation therapy reduces side effects in an in vivo mouse ear model. *Int J Radiat Oncol Biol Phys* 95:234–241. <https://doi.org/10.1016/j.ijrobp.2015.10.020>
- Griffin RJ, Koonce NA, Dings RP, Siegel E, Moros EG, Brauer-Krisch E, Corry PM (2012) Microbeam radiation therapy alters vascular architecture and tumor oxygenation and is enhanced by a galectin-1 targeted anti-angiogenic peptide. *Radiat Res* 177:804–812
- Hadsell M, Zhang J, Laganis P, Sprenger F, Shan J, Zhang L, Burk L, Yuan H, Chang S, Lu J, Zhou O (2013) A first generation compact microbeam radiation therapy system based on carbon nanotube X-ray technology. *Appl Phys Lett* 103:183505. <https://doi.org/10.1063/1.4826587>
- Ibrahim MJ, Crosbie JC, Yang Y, Zaitseva M, Stevenson AW, Rogers PA, Paiva P (2014) An evaluation of dose equivalence between synchrotron microbeam radiation therapy and conventional broad beam radiation using clonogenic and cell impedance assays. *PLoS One* 9:e100547. <https://doi.org/10.1371/journal.pone.0100547>
- Jacquet M, Suortti P (2015) Radiation therapy at compact compact sources. *Phys Med* 31:596–600. <https://doi.org/10.1016/j.ejmp.2015.02.010>
- Joiner M, Van der Kogel A (2009) *Basic clinical radiobiology*, 4th edn. Hodder Education, London
- Kim JW, Lee DW, Choi WH, Jeon YR, Kim SH, Cho H, Lee EJ, Hong ZY, Lee WJ, Cho J (2013) Development of a porcine skin injury model and characterization of the dose-dependent response to high-dose radiation. *J Radiat Res* 54:823–831. <https://doi.org/10.1093/jrr/rrt016>
- Kinner A, Wu W, Staudt C, Iliakis G (2008) Gamma-H2AX in recognition and signaling of DNA double-strand breaks in the context of chromatin. *Nucleic Acids Res* 36:5678–5694. <https://doi.org/10.1093/nar/gkn550>
- Laissue JA, Geiser G, Spanne PO, Dilmanian FA, Gebbers JO, Geiser M, Wu XY, Makar MS, Micca PL, Nawrocky MM, Joel DD, Slatkin DN (1998) Neuropathology of ablation of rat gliosarcomas and contiguous brain tissues using a microplanar beam of synchrotron-wiggler-generated X-rays. *Int J Cancer* 78:654–660. [https://doi.org/10.1002/\(sici\)1097-0215\(19981123\)78:5%3c654::aid-ijc21%3e3.0.co;2-l](https://doi.org/10.1002/(sici)1097-0215(19981123)78:5%3c654::aid-ijc21%3e3.0.co;2-l)
- Oppelt M, Baumann M, Bergmann R, Beyreuther E, Brüchner K, Hartmann J, Karsch L, Krause M, Laschinsky L, Leßmann E, Nicolai M, Reuter M, Richter C, Sävert A, Schnell M, Schürer M, Woithe J, Kaluza M, Pawelke J (2015) Comparison study of in vivo dose response to laser-driven versus conventional electron beam. *Radiat Environ Biophys* 54:155–166. <https://doi.org/10.1007/s00411-014-0582-1>
- Prezado Y, Fois G, Le Duc G, Bravin A (2009) Gadolinium dose enhancement studies in microbeam radiation therapy. *Med Phys* 36:3568–3574. <https://doi.org/10.1118/1.3166186>
- Regnard P, Le Duc G, Brauer-Krisch E, Tropes I, Siegbahn EA, Kusak A, Clair C, Bernard H, Dallery D, Laissue JA, Bravin A (2008) Irradiation of intracerebral 9L gliosarcoma by a single array of microplanar X-ray beams from a synchrotron: balance between curing and sparing. *Phys Med Biol* 53:861–878. <https://doi.org/10.1088/0031-9155/53/4/003>
- Sabatasso S, Laissue JA, Hlushchuk R, Graber W, Bravin A, Brauer-Krisch E, Corde S, Blattmann H, Gruber G, Djonov V (2011) Microbeam radiation-induced tissue damage depends on the stage of vascular maturation. *Int J Radiat Oncol Biol Phys* 80:1522–1532. <https://doi.org/10.1016/j.ijrobp.2011.03.018>
- Schleede S, Bech M, Achterhold K, Potdevin G, Gifford M, Loewen R, Limborg C, Ruth R, Pfeiffer F (2012a) Multimodal hard X-ray imaging of a mammography phantom at a compact synchrotron light source. *J Synchrotron Radiat* 19:525–529. <https://doi.org/10.1107/s0909049512017682>
- Schleede S, Meinel FG, Bech M, Herzen J, Achterhold K, Potdevin G, Malecki A, Adam-Neumair S, Thieme SF, Bamberg F, Nikolaou K, Bohla A, Yildirim AO, Loewen R, Gifford M, Ruth R, Eickelberg O, Reiser M, Pfeiffer F (2012b) Emphysema diagnosis using X-ray dark-field imaging at a laser-driven compact synchrotron light source. *Proc Natl Acad Sci USA* 109:17880–17885. <https://doi.org/10.1073/pnas.1206684109>
- Serduc R, Christen T, Laissue J, Faron R, Bouchet A, Sanden B, Segebarth C, Brauer-Krisch E, Le Duc G, Bravin A, Remy C, Barbier EL (2008) Brain tumor vessel response to synchrotron microbeam radiation therapy: a short-term in vivo study. *Phys Med Biol* 53:3609–3622. <https://doi.org/10.1088/0031-9155/53/13/015>
- Serduc R, Bouchet A, Brauer-Krisch E, Laissue JA, Spiga J, Sarun S, Bravin A, Fonta C, Renaud L, Boutonnat J, Siegbahn EA, Esteve F, Le Duc G (2009) Synchrotron microbeam radiation therapy for rat brain tumor palliation-influence of the microbeam width at constant valley dose. *Phys Med Biol* 54:6711–6724. <https://doi.org/10.1088/0031-9155/54/21/017>
- Serduc R, Brauer-Krisch E, Siegbahn EA, Bouchet A, Pouyatos B, Carron R, Pannetier N, Renaud L, Berruyer G, Nemoz C, Brochard T, Remy C, Barbier EL, Bravin A, Le Duc G, Depaulis A, Esteve F, Laissue JA (2010) High-precision radiosurgical dose delivery by interlaced microbeam arrays of high-flux low-energy synchrotron X-rays. *PLoS One* 5:e9028. <https://doi.org/10.1371/journal.pone.0009028>
- Slatkin DN, Spanne P, Dilmanian FA, Sandborg M (1992) Microbeam radiation therapy. *Med Phys* 19:1395–1400. <https://doi.org/10.1118/1.596771>
- Slatkin DN, Spanne P, Dilmanian FA, Gebbers JO, Laissue JA (1995) Subacute neuropathological effects of microplanar beams of X-rays from a synchrotron wiggler. *Proc Natl Acad Sci* 92:8783–8787
- Yuan H, Zhang L, Frank JE, Inscoe CR, Burk LM, Hadsell M, Lee YZ, Lu J, Chang S, Zhou O (2015) Treating brain tumor with microbeam radiation generated by a compact carbon-nanotube-based irradiator: initial radiation efficacy study. *Radiat Res* 184:322–333. <https://doi.org/10.1667/rr13919.1>
- Zhang L, Yuan H, Inscoe C, Chtcheprov P, Hadsell M, Lee Y, Lu J, Chang S, Zhou O (2014) Nanotube X-ray for cancer therapy: a compact microbeam radiation therapy system for brain tumor treatment. *Expert Rev Anticancer Ther* 14:1411–1418. <https://doi.org/10.1586/14737140.2014.978293>
- Zlobinskaya O, Siebenwirth C, Greubel C, Hable V, Hertenberger R, Humble N, Reinhardt S, Michalski D, Roper B, Multhoff G, Dollinger G, Wilkens JJ, Schmid TE (2014) The effects of ultra-high dose rate proton irradiation on growth delay in the treatment of human tumor xenografts in nude mice. *Radiat Res* 181:177–183. <https://doi.org/10.1667/rr13464.1>

**Publisher's Note** Springer Nature remains neutral with regard to jurisdictional claims in published maps and institutional affiliations.

## **3.2 Acute and late side effects after high-dose irradiation**

### **3.2.1 Aim and setup of the study**

Normal tissue complications are a common side effect after conventional RT. There are several approaches developed for the reduction of side effects in the normal tissue such as the temporal fractionation, the spatial fractionation (MBRT, MRT) and the use of protons or heavy ions. MBRT as spatial fractionation can be performed with protons. pMBRT increases the therapeutic index [122] because it enables a homogeneous tumor irradiation as in conventional RT [14]. Homogeneous dose coverage of tumors is achieved by lateral scattering of protons within the tissue which widens the beam [14]. However, the beam distances are preserved which conveys a sparing of the shallow normal tissue proximal to the tumor [14,59]. Therefore, pMBRT is suitable for the delivery of high doses in a fractionated regime (hypofractionation). This allows to further increase the lethal tumor dose while keeping the normal tissue toxicity decreased.

The aim of the doctoral thesis was to test the hypothesis that normal tissue complications depend on the irradiation accuracies of a radiation treatment which combines spatial fractionation with protons and temporal fractionation.

In this study, four fractions were delivered on consecutive days to the right healthy ear of Balb/c mice. Fractions of either BB X-rays (pilot study) or a pattern of proton minibeam patterns (main study) were administered. In the pilot study, a dose-response curve for early and late side effects of the skin was determined after fractionation X-ray RT using a fractional dose from 5 Gy to 30 Gy (chapter 3.2.2). In the main part of this study, a fractional dose of 30 Gy was used for hypofractionated pMBRT (chapter 3.2.3) investigating the dependency of the severity of acute and late side effects of the skin from the reirradiation position of minibeam patterns with different dose modulations.

### **3.2.2 Acute skin damage and late radiation-induced fibrosis and inflammation in murine ears after high-dose irradiation**

#### **3.2.2.1 Summary of the pilot study**

Several acute (erythema, desquamation, ear thickness) and late side effects (chronic inflammation, hyperplasia, hair follicle loss, fibrosis and the expression of its mediator TGF $\beta$ 1) were quantified for a period of 90 days after broadbeam X-ray irradiation at 0 Gy, 5 Gy, 10 Gy, 20 Gy and 30 Gy per fraction.

The comparison of four different fractional doses showed that the ear thickness increases with fractional dose. The maximum ear thickness is reached earlier the higher the fractional dose is. A dose-dependency is also observed for the erythema score but not for the desquamation score. The inflammation score increases significantly at 4x20 Gy and 4x30 Gy, while the number of hair follicles decreases significantly from 4x5 Gy on. A two-fold increased thickness of the epidermal layer (hyperplasia) is present after 4x30 Gy. The analysis of fibrosis as a late side effect showed that collagen is massively deposited in 4x30 Gy ears while the number of TGF $\beta$ 1-expressing cells increases only slightly with increasing dose per fraction. Furthermore, fibrosis correlates significantly with the fractional dose, the maximum ear thickness, and the severity of inflammation. The maximum ear thickness correlates with the severity of inflammation. However, the number of TGF $\beta$ 1-expressing cells does not correlate with the maximum ear thickness, fibrosis, and chronic inflammation.

In conclusion, there is a dose-dependency of ear thickness after hypofractionated X-ray RT. Ear thickness is also directly correlated with the severity of inflammation and hyperplasia as major contributors to acute ear thickness. Therefore, measuring ear thickness is a quantitative tool for acute side effects. In addition, there is a direct and dose-dependent link between fibrosis and chronic inflammation. They are responsible for chronic ear thickening. The severity of fibrosis also correlates with the maximum acute ear thickness enabling ear thickness as a predictor of late side effects. Furthermore, acute and late side effects are dose-dependent but still measurable at high doses of 30 Gy. This fractional dose allows the use of high-dose fractions in hypofractionated pMBRT.

### 3.2.2.2 Contributions

In collaboration with physicists Matthias Sammer and Jannis Schauer, I planned and prepared the experiment. Jannis Schauer and Matthias Sammer developed the mouse holder and implemented the setup for positioning of the ear. Dr. Stefan Bartzsch did the dosimetry at the conventional X-ray tube RS225. I had the main responsibility for the biological part of this experiment while Jannis Schauer and Matthias Sammer were responsible for the physical aspects. I conducted the irradiation at the RS225 with the support of Matthias Sammer, Jannis Schauer, Dr. Dieter Walsh, Marlon Stein, Benjamin Schwarz, Jessica Weigel and Prof. Dr. Thomas E. Schmid (fixation, irradiation, anesthesia). I conducted the scoring of early side effects with the help of Jannis Schauer during the follow-up period. I planned the histological analysis of the ear samples while the preparation of the histological samples and staining of slides was conducted by the Research Unit Analytical Pathology at the Helmholtz Center Munich (Dr. Andreas Blutke, Dr. Annette Feuchtinger).

I performed data analysis and interpretation. In addition, I wrote the manuscript except section 4.2 which was written by Jannis Schauer. Furthermore, Jannis Schauer designed figure 12. Dr. Andreas Blutke offered figure 13, while he also helped me to prepare figures 6, 7 and 8. Moreover, I designed all other figures, illustrations, and tables. All co-authors, but especially Matthias Sammer, Dr. Andreas Blutke, Prof. Dr. Thomas E. Schmid and Prof. Dr. Günther Dollinger contributed to the scientific discussion, data interpretation, and reviewed the manuscript.

### 3.2.2.3 Publication

The data were presented in the following original peer-reviewed research article on May 25<sup>th</sup> in 2019 in the Journal 'Cancers'.

#### ***Acute Skin Damage and Late Radiation-Induced Fibrosis and Inflammation in Murine Ears after High-Dose Irradiation***

Annique C. Dombrowsky † , Jannis Schauer †, Matthias Sammer, Andreas Blutke, Dietrich W. M. Walsh, Benjamin Schwarz, Stefan Bartzsch, Annette Feuchtinger, Judith Reindl, Stephanie E. Combs, Günther Dollinger, Thomas E. Schmid

† contributed equally to this manuscript



Cancers 2019, 11, 727

DOI: 10.3390/cancers11050727



Article

# Acute Skin Damage and Late Radiation-Induced Fibrosis and Inflammation in Murine Ears after High-Dose Irradiation

Annique C. Dombrowsky <sup>1,2,†</sup> , Jannis Schauer <sup>3,†</sup>, Matthias Sammer <sup>3</sup>, Andreas Blutke <sup>4</sup>, Dietrich W. M. Walsh <sup>3,5,6</sup>, Benjamin Schwarz <sup>3</sup>, Stefan Bartzsch <sup>1,2</sup>, Annette Feuchtinger <sup>4</sup>, Judith Reindl <sup>3</sup>, Stephanie E. Combs <sup>1,2</sup>, Günther Dollinger <sup>3</sup> and Thomas E. Schmid <sup>1,2,\*</sup> 

<sup>1</sup> Institute for Radiation Medicine, Helmholtz Zentrum München GmbH, 85764 Neuherberg, Germany; annique.hunger@helmholtz-muenchen.de (A.C.D.); stefan.bartzsch@helmholtz-muenchen.de (S.B.); stephanie.combs@helmholtz-muenchen.de (S.E.C.)

<sup>2</sup> Department of Radiation Oncology, Technical University of Munich, School of Medicine, Klinikum rechts der Isar, 81675 Munich, Germany

<sup>3</sup> Institute for Applied Physics and Metrology, Universität der Bundeswehr München, 85577 Neubiberg, Germany; jannis.schauer@unibw.de (J.S.); matthias.sammer@unibw.de (M.S.); d.walsh@dkfz-heidelberg.de (D.W.M.W.); benjamin.schwarz@unibw.de (B.S.); judith.reindl@unibw.de (J.R.); guenther.dollinger@unibw.de (G.D.)

<sup>4</sup> Research Unit Analytical Pathology, Helmholtz Zentrum München GmbH, 85764 Neuherberg, Germany; andreas.parzefall@helmholtz-muenchen.de (A.B.); annette.feuchtinger@helmholtz-muenchen.de (A.F.)

<sup>5</sup> German Cancer Consortium, 69120 Heidelberg, Germany

<sup>6</sup> Clinical Cooperation Unit Translational Radiation Oncology, Heidelberg Ion Therapy Center (HIT), Heidelberg Institute of Radiation Oncology Heidelberg University Medical School and National Center for Tumor Diseases, German Cancer Research Center, 69120 Heidelberg, Germany

\* Correspondence: thomas.schmid@helmholtz-muenchen.de; Tel.: +49-89-3187-43040

† These authors share equal contribution.

Received: 27 April 2019; Accepted: 21 May 2019; Published: 25 May 2019



**Abstract:** The use of different scoring systems for radiation-induced toxicity limits comparability between studies. We examined dose-dependent tissue alterations following hypofractionated X-ray irradiation and evaluated their use as scoring criteria. Four dose fractions (0, 5, 10, 20, 30 Gy/fraction) were applied daily to ear pinnae. Acute effects (ear thickness, erythema, desquamation) were monitored for 92 days after fraction 1. Late effects (chronic inflammation, fibrosis) and the presence of transforming growth factor beta 1 (TGF $\beta$ 1)-expressing cells were quantified on day 92. The maximum ear thickness displayed a significant positive correlation with fractional dose. Increased ear thickness and erythema occurred simultaneously, followed by desquamation from day 10 onwards. A significant dose-dependency was observed for the severity of erythema, but not for desquamation. After 4  $\times$  20 and 4  $\times$  30 Gy, inflammation was significantly increased on day 92, whereas fibrosis and the abundance of TGF $\beta$ 1-expressing cells were only marginally increased after 4  $\times$  30 Gy. Ear thickness significantly correlated with the severity of inflammation and fibrosis on day 92, but not with the number of TGF $\beta$ 1-expressing cells. Fibrosis correlated significantly with inflammation and fractional dose. In conclusion, the parameter of ear thickness can be used as an objective, numerical and dose-dependent quantification criterion to characterize the severity of acute toxicity and allow for the prediction of late effects.

**Keywords:** hypofractionation; side effects; acute; late; high-dose; fractionated radiotherapy; skin

## 1. Introduction

At least half of all cancer patients receive ionizing radiation as part of their treatment [1–3]. Despite the effective tumor control of radiation therapy, the risk of acute and late side effects remains a main problem [4]. In humans, acute side effects develop within a few weeks of treatment [1] and usually last four to six weeks [4]. Late side effects manifest after a latent period of three months [5] to years [1] and may, in the worst cases, become chronic [4].

Early side effects of radiation therapy typically manifest in tissues with a high proliferative activity, such as the skin or the mucosae of the gastro-intestinal tract [6]. Cells of the basal layer of the epidermis of the skin are rapidly dividing and are therefore very prone to cell death upon radiation therapy [6,7]. Secondary to the death of basal cells, an inflammatory reaction evolves, resulting in an erythematous reaction [8]. Inflammation is the first acute response of the skin [6]. Dry desquamation is caused by fast cell production in the basal layers [9]. Moist desquamation appears after high doses of radiation because cell production in the basal layers cannot compensate for the loss of cells in the basal layers and exudate is released [9,10]. Moreover, hair follicle loss can occur as another early side effect [11]. Tissue regeneration occurs from surviving basal stem cells [10]. In contrast, radiation-induced late side effects are usually irreversible and may be progressive in severity [1]. Late damage of irradiated skin is mainly characterized by atrophy [12] and abnormal differentiation of keratinocytes [13]. However, the most prominent, long-term radiation-induced side effects of the skin are telangiectasia and fibrosis [12,14]. Clinically, patients with dermal fibrosis show signs of increased stiffness and thickening of the affected skin [15]. Mechanistically, the development of fibrosis results from an interplay of cytokines and different cell types. The early inflammatory phase is characterized by an infiltration of immune cells, which initiates the restoration of the damaged tissue [13]. In the subsequent proliferative phase, infiltrating macrophages induce a trans-differentiation of stromal fibroblasts into myofibroblasts by secretion of the transforming growth factor beta (TGF $\beta$ ) [15]. Myofibroblasts proliferate and secrete excessive collagen fibers and other extracellular matrix components (ECM) [15,16]. The ECM deposition is maintained over several years with a persistently elevated cytokine production [16]. Under normal circumstances of wound healing, the ECM expansion is provisional until the process of re-epithelialization occurs [17]. In the case of fibrosis, there is a pathological imbalance between synthesis and degradation of collagen [1]. Cytokine-driven ECM synthesis overbalances and culminates in fibrosis [16]. The main driver of the fibrotic process is the cytokine TGF $\beta$  [1], which is produced by different cell types, such as macrophages [15] or myofibroblasts [6]. TGF $\beta$  can be directly activated by ionizing radiation through dissociation of the latency-associated peptide [1]. TGF $\beta$  also plays an important role in activation, proliferation and differentiation of epithelial cells and fibroblasts into collagen-producing myofibroblasts [18]. In addition to a local expression of TGF $\beta$  at the exposed site, inflammatory cytokines are also systemically elevated after radiation treatment [19]. Cytokines that are highly concentrated in the plasma are able to induce radiation-related adverse effects in out-of-field organs. A systemic immune response activates immune cells in distant organs resulting in oxidative stress which can induce DNA damages and apoptosis in out-of-field normal tissue cells [19].

Side effects of the skin are observed in 90% of patients receiving radiation therapy [20]. Due to its clinical importance different scoring systems of acute radiation-induced side effects of the skin were developed. The most relevant scoring systems were introduced by the National Institutes of Health Common Toxicity Criteria-Adverse Event (CTCAE) and the Radiation Therapy Oncology Group (RTOG). These scoring systems assign radiation-induced side effects such as erythema and desquamation into four different severity grades [14,21]. A similar scoring system exists also for late radiation-induced morbidity (RTOG/EORTC) [21]. The scoring systems differ in the increments of the assigned grades [14]. For animal trials, the scoring systems are based on similar criteria as for humans, e.g., acute side effects in the skin such as erythema and desquamation can be assessed by different grades from no reaction to severe reaction in a mouse ear model [22,23]. However, a gold standard for the clinical rating of the severity of side effects in humans and animals still does not exist [14]. Therefore, different scoring systems have been used in clinical and experimental trials which hamper



comparability between different studies. The comparability is also limited by the subjective assessment of radiation-induced toxicities by scoring systems, which deliver no quantitative data. It has been shown in radiobiological experiments using mice that the ear thickness increases if acute skin damage occurs due to X-ray irradiation. The measurement of the ear thickness might be an objective criterion for acute radiodermatitis [22]. In addition to these previously mentioned limitations of conventional scoring systems for humans and experimental animals, the relationship between acute and late side effects is not well understood. There are only a few studies suggesting a correlation between both lung function [24] and TGF $\beta$ 1 expression [25], as acute reactions, correlate with pulmonary fibrosis as a late reaction. In the skin, a correlation between the number of atrophied hair follicles and the number of radiation-induced tumors was detected [24]. Clinical studies observed a relationship between acute and late toxicity in the gastrointestinal tract and in the skin after radiotherapy of prostate cancer [26] and breast cancer patients [27], respectively. In addition to that, a good correlation between acute and late skin effects was observed after fractionation in several mouse studies, e.g., desquamation (acute reaction) and necrosis (late reaction) [27]. Nevertheless, experimental data about a mechanistic relationship between acute and late side effects, especially in the skin, are rare despite the clinical importance of the skin, which is always affected by radiation because it is located at the beam entrance regardless of which tumor is irradiated [28].

Therefore, the aim of our study was to determine a correlation between acute and late side effects of the skin after a hypofractionated schedule. Doses up to 30 Gy per fraction were delivered daily to the skin for four consecutive days using a standardized mouse ear model, which allowed for quantification of acute and late radiation-induced side effects in the same animal model. Acute (ear thickness, erythema, and desquamation) and late side effects (fibrosis, chronic inflammation), and the abundance of TGF $\beta$ 1-expressing cells in the skin were assessed up to 92 days following the first fraction. Our results indicate a dose-dependent positive correlation of the severity of acute side effects with a maximum reaction around day 15 after the first fraction. It also marks ear thickness as a quantitative scoring criterion for acute radiation-induced side effects, which is able to predict late tissue reactions in the mouse ear model.

## 2. Results

### 2.1. Analysis of Erythema and Desquamation

The acute side effects erythema and desquamation were assessed independently in two different scores, depicted in Figure 1, during the follow-up period of 92 days after a hypofractionation schedule. Mouse ears were irradiated with four fractions with a fraction interval of 24 h. Fraction 1 was given on day 0, fraction 2 to 4 on days 1, 2 and 3, respectively (Figure 10).

Already one day after delivery of the first fraction, the erythema score increased (Figure 1A). This increase of the erythema score was present in all dose groups, even for sham-irradiations. During fixation of the ears in the mouse holder, ears were gently compressed which induced a flush of the skin. After fraction 2, 3 and 4 a further increase of the erythema score was measured which was more prominent for doses of 20 Gy and 30 Gy per fraction. This increase might be due to the combined effect of squashing and radiation, or longer fixation times due to longer irradiations for higher fractional doses. After completing irradiation (day 5–6), a prompt decrease of erythema was observed. The desquamation score remained unchanged during the time of irradiation.

On day 4 (first day after hypofractionated irradiation), the erythema score culminated at  $2.2 \pm 0.4$ ,  $2.6 \pm 0.3$ ,  $1.6 \pm 0.3$  and  $1.1 \pm 0.2$  for fractional doses of 30 Gy, 20 Gy, 10 Gy and 5 Gy, respectively. Sham-irradiated ears also showed a flush of the skin with a score of  $1.0 \pm 0.2$  on day 4, likely induced by the mechanical fixation of the ears. On day 6 the erythema score dropped down to  $1.8 \pm 0.3$ ,  $1.4 \pm 0.3$ ,  $1.3 \pm 0.2$ ,  $1.2 \pm 0.2$  and  $0.7 \pm 0.3$  on day 6 after four fractional doses of 30 Gy, 20 Gy, 10 Gy, 5 Gy and 0 Gy, respectively. A second increase of the erythema score appeared on day 15–16 with a score of  $1.4 \pm 0.1$  and  $1.4 \pm 0.3$  after both  $4 \times 30$  Gy and  $4 \times 20$  Gy (Table 1). After  $4 \times 10$  Gy and  $4 \times 5$  Gy

irradiations, an erythema score of  $1.0 \pm 0.2$  and  $0.6 \pm 0.4$  was seen with score maxima between day 20–22 and day 18, respectively. After sham-irradiation, the erythema score of sham-irradiated ears culminated with a score of  $0.4 \pm 0.1$  on day 12 and further decreased to  $0.0 \pm 0.0$  on day 22. After  $4 \times 5$ ,  $4 \times 10$  and  $4 \times 20$  Gy treatments, the erythema score decreased slowly to  $0.0 \pm 0.1$ , measured on day 34. On day 50, erythema also disappeared on  $4 \times 20$  Gy and  $4 \times 30$  Gy irradiated ears.

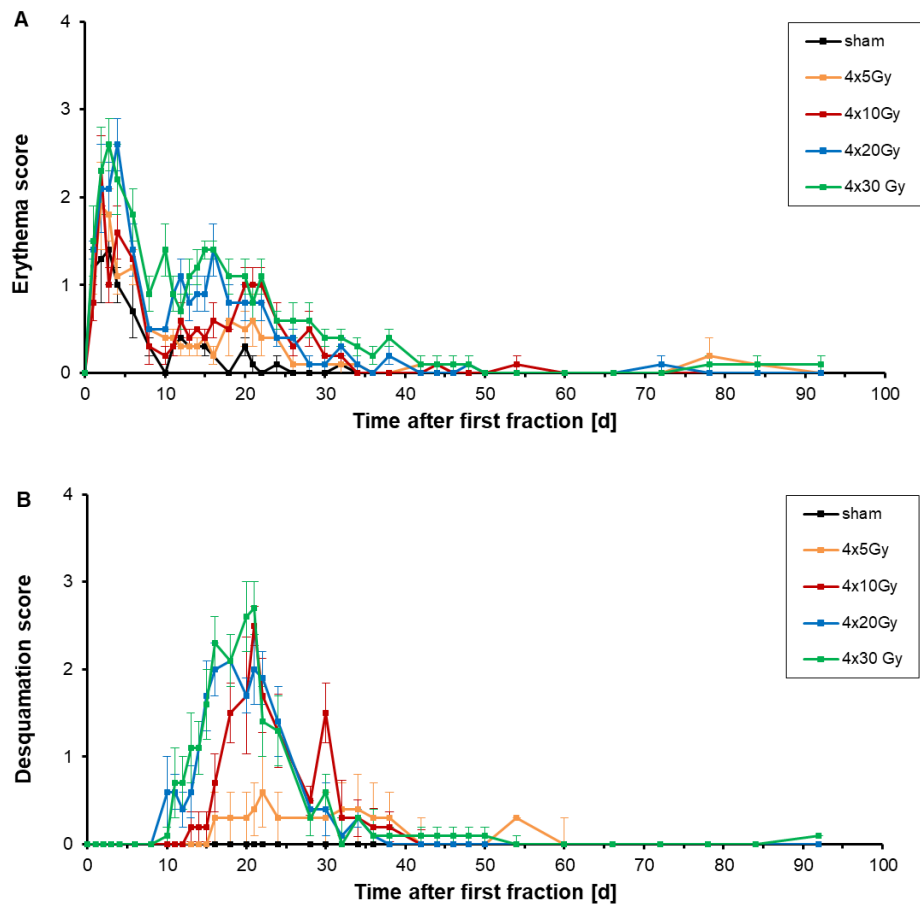


**Figure 1.** Semi-quantitative erythema score (A) and desquamation score (B) were measured on irradiated ears of 6–7 mice per dose group according to the grading scheme in Table 3 during the follow-up period of 92 days after a hypofractionation. Murine ears were irradiated with fractional doses of 0 Gy (black), 5 Gy (orange), 10 Gy (red), 20 Gy (blue) and 30 Gy (green). The error bars represent the standard errors of the mean (SEM).

**Table 1.** Maximum erythema score and desquamation score of ears after receiving a 4-fraction course with different X-ray doses. The time after the first fraction is illustrated at which either the erythema or desquamation score was maximal. The errors are given as the standard errors of the mean (SEM).

Dose (Gy)	Maximum Erythema Score ( $\mu\text{m}$ )	Time after First Fraction (d)	Maximum Desquamation Score ( $\mu\text{m}$ )	Time after First Fraction (d)
0 (sham)	$0.4 \pm 0.1$	12	$0.0 \pm 0.0$	-
$4 \times 5$	$0.6 \pm 0.4$	18	$0.6 \pm 0.4$	22
$4 \times 10$	$1.0 \pm 0.2$	20–22	$2.5 \pm 0.2$	21
$4 \times 20$	$1.4 \pm 0.3$	16	$2.1 \pm 0.3$	18
$4 \times 30$	$1.4 \pm 0.1$	15–16	$2.7 \pm 0.3$	21

An increase of the desquamation score appeared initially 10 days after the first fraction of either 20 Gy or 30 Gy (Figure 1B). The start of the increase of the desquamation score was delayed when lower doses were delivered, e.g., 13 days after the first fraction of 10 Gy. Using doses of 30 Gy, 20 Gy, 10 Gy and 5 Gy per fraction the maximum score of desquamation was measured 21 days, 18 days, 21 days and 22 days upon the first fraction, respectively (Table 1). The observed desquamation was always dry and never developed into a moist desquamation.

As a conclusion, erythema is dose-dependent: the higher the dose per fraction the more pronounced and earlier the erythema develops. The severity of desquamation is apparently different between lower fractional doses of 5 Gy and fractional doses higher than 10 Gy, but the difference in severity between the high fractional doses is marginal. The evaluation of erythema and desquamation is however subjective and requires a standardized scoring system. Therefore, it is not suitable for a reliable and comparable grading of acute toxicities.

## 2.2. Analysis of Ear Thickness

Acute intumescent inflammatory alterations (edema, vascular congestion, hyperemia) were assessed following hypofractionated X-ray radiation therapy by measuring the thickness of irradiated ears. Figure 2 shows the mean changes of the thickness of the right ears of 6–7 mice per dose group receiving four fractions with doses ranging from 0 Gy to 30 Gy per fraction.

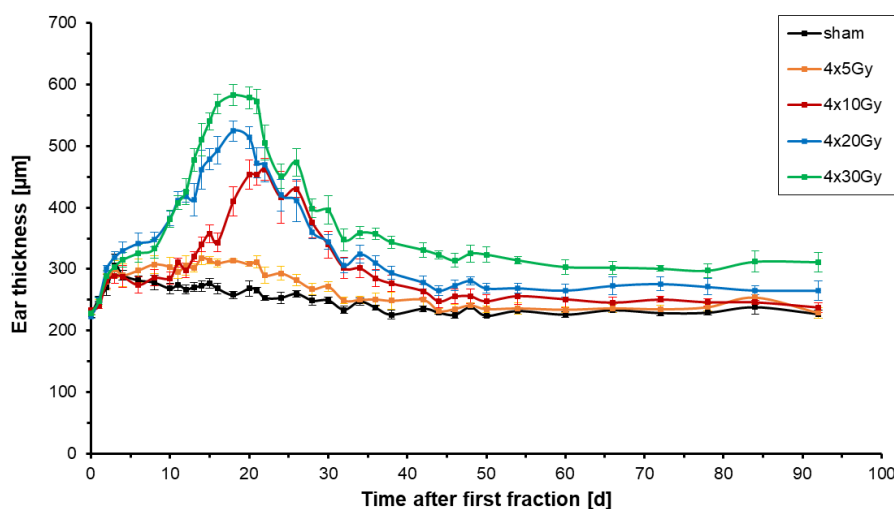


**Figure 2.** Thickness of irradiated right ears of mice after hypofractionated X-ray irradiation with a total of 4 fractions given every 24 h. Doses of 0 Gy (black), 5 Gy (orange), 10 Gy (red), 20 Gy (blue) or 30 Gy (green) per fraction were used per fraction. The plot shows the mean values for every dose group comprising 6–7 mice. The thickness of the irradiated ears was monitored for 92 days after the first fraction. The errors are given as the standard errors of the mean (SEM).

The left ear of each mouse served as a control and had a constant thickness of  $216.9 \pm 6.1 \mu\text{m}$ . In all treatment groups, all mice had a similar initial thickness of the right ear of  $227.6 \pm 3.7 \mu\text{m}$  (Figure 2). With the start of treatment, the mean thickness of sham-irradiated ears increased slightly by around  $80 \pm 18 \mu\text{m}$  on day 3 but then dropped down again on day 4 once sham-irradiation was completed. The ears were gently compressed during the fixation in the mouse holder. The repetition of the mechanical stress on every day of irradiation caused a culmination of ear thickness to a maximum on day 3 (last day of irradiation). During the follow-up period of 92 days sham-irradiated ears reached a maximum thickness of  $276.7 \pm 15 \mu\text{m}$  on day 15 (Table 2) and returned to their initial thickness of around  $230 \mu\text{m}$  on day 30 which remained constant from that day on.

**Table 2.** Maximum thickness of murine ears after receiving a four-fraction course with different X-ray doses. The time of maximal ear thickness is given for every dose group. The errors are given as the standard errors of the mean (SEM).

Dose (Gy)	Maximum of Ear Thickness ( $\mu\text{m}$ )	Time after First Fraction (d)
0 (sham)	276.7 $\pm$ 15.0	15
4 $\times$ 5	317.9 $\pm$ 8.2	14
4 $\times$ 10	461.9 $\pm$ 17.8	22
4 $\times$ 20	524.5 $\pm$ 16.5	18
4 $\times$ 30	582.4 $\pm$ 16.9	18

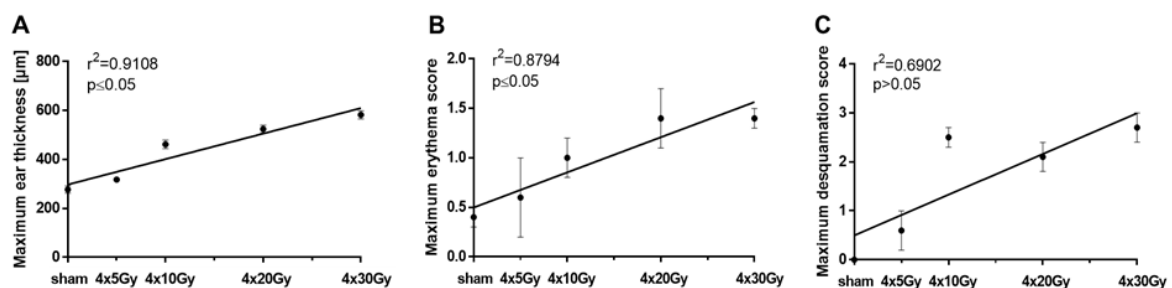
All doses used in the X-ray fractions induced an increase of thickness of the right ear. After the first minor rise of ear thickness due to mechanical stress the ear thickness peaked 18 days after both 4  $\times$  30 Gy and 4  $\times$  20 Gy, and 22 days after 4  $\times$  10 Gy (Table 2). After four fractions of 5 Gy, the ear thickness reached a plateau from day 14 onwards. Hypofractionation with four fractions of 30 Gy, 20 Gy, 10 Gy and 5 Gy led to an increase of ear thickness of 2.5, 2.4, 2.0 and 1.4 times the initial thickness, respectively. During the follow-up period, the thickness of irradiated ears decreased slowly to 250  $\pm$  9.8  $\mu\text{m}$  for 4  $\times$  5 Gy, 250  $\pm$  3.5  $\mu\text{m}$  for 4  $\times$  10 Gy, 265  $\pm$  7.4  $\mu\text{m}$  for 4  $\times$  20 Gy, and 310  $\pm$  17.1  $\mu\text{m}$  for 4  $\times$  30 Gy on day 92. The ear thickness never returned to the initial thickness, if four fractional doses of 20 Gy or 30 Gy were applied, demonstrating chronic ear swelling as part of chronic inflammation.

For all irradiation groups, it was observable that the temporal course of the radiation response was shifted to earlier time points for higher doses per fraction; the higher the dose per fraction the earlier the maximum ear thickness was reached and the stronger the ear swelling was present. In conclusion, ear thickness is a direct measurement of acute responses to radiation.

### 2.3. Dose-Dependency of the Maximum Ear Thickness, the Maximum Erythema and Desquamation Score

In Figure 3A, the maximum ear thickness is plotted against the dose per fraction. It depicts that the maximum swelling correlated linearly ( $y = 10.42 \cdot x + 297.2$ ) with a significance of  $p \leq 0.05$  with the dose per fraction after a hypofractionated radiation treatment. Figure 3B shows that the maximum erythema score significantly ( $p \leq 0.05$ ) correlated with the dose of all used hypofractionation schedules ( $y = 0.04 \cdot x + 0.49$ ). Whereas there was no correlation between the maximum desquamation score and the doses per fraction ( $p > 0.05$ , Figure 3C).

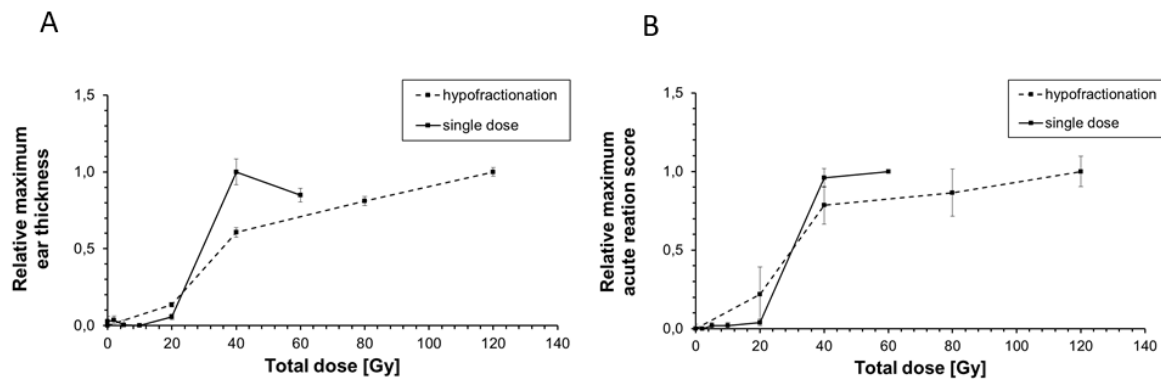
The higher the dose per fraction the thicker is the irradiated ear. The maximum thickness of irradiated ears is a dose-dependent measurement.



**Figure 3.** Comparison between the maximum ear thickness (A), the maximum erythema score (B) or the maximum desquamation score (C), and dose of irradiated ears after a 4-fraction course given one fraction per day. The days and the values on which the maximum erythema score, desquamation score and ear thickness were assessed are shown in Tables 1 and 2. Correlations were calculated using Spearman's correlation with linear regression. Significance levels are indicated. The errors are given as the standard errors of the mean (SEM).

#### 2.4. Comparison of the Maximum Acute Reaction Score and the Maximum Ear Thickness between Hypofractionated and Single X-ray Dose Irradiation

In a previously performed study by Girst et al., 2016 [22], ear thickness, erythema and desquamation as acute side effects were assessed after single dose X-ray irradiation of murine ears. Erythema score and desquamation score were combined to one acute reaction score (see Section 4.3). Here, we want to compare the severity of both ear thickness (Figure 4A), and the acute reaction score (Figure 4B) between hypofractionated and single dose irradiation. In Figure 4, relative values are illustrated in order to reduce a difference in the individual assessment of acute side effects.



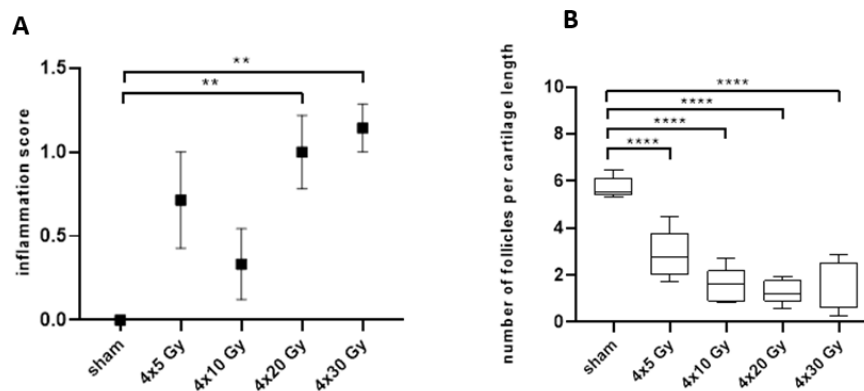
**Figure 4.** Comparison of the relative maximum ear thickness (A) and relative maximum acute reaction score (B) of murine ears after irradiation with both single (solid line) and hypofractionated (dashed line) X-ray doses. The maximum measured ear thickness (Table 2) and the maximum acute reaction score (Table 1) were set to 1, the minimal ones to 0 in order to calculate the relative values. For single dose irradiation, the maximum ear thickness and the maximum acute reaction score were used from Girst et al., 2016 [22] using X-ray doses of 0 Gy, 2 Gy, 5 Gy, 10 Gy, 20 Gy, 40 Gy and 60 Gy. For hypofractionation, the maximum erythema score and the maximum desquamation score (Figure 1) were summed up to an acute reaction score. The total doses of 20 Gy, 40 Gy, 80 Gy and 120 Gy correspond to the used four fractional doses of 5 Gy, 10 Gy, 20 Gy and 30 Gy, respectively. The errors are given as the standard errors of the mean (SEM).

Figure 4A shows that a single dose of 40 Gy ( $1 \times 40$  Gy) induced a relative maximum ear thickness of  $1.0 \pm 0.08$  while  $4 \times 10$  Gy which corresponds to a total dose of 40 Gy induced a lower relative maximum ear thickness of  $0.61 \pm 0.03$ . After  $4 \times 10$  Gy a similar reduction of the maximum acute reaction score was measured compared to that after  $1 \times 40$  Gy ( $0.78 \pm 0.1$  vs.  $0.96 \pm 0.06$ , Figure 4B). In contrast to that, there was only a marginal difference of the maximum ear thickness of about 0.08 between  $4 \times 5$  Gy (total dose of 20 Gy) and  $1 \times 20$  Gy despite the same total dose was delivered. At higher doses, the delivering of  $4 \times 20$  Gy (total dose of 80 Gy) to murine ear resulted in an ear thickness of  $0.81 \pm 0.03$  and acute reaction score of  $0.87 \pm 0.15$ . The same maximum ear thickness of  $0.85 \pm 0.04$  was measured after  $1 \times 60$  Gy despite 20 Gy less was applied. A similar maximum acute reaction score of 1.0 was observed for single doses higher than 40 Gy ( $0.96 \pm 0.06$ ) and total doses of 120 Gy ( $4 \times 30$  Gy,  $1.0 \pm 0.09$ ) indicating that a much higher dose is necessary to observe both the same maximum ear thickness and acute reaction score in the murine ear skin if hypofractionation is used.

#### 2.5. Histopathological Analyses of Irradiated Ears

In addition to the assessment of acute side effects in the skin, late irradiation-induced side effects were also examined by qualitative and quantitative histopathological analyses. In sections of the irradiated ears, the infiltration of inflammatory cells as a late radiation-induced side effect was acquired 92 days post-irradiation, using a semi-quantitative grading scheme (see Section 4.3). Figure 5A shows an increase of the inflammation score with increasing dose 92 days after hypofractionated radiotherapy. The frequency (i.e., number of affected animals) and severity of inflammatory lesions (grade 0 to

2) continuously increased in groups with increasing radiation doses. At day 92, the severity of inflammatory lesions significantly increased after four fractional doses of 20 Gy or 30 Gy demonstrating that a chronic inflammatory reaction has been developed.



**Figure 5.** Semi-quantitative analysis of the inflammation score (A) and quantification of hair follicle profiles within pre-defined region of interest. (B) in histological sections of irradiated ears on day 92 after sham-irradiation or a 4-fraction course with doses of 5 Gy, 10 Gy, 20 Gy and 30 Gy per fraction. One-way ANOVA with Kruskal-Wallis test and Dunn's post hoc test was used for statistical analysis. Asterisks indicate significant differences: \*\*  $p \leq 0.01$ , \*\*\*\*  $p \leq 0.0001$ .

The loss of hair follicles represents an additional, side effect of radiation [11]. In Figure 5B the number of section profiles of hair follicles within a defined region of interest (ROI) is displayed on day 92. There was a visible trend that the number of follicle profiles per ear section length decreased as the fractional dose increased. Already  $4 \times 5$  Gy resulted in a highly significant loss of follicle profiles per ROI. With increasing dose further from  $4 \times 10$  to  $4 \times 30$  Gy, the number of section profiles of hair follicles was further reduced, and follicle profiles were almost completely absent. The absence of hair follicle profiles at a late time point (e.g., day 92) indicates that the radiation-induced damage of hair follicles does not recover probably due to complete sterilization of stem cells in the hair bulb.

Pronounced epidermal hyperplasia was regularly present in ear sections after four doses of 30 Gy (Figure 6). While in low dose groups the thickness of the epidermal layer is comparable to sham-irradiated ears, an up to two-fold increase in dermal thickness was observed after  $4 \times 30$  Gy. As a conclusion, after high doses ( $>4 \times 10$  Gy) chronic side effects such as inflammation and epidermal hyperplasia are induced.



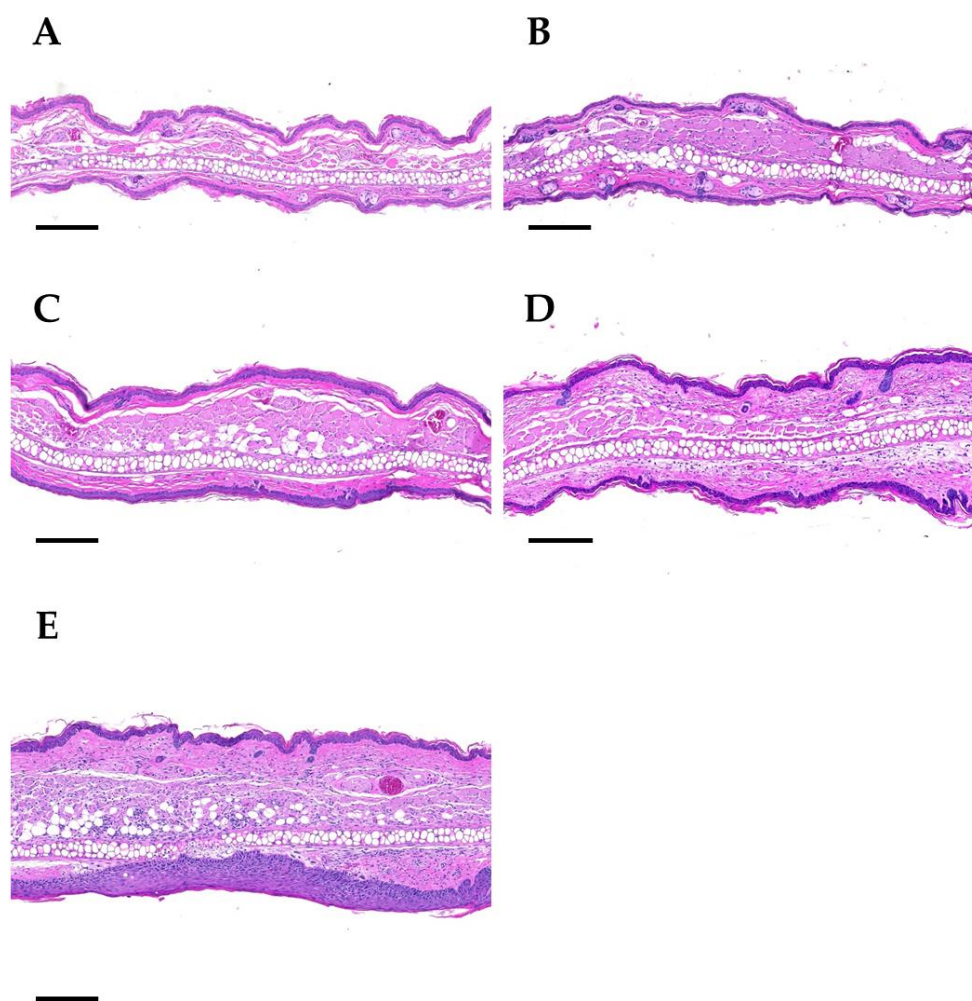


**Figure 6.** Representative histological images of ears on day 92 upon a 4-fraction course with different doses per fraction: sham (A), 5 Gy (B), 10 Gy (C), 20 Gy (D), 30 Gy (E). Panel A: Sham-irradiated. The central cartilage of the pinna is flanked by a layer of skeletal muscle, a dermal layer of moderate thickness and the epidermis. Hair follicles, nerves, sebaceous glands, and blood vessels are present. Panel B:  $4 \times 5$  Gy. The dermal layer of the ear skin is slightly thickened. Hair follicles are rarely present. Panel C:  $4 \times 10$  Gy. The dermal layer is further increased, and the epidermis is mildly hyperplastic. Hair follicle profiles are almost completely absent. No sebaceous glands are present. Panel D:  $4 \times 20$  Gy. The dermal layer of the skin is markedly thickened and infiltrated by a mixed population of inflammatory cells. No hair follicles and sebaceous glands are detectable. Panel E:  $4 \times 30$  Gy. The ear section displays severe dermal thickening and inflammatory cell infiltration, as well as marked epithelial hyperplasia. No hair follicles and sebaceous gland section profiles are present. Paraffin sections were stained with hematoxylin and eosin. Scale bar: 200  $\mu\text{m}$ .

### 2.6. Correlation of Acute and Late Side Effects after Hypofractionation

The results in the previous Sections 2.2 and 2.5 showed a strong increase of the dermal thickness of ears especially after receiving  $4 \times 30$  Gy. Therefore, we analyzed the extent of dermal fibrosis, as well as the abundance of TGF $\beta$ 1-expressing cells in irradiated ear sections.

Sirius red staining was used to visualize collagen in ear section on day 92 (Figure 7). Parallel to the increase of the ear thickness, the deposition of collagen fibers was increased after  $4 \times 10$  Gy and  $4 \times 20$  Gy. If  $4 \times 30$  Gy was applied, the collagen deposition is more pronounced contributing to a two-fold increase of the ear thickness. Due to this observation, we wanted to analyze the correlation

between acute side effects indicated as ear thickness, and late side effects such as fibrosis, the number of TGF $\beta$ 1-expressing cells and chronic inflammation.

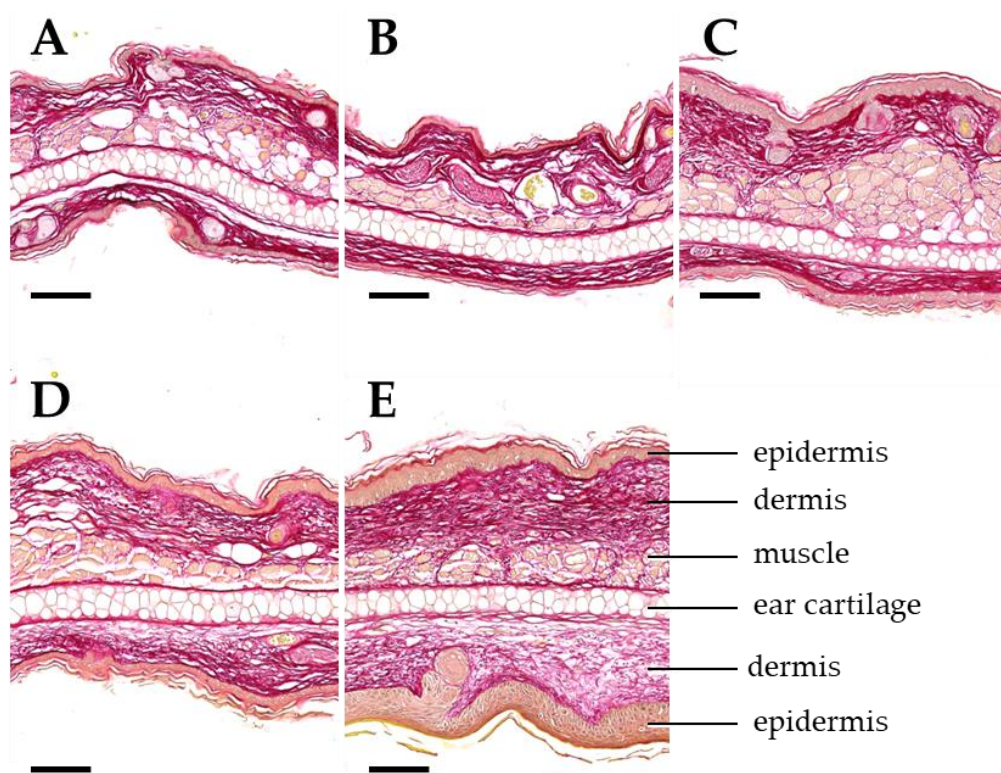


**Figure 7.** Dose-dependent development of dermal fibrosis. Representative images of ear sections on day 92 after a 4-fraction course using different doses per fraction: sham (A), 5 Gy (B), 10 Gy (C), 20 Gy (D), 30 Gy (E). Sections are stained with Sirius red for demonstration of collagenous connective tissue (dark red color). Important anatomical structures are indicated in E. Ear thickness and connective tissue deposition in the dermal layers of the ear skin increase with the radiation dose. Paraffin sections. Scale bar: 100  $\mu$ m.

Quantification of the number of TGF $\beta$ 1-expressing cells in histological ear sections on day 92 after hypofractionation showed that TGF $\beta$ 1 was mainly expressed by endothelial cells, intravascular immune cells as well as epidermal cells of the basal layer and dermal spindle cells (Figure 8). With increasing dose, the number of TGF $\beta$ 1-positive cell profiles slightly increased.

Collagen deposition in Sirius red stained ear sections was quantified as the fibrotic area per mm section length, using automated digital imaging analysis. The dose-dependency of both the fibrotic area and the number of TGF $\beta$ 1-positive cells per ROI is depicted in Figure 9a,b. With increasing dose per fraction, the fibrotic area per mm section width increases, but not the number of TGF $\beta$ 1-positive cells per ROI. The applied dose per fraction correlated significantly with fibrotic area ( $p \leq 0.01$ ), while there was no correlation with TGF $\beta$ 1 expression in irradiated ears ( $p > 0.05$ ).



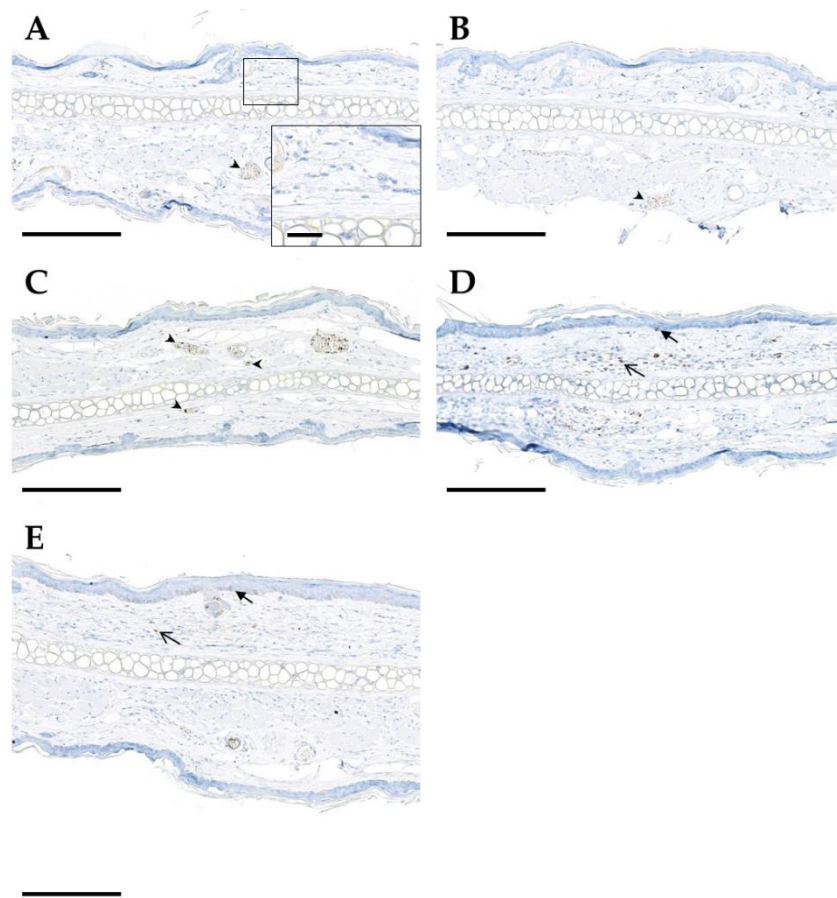


**Figure 8.** Immunohistochemical detection of TGF $\beta$ 1 (brown color) in mouse ear sections on day 92 following hypofractionation with different doses per fraction: sham (A), 5 Gy (B), 10 Gy (C), 20 Gy (D), 30 Gy (E). Positive endothelial and intravascular inflammatory cells are indicated by arrowheads, epidermal immunoreactivity by closed arrows, and immunoreactivity of dermal cells by open arrows. Paraffin sections of murine ears are shown. Chromogenic substrate: diaminobenzidine (DAB), nuclear counterstain: hematoxylin. Scale bar: 200  $\mu$ m (for zoom-in image 20  $\mu$ m).

Mouse ears irradiated with 5 Gy per fraction had a maximum thickness of  $317.9 \pm 8.2 \mu\text{m}$  (see Table 2) and a fibrotic area of  $411.1 \pm 174.8 \mu\text{m}^2$  and  $36 \pm 16$  TGF $\beta$ 1-positive cells per ROI. In mouse ears irradiated with a higher dose of 30 Gy per fraction with a maximum ear thickness of  $582.4 \pm 16.9 \mu\text{m}$  (Table 2) showed a fibrotic area of  $520.2 \pm 66.2 \mu\text{m}^2$  and  $50 \pm 18$  TGF $\beta$ 1-positive cells per ROI. Therefore, the size of fibrotic area in the skin is correlated with the maximum ear thickness ( $p \leq 0.05$ ), which is observed after irradiation using fractional doses from 0 Gy to 30 Gy (Figure 9c). However, there was no correlation between the number of TGF $\beta$ 1-positive cells and the maximum ear thickness ( $p > 0.05$ , Figure 9d). Moreover, the maximum ear thickness correlated with the inflammation score (Figure 9e), e.g., no inflammation was found in sham-irradiated ears with a thickness of  $276.7 \pm 15 \mu\text{m}$  (Table 2), but 100% of  $4 \times 30$  Gy irradiated ears with a thickness of  $582.4 \pm 16.9 \mu\text{m}$  showed an inflammation score of 1 and 2.

Since different types of inflammatory cells express TGF $\beta$ 1, it was of interest to evaluate, if there was a correlation between the number of TGF $\beta$ 1-expressing cells, fibrosis and inflammation on day 92 after hypofractionation. Our data show no correlation between the severity of fibrosis and the number of TGF $\beta$ 1-expressing immune cells present in the examined sections at the given time point ( $p > 0.05$ , Figure 9f), whereas there was a correlation between the fibrotic area and inflammation ( $p \leq 0.01$ , Figure 9g). The number of TGF $\beta$ 1-expressing cells was not correlated to the severity of inflammation (Figure 9h). In summary, there are significant correlations between the thickness of ears as an acute reaction, and fibrosis and inflammation score as late side effect on day 92.

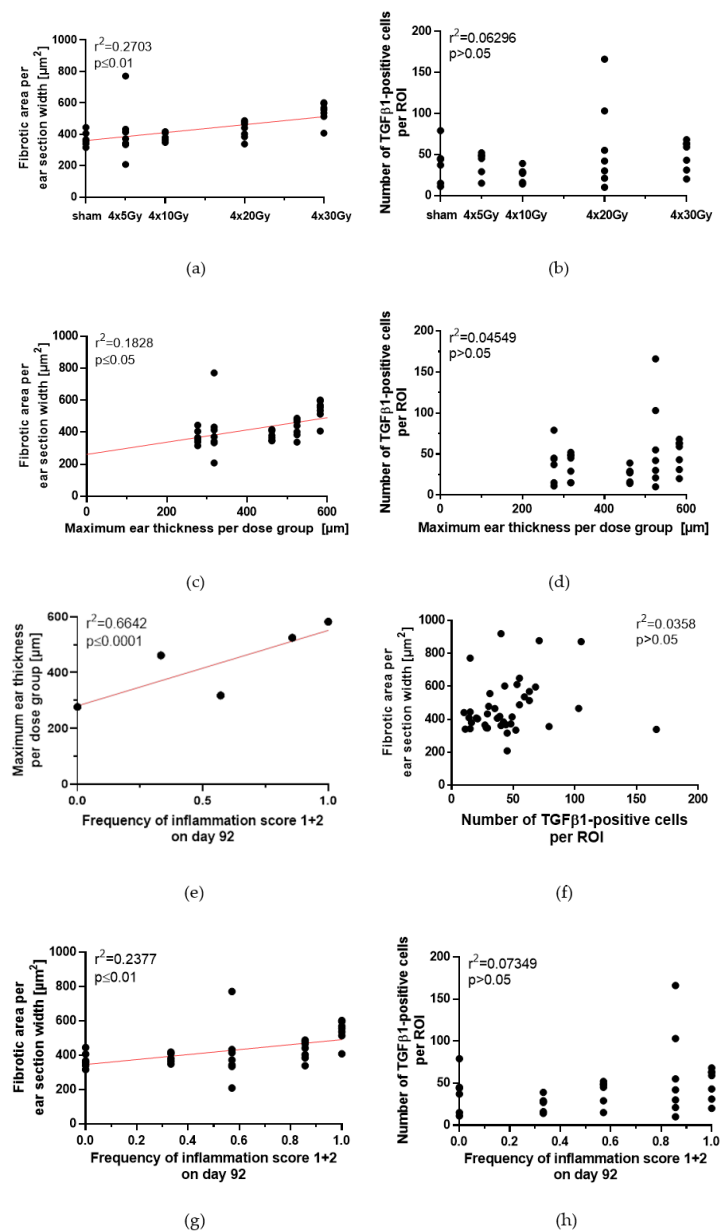


**Figure 9.** Quantification of the fibrotic area and the abundance of TGF $\beta$ 1-expressing cells in ear sections on day 92 following a 4-fraction course with different doses per fraction. Collagen was stained by Sirius red and TGF $\beta$ 1-expressing cells were identified by immunohistochemistry and quantified within the pre-defined ROI, using automated digital image analysis. (a) Correlation of the fibrotic area on day 92 with the dose per fraction. (b) Correlation of the number of TGF $\beta$ 1-expressing cells on day 92 with the dose per fraction. (c) Correlation of the fibrotic area with the maximum ear thickness during the acute reaction (see Section 2.2, Table 2). (d) Correlation of the number of TGF $\beta$ 1-expressing cells on day 92 with the maximum ear thickness during the acute reaction (see Section 2.2, Table 2). (e) Correlation between the maximum ear thickness as acute reaction (see Section 2.2, Table 2) and the frequency of both inflammation score 1 and 2 in all animals on day 92. (f) Correlation between fibrotic area and number of TGF $\beta$ 1-positive cells. (g) Correlation between fibrotic area and the frequency of both inflammation score 1 and 2 in all animals on day 92. (h) Correlation between number of TGF $\beta$ 1-expressing cells and the frequency of both inflammation score 1 and 2 in all animals on day 92. Correlations were calculated using Spearman's correlation with linear regression. Significance  $p$ -values are indicated.

### 3. Discussion

The use of different semi-quantitative scoring systems for acute and late side effects in patients and experimental animals does not allow for a reliable comparison between different studies. Moreover, there is no scoring criterion which allows for the prediction of the chance for occurrence and severity of late, possibly chronic side effects. The highest risk to develop side effects is in the skin, which is always irradiated during the treatment of deep-seated tumors. Therefore, in the present study, we examined the acute and late side effects of murine ears after a hypofractionation schedule with four daily fractions using doses from 0 Gy to 30 Gy per fraction. Our aim was to figure out whether the evaluation of acute side effects is able to predict the occurrence of late side effects after hypofractionation.

Our study demonstrates that the severity of the acute side effects, erythema and ear thickness, are significantly dose-dependent. Moreover, in contrast to erythema and desquamation, ear swelling represents a direct pendant of acute responses (edema, vascular congestion, hyperemia) to ionizing irradiation, and can adequately be quantified by measurement with a caliper. Therefore, ear swelling is suitable as a quantitative scoring criterion for acute side effects. Our study showed that quantitatively determined ear swelling as an acute side effect is significantly correlated with the fibrotic area and inflammation on day 92 after radiation exposure. Therefore, measuring the ear thickness can predict the development of late side effects in the skin at late time points after radiation treatment in the mouse ear model.

We quantified the area of deposited collagen in the ear sections as marker for fibrosis. Fibrosis correlated significantly with the applied dose which agrees to the result of another previously published study [15]. In the mouse ear model, fibrosis was quantified on day 92 (13 weeks post-irradiation). Comparable studies observed dermal fibrosis in mice at week 21 after irradiation with 35 Gy [29] or 12 weeks post-irradiation with doses up to 25 Gy of gamma-rays [30]. The differences between time points for measuring of fibrosis could be explained by the use of different mouse strains and different irradiated parts of the body, all differently prone to radiation-induced toxicities. These mouse studies delivered single doses in contrast to our hypofractionated schedule which is presumed to reduce toxicities. These results are well in line with our study in which no increased collagen deposition was observed in the mouse ear on day 92 after a dose up to  $4 \times 20$  Gy.

In addition to fibrosis, we quantified the number of TGF $\beta$ 1-expressing cells in ear sections. Our study does not show a correlation between ear swelling and the number of TGF $\beta$ 1-expressing cells per section ROI. However, there was a slight, but not significant increase in the cellular expression of TGF $\beta$ 1 but it was only detectable after  $4 \times 30$  Gy. Furthermore, the time point (92 days) for the quantification of TGF $\beta$ 1 may have been too early since fibrosis develops gradually after radiation exposure. Fibrosis represents the final result of a chronic inflammatory reaction [31]. There are three distinct increases of TGF $\beta$ 1 expression in murine skin [32]. After a first and a second wave at day 1–2 and day 14–28 post-irradiation, a third peak was observed after 9 months starting to elevate after three months [32]. We can infer from the study mentioned earlier that both a higher TGF $\beta$ 1 expression and thus higher collagen deposition might be detectable later than three months after hypofractionation. These findings are in agreement with the observed chronic inflammation (increase of the inflammation score) in murine ears on day 92 after hypofractionation. These increase number of inflammatory cell types might stimulate the development of fibrosis. Since fibrosis develops gradually over a prolonged period of several months after radiation therapy, we will quantify the fibrotic area and the tissue expression of TGF $\beta$ 1 at later time points after hypofractionation in a future experiment, also using quantitative RNA- and protein analysis.

Our study focused on the locally increased expression of TGF $\beta$ 1 in the ear. However the role of systemically increased TGF $\beta$ 1 cannot be neglected. It could be that TGF $\beta$ 1 circulating in the plasma of irradiated mice may activate immune cells in out-of-field organs as shown in previous studies by Ventura et al., 2017 [19] and activated inflammatory cells may promote oxidative stress, DNA damage and apoptosis in distant normal cells and in turn, it can also induce fibrosis and local inflammation in distant organs [19]. However, the systemic response of radiation exposure interplays with the

genetic background of the host [33]. Therefore, it needs to be elucidated whether TGF $\beta$ 1 is systemically increased and if it plays a distant role in the mouse ear model.

In addition to late side effects, we also evaluated the time course and the dose-dependency of acute side effects. It has been shown that erythema, as a cardinal symptom of acute inflammatory reactions, manifests as one of the first pathological signs of radiation [34]. Our data shows that the erythema score is already elevated after the first fraction. This early erythema might also be caused by the mechanical stress during ear fixation. However, the erythema score was still high at day 5 when the treatment was completed and consequently no daily exposure to mechanical stress was present anymore. A similar increase of the score of dorsal skin lesions with different maximum intensities was observed at day 7 after a single dose exposure of 20 Gy, 40 Gy and 80 Gy [35] which confirms the early onset of erythema and also the measured significant dose-dependency of the severity of erythema in murine ears. The increase of erythema score persisted for about two weeks for each dose. During this period, the desquamation score also starts to rise with increasing dose (not significant). Desquamation is a later acute pathological sign of radiation damage [14]. With an increasing dose, the advent of the desquamation reaction occurred later; it started to increase at day 10 after both  $4 \times 30$  Gy and  $4 \times 20$  Gy, at day 13 after  $4 \times 10$  Gy and at day 16 after  $4 \times 5$  Gy. A significant dose-dependent increase of the desquamation score was not detected in our study. Nevertheless, an increase dose-dependent progression of skin lesions was found in other mouse studies, observing desquamation at about day 14 after single dose exposure of 20 Gy, 40 Gy and 80 Gy [35] confirming the results of our study. Desquamation was resolved at around day 30 after doses below  $4 \times 20$  Gy as also shown in the mouse skin after irradiation with single doses of 20 Gy [22] and 30 Gy [36].

After hypofractionation, an increase of ear thickness was observed which culminated on day 18 with a thickness of about 600  $\mu$ m after  $4 \times 30$  Gy. This ear thickness is much lower compared to X-ray single dose irradiations in the same mouse ear model showing a maximum ear thickness of 900  $\mu$ m around day 25 after either 40 Gy or 60 Gy single doses [22]. When comparing the total doses which were delivered to murine ears during single dose and hypofractionated irradiation, a total dose below 20 Gy induced a similar increase in ear thickness and acute reaction score independent of the fractionation schedule. However, an increased sparing of the skin was observed at higher doses, e.g., a total dose of 40 Gy induced a less pronounced ear swelling and acute reaction score when X-rays were applied as a hypofractionated dose. To detect the same ear thickness or the same acute reaction score, a much higher X-ray dose can be delivered if murine ears are fractionally irradiated. The comparison of the ear thicknesses between both experiments should be done with caution. A difference in the individual scoring between several examiners is assumed. Furthermore, the assessment of erythema and desquamation constitutes a more subjective criterion than the measurement of the ear thickness.

The macroscopic increase of the ear thickness in the mouse ear model can be attributed, partly, to an increase of the thickness of the epidermis [37,38]. Our study shows a long-lasting hyperplasia of keratinocytes after  $4 \times 30$  Gy. These results can be confirmed by a hind limb skin model which observed an apparent thickening of the murine epithelium after a single dose exposure of 30 Gy and 40 Gy [39]. A second, major contributor to the prompt increase of ear thickness appears to be the accumulation of inflammatory cells upon irradiation as shown in radiation dermatitis studies [37]. The inflammatory phase is the first step of cutaneous wound healing starting within the first three days post-irradiation [20] leading to the continuous increase of ear thickness from day 5 in our study. Immune cells are recruited by pro-inflammatory mediators (e.g., interleukin 17C) expressed by keratinocytes upon X-ray exposure [37]. These mediators may also trigger the hyperproliferation of keratinocytes by an autocrine feedback loop [37] which induces the cellular regeneration of the wound during the second phase of healing [40]. This process is linked to the hyperplasia of keratinocytes. In a pig skin model, healing of the skin is initially associated with a first decrease of basal cell density followed by an increase on day 14–22 after 15 Gy single dose exposure, or even later between days 25–35 after single exposure of 20 Gy [38] which agrees to the beginning of cellular regeneration on day 10–14 in humans [14]. In contrast to that, we observed an increase of the ear thickness between

the days 18–22 (depending on the dose). This observation suggests that cells, which were killed by radiation, were removed by inflammatory cells enabling the replacement of dead keratinocytes by new ones in order to maintain the skin barrier. However, in addition to increased repopulation, increased differentiation may also take place among the regenerated keratinocytes. Regarding the observed increase of ear thickness in our study, the infiltration of immune cells might compensate the decline of basal cell density, as shown in the pig skin model, suggesting that inflammation might be the one of the major contributors to acute radiation-induced ear thickening and a relevant contributor to the chronic ear thickening. Therefore, the ear thickness is a direct measurement of the healing process. Another aspect when comparing our data to the pig skin model would be the applied fractionated schedule. The first fraction destroys some basal keratinocytes followed by further fractions which destroy the remaining keratinocytes [14]. According to this, higher doses lead to an increased cell death and therefore to a reduced basal cell density. This suggests that there is a massive infiltration of immune cells at high doses corresponding to the observed increase of the maximum ear thickness with increasing dose. This proposed mechanism agrees with a study of Morris and Hopewell in 1988 [38] measuring the dependency between the severity of cell depletion, time of maximum depletion and dose. In line to our study, ear swelling, as a sign for cell damage and the healing process, correlates with both an increasing fractional dose and an increasing latency time: The higher the fractional dose, the earlier the ear swelling peaked and the higher is the severity of swelling. After fractional doses of 30 Gy or lower, ear swelling was completely resolved 45 days post-hypofractionation which is in agreement with the findings of a restored basal cell density at day 48 in the pig skin model [38].

## 4. Material and Methods

### 4.1. Ear Irradiation

Female BALB/c mice with an age of 8–12 weeks were obtained from Janvier (Janvier Labs, Saint-Berthevin Cedex, France). Mice were hosted at the experimental sites of the Helmholtz Zentrum München GmbH (Munich, Germany) according to the respective institutional guidelines and the German animal welfare regulations with permission of the local authorities (Regierung von Oberbayern, project license ROB-55.2-2532.Vet\_02-17-9). The animals were kept at 20–24 °C, 45–65% relative humidity, at 12 h light-dark cycle and fed with commercial laboratory animal diet and water ad libitum.

For irradiation, the animals were anaesthetized intraperitoneally with a mixture of 1 mg/mL Medetomidin, 5 mg/mL Midazolam and 0.05 mg/mL Fentanyl. Only the right ear of each mouse was irradiated with a total of four fractions delivered every 24 h. The left ear of each mouse served as an internal control. The dose per fraction was 5 Gy, 10 Gy, 20 Gy and 30 Gy using 70 kVp X-rays at the conventional X-ray cabinet RS225 (XStrahl Limited, Camberley, UK). A 3 mm-thick aluminum filter was used for beam hardening. The irradiation field had a size of 7.2 mm × 7.2 mm. 6–7 mice per dose group were irradiated and compared to sham-irradiated mice, which were treated according to the same protocol but without turning on the X-ray beam. In total, the right ears of 40 mice, including 34 irradiated and 6 unirradiated control animals, were used. Fraction 1 was given on day 0, fraction 2 to 4 on days 1, 2 and 3, respectively (Figure 10). Acute side effects were measured during a follow-up period of 92 days. Late side effects were assessed 92 days after the first fraction.



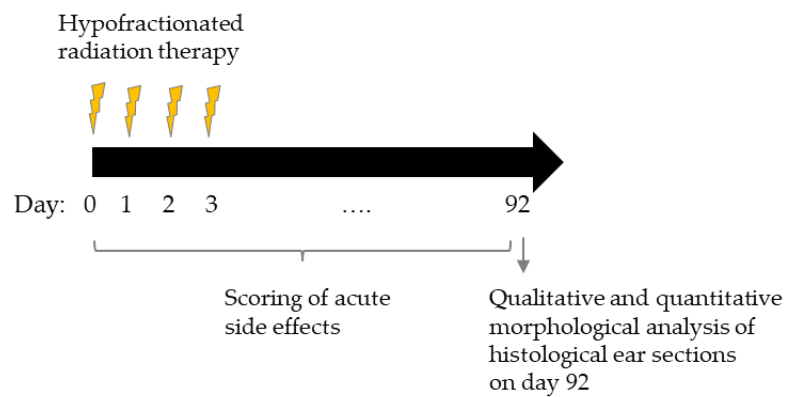


**Figure 10.** Schematic overview of the mouse ear study. Mouse ears were irradiated on 4 consecutive days with doses ranging from 0 Gy, 5 Gy, 10 Gy, 20 Gy to 30 Gy per fraction. Fraction 1 was given on day 0, fraction 2, 3, and 4 was given on day 1, 2 and 3, respectively. Acute side effects were assessed during irradiation and during a follow-up period. On day 92, sections of the mouse ears were assessed for examination of chronic side effects.

#### 4.2. Ear Positioning and Accuracy

For fractionated irradiation, the positioning of the mouse ear was essential. The field of the mouse ear, which was irradiated in fraction one should be reproduced for the following fractions as accurately as possible. For this purpose, a special mouse ear holder was developed (Figure 11) and supplementary software was used.

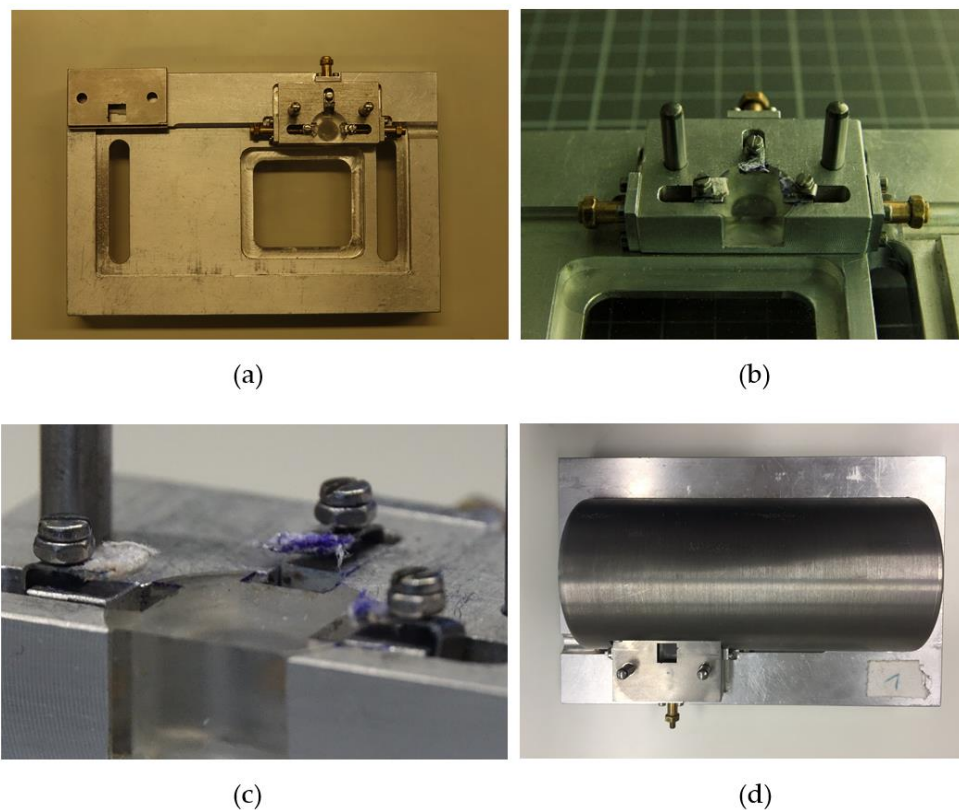


**Figure 11.** (a) Mouse ear holder for irradiation setup. (b–c) Three movable clamps can be seen directly next to the Plexiglas area on the top right corner with their corresponding golden millimeter screws. (d) The entire body of the mouse was shielded by a tungsten shield. Parts of the ear which were not irradiated were also shielded by a tungsten collimator.

The holder of the ear consists of a lying surface with a Plexiglas window to observe the mouse during irradiation. A small stage with an embedded Plexiglas insert is mounted at the location of the head. In Figure 11b, the two big pins are used to fix the tungsten shield, which also defines the irradiation field. Three clamps surround the Plexiglas for ear positioning. The clamps were taped up to spare the ears as much as possible from mechanical stress (Figure 11c). By tightening the screws, the ear could be fixed and by turning the golden millimeter screws the clamps and thus the ear can be moved.

For validation of the correct ear position and thereby of the irradiation field, a picture of the fixed ear was taken daily before the fraction was delivered. To perform the matching a Sony RX10 III camera (Sony, Tokio, Japan) was installed directly above the ear and was connected to the Sony software “imaging edge”. The software allows a live view of the current image, which enables the superposition of the live view with a template with a steplessly adjustable opacity. The template used was the image taken at day of the first fraction, which was meant to be reproduced for the following fractions. This image was superimposed with the current live view for the matching of the fractions 2, 3 and 4. By moving the ear with the millimeter screws the blood vessel structure could be adjusted until it was aligned with the image of fraction one. Using this procedure, an accuracy of around 250  $\mu\text{m}$  was achieved. Figure 12 illustrates the field on the ear, which was irradiated on every day during the hypofractionation schedule.

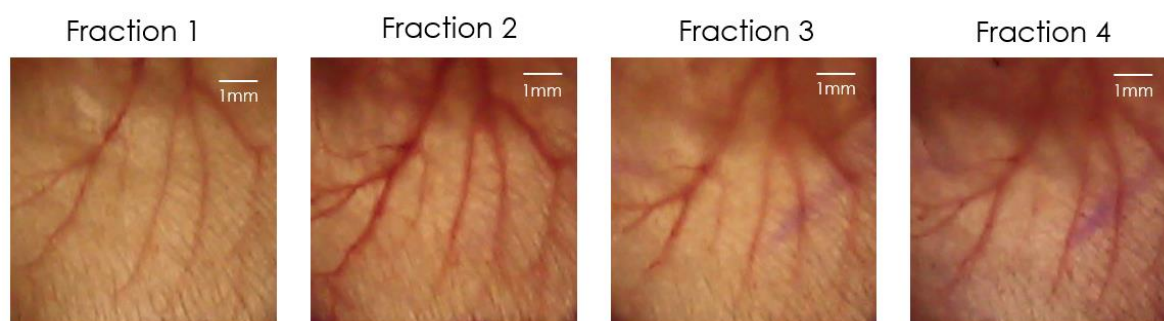


**Figure 12.** Illustration of the irradiation field for every fraction during the 4-fraction course.

#### 4.3. Scoring of Acute Side Effect: Erythema, Desquamation and Ear Swelling

The scoring endpoints were erythema, desquamation and ear thickness. The acute side effects of both the unirradiated left ear and the irradiated right ear were measured over a period of 92 days post-irradiation. All three endpoints were assessed before irradiation (day 0), between the fractions (day 1, 2, 3) and the day after the fourth fraction (day 4) followed by an assessment on every other second day. The scoring frequency was increased once either the ear thickness or acute side effects increased and decreased once the acute reactions decreased. The acute side effects were assessed during a follow-up period of 92 days.

The ear swelling was determined by measuring the ear thickness using a specially adapted electronic external measuring gauge (C1x079; Kröplin GmbH, Schlüchtern, Germany), with measuring contacts of 6 mm in diameter [22]. This caliper allows the measurement of ear thickness within the whole irradiation field without applying pressure to the ear and therefore without squashing of the ear.

Erythema and desquamation were assessed in four grades (Table 3). This system has been used in our laboratory in previous studies [22]. The scoring was always performed by the same two examiners. Scoring of each mouse was carried out blindly in order to limit individual differences in scoring. Both scores were summed up to one acute reaction score [22] for the comparison of radiation-induced side effects after hypofractionated and single dose irradiations (see Section 2.4).

**Table 3.** Semi-quantitative scores for skin erythema (top) and desquamation (bottom).

Kind of Score	Description
Erythema Score	
3	Severe
1.5	Definite
0.5	Mild
0	No
Desquamation Score	
3	Moist
2	Crust
1	Dry
0	No

#### 4.4. Histopathological Analysis of Skin Toxicities on Day 92

After a follow-up period of about 92 days all animals were sacrificed. The excised ears (right) were fixed in 4% (*w/v*) neutrally buffered formaldehyde solution, sectioned and subsequently embedded in paraffin. Transversal ear sections from the center of the irradiation fields with 3  $\mu\text{m}$  thickness were prepared for histological and immunohistochemical analyses. Histological sections were stained with eosin and hematoxylin, or Sirius red for quantification of fibrosis, respectively. For detection of TGF $\beta$ 1, a monoclonal rabbit anti-mouse TGF $\beta$ 1 antibody (abcam EPR21143, Abcam, Cambridge, UK) and an horseradish peroxidase (HRP)-coupled secondary antibody (goat anti rabbit IgG, BA-1000, Biozol Vector, Eching, Germany) were used. Appropriate positive (murine spleen) and negative controls were included in the analysis. Before the analysis and quantification of skin toxicities was performed, a region of interest (ROI) was defined in the center of the irradiated section area, using anatomical landmarks (Figure 13). This ROI had a width of about 3.5 mm and harbored skeletal musculature of the pinna and at least two section profiles of ear veins and/or ear nerves.

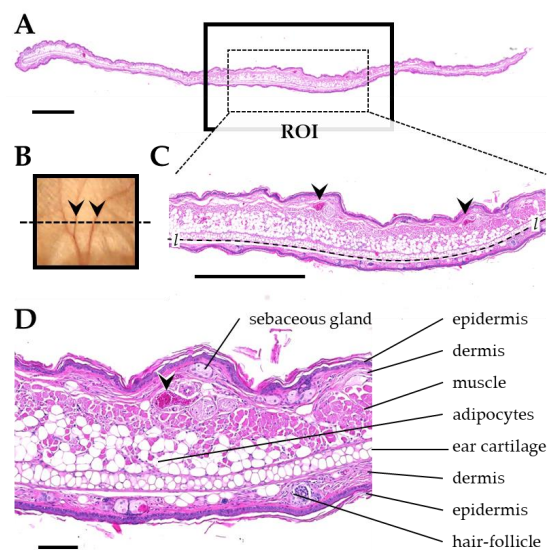


**Figure 13.** Anatomical landmarks used for definition of the ROI in transversal ear sections. (A) Histological section of the pinna. The radiated region of the pinna is indicated by a black box. The dotted line in (B) indicates the orientation of the section through the radiated area of the pinna. (C) ROI sampled for histological analysis and morphometric analysis (dotted rectangle in A). The ROI contains at least two section profiles of ear veins (arrowheads) and skeletal musculature. The dotted line marks the interface of the ear cartilage, used to measure the length *l* of the ROI (i.e., the section width). (D) Detail enlargement of the image shown in C, demonstrating relevant histological structures. Formalin-fixed paraffin embedded sections, H&E staining. Scale bar = 1 mm in A and C, and 100  $\mu\text{m}$  in D.



Inflammation within the section ROI was graded from 0 to 2 using a semi-quantitative grading scheme. Grade 0 shows no relevant infiltration of extravascular neutrophils, no vasodilation or edema. In grade 1, extravascular neutrophils and other mononuclear infiltrating cells appear scattered. Vasodilation and edema are present. Fibrosis may be present. Grade 2 is characterized by a multifocal to diffuse appearance of numerous extravascular neutrophils and other mononuclear infiltrating cells. Additionally, vasodilation and edema are present together with subepidermal fibrosis and epithelial thickening. Ear sections were assigned blindly to one of these three inflammation grades.

The quantification of fibrosis and TGF $\beta$ 1-positive cells was performed by automated digital image analysis (Definiens Architect XD, Definiens Inc., Carlsbad, CA, USA).

#### 4.5. Statistical Analysis

The statistical significance of the differences in the histological parameters measured for different doses per fraction was estimated using the program Graphpad Prism 8 (<https://www.graphpad.com/scientific-software/prism/>). The *p* values were calculated based on the variance analysis (one way-ANOVA test) with Kruskal-Wallis-Test and Dunn's post hoc test. Correlations were performed using the Spearman's correlation with linear regression.

## 5. Conclusions

In conclusion, our findings demonstrate that acute and late radiation-induced side effects of the skin are dose-dependent after a hypofractionated regime. We found that doses up to 20 Gy per fraction caused only reversible effects besides follicle loss while a higher fractional dose of 30 Gy indicates the start of chronic side effects such as fibrosis. Moreover, our results show that ear thickness as a quantitative measurement for ear swelling is able to predict chronic side effects such as fibrosis and inflammation in a mouse ear model. This scoring system can be transferred to other animal models in order to measure acute and late side effects in the ear. Therefore, the results of our in vivo study deliver a numerical scoring criterion of acute side effects after radiation for a better comparison between different treatment modalities like spatially fractionated radiation therapy or high linear energy transfer (LET) particle therapy in future. In future studies, the presence of TGF $\beta$ 1 in the blood should be analyzed in order to better understand the systemic effects on distant organs.

**Author Contributions:** A.C.D., M.S., J.S., T.E.S. and J.R. conceived and designed the animal study. A.C.D. wrote the paper, prepared the final figures and tables and did the editing. J.S. and M.S. developed, designed and implemented the ear positioning and mouse holder. J.S. wrote the Section 4.2. of this manuscript. A.C.D., M.S. and J.S. performed the experiment, supervised all work and did the data acquisition. D.W.M.W., B.S. and T.E.S. performed the experiment. S.B. did the dosimetry at the X-ray cabinet RS225. A.B. and A.F. did the histological sample preparation and analysis, and prepared the final figures. A.B., T.E.S. and G.D. reviewed the manuscript. G.D., T.E.S. and S.E.C. administered the project and did the funding acquisition. All authors read and approved the final manuscript.

**Funding:** This research was funded by the Deutsche Forschungsgemeinschaft via the Cluster of Excellence: Munich-Centre for Advanced Photonics (MAP) [grant number: MAP C.3.4].

**Acknowledgments:** This work has been supported by the Deutsche Forschungsgemeinschaft via Cluster of Excellence: Munich-Centre for Advanced Photonics. We also thank Klaus Rüdiger Trott who contributed with his knowledge to this manuscript and helped in writing.

**Conflicts of Interest:** The authors declare no conflict of interest.

## References

1. Bentzen, S.M. Preventing or reducing late side effects of radiation therapy: Radiobiology meets molecular pathology. *Nat. Rev. Cancer* **2006**, *6*, 702–713. [[CrossRef](#)] [[PubMed](#)]
2. Prasanna, A.; Ahmed, M.M.; Mohiuddin, M.; Coleman, C.N. Exploiting sensitization windows of opportunity in hyper and hypo-fractionated radiation therapy. *J. Thorac. Dis.* **2014**, *6*, 287–302. [[CrossRef](#)]
3. Baskar, R.; Lee, K.A.; Yeo, R.; Yeoh, K.W. Cancer and radiation therapy: Current advances and future directions. *Int. J. Med. Sci.* **2012**, *9*, 193–199. [[CrossRef](#)]

4. Hall, S.; Rudrawar, S.; Zunk, M.; Bernaitis, N.; Arora, D.; McDermott, C.M.; Anoopkumar-Dukie, S. Protection against Radiotherapy-Induced Toxicity. *Antioxidants* **2016**, *5*, 22. [[CrossRef](#)]
5. Hymes, S.R.; Strom, E.A.; Fife, C. Radiation dermatitis: Clinical presentation, pathophysiology, and treatment 2006. *J. Am. Acad. Dermatol.* **2006**, *54*, 28–46. [[CrossRef](#)] [[PubMed](#)]
6. Sprung, C.N.; Forrester, H.B.; Siva, S.; Martin, O.A. Immunological markers that predict radiation toxicity. *Cancer Lett.* **2015**, *368*, 191–197. [[CrossRef](#)]
7. Jacobson, L.K.; Johnson, M.B.; Dedhia, R.D.; Niknam-Bienia, S.; Wong, A.K. Impaired wound healing after radiation therapy: A systematic review of pathogenesis and treatment. *JPRAS* **2017**, *13*, 92–105. [[CrossRef](#)]
8. Martin, M.T.; Vulin, A.; Hendry, J.H. Human epidermal stem cells: Role in adverse skin reactions and carcinogenesis from radiation. *Mutat. Res.* **2016**, *770*, 349–368. [[CrossRef](#)] [[PubMed](#)]
9. Singh, M.; Alavi, A.; Wong, R.; Akita, S. Radiodermatitis: A Review of Our Current Understanding. *Am. J. Clin. Dermatol.* **2016**, *17*, 277–292. [[CrossRef](#)]
10. Joiner, M.; Van der Kogel, A. *Basic Clinical Radiobiology*, 4th ed.; Hodder Education: London, UK, 2009; pp. 1–391, ISBN 978-0340929667.
11. Mendelsohn, F.A.; Divino, C.M.; Reis, E.D.; Kerstein, M.D. Wound Care After Radiation Therapy. *Adv. Skin Wound Care* **2002**, *15*, 216–224. [[CrossRef](#)] [[PubMed](#)]
12. Hegedus, F.; Mathew, L.M.; Schwartz, R.A. Radiation dermatitis: An overview. *Int. J. Dermatol.* **2017**, *56*, 909–914. [[CrossRef](#)]
13. Sivan, V.; Vozenin-Brotans, M.-C.; Tricaud, Y.; Lefaix, J.-L.; Cosset, J.-M.; Dubray, B.; Martin, M.T. Altered proliferation and differentiation of human epidermis in cases of skin fibrosis after radiotherapy. *Int. J. Radiat. Oncol. Biol. Phys.* **2002**, *53*, 385–393. [[CrossRef](#)]
14. Ryan, J.L. Ionizing radiation: The good, the bad, and the ugly. *J. Investig. Dermatol.* **2012**, *132*, 985–993. [[CrossRef](#)]
15. Straub, J.M.; New, J.; Hamilton, C.D.; Lominska, C.; Shnyder, Y.; Thomas, S.M. Radiation-induced fibrosis: Mechanisms and implications for therapy. *J. Cancer Res. Clin. Oncol.* **2015**, *141*, 1985–1994. [[CrossRef](#)]
16. Okunieff, P.; Xu, J.; Hu, D.; Liu, W.; Zhang, L.; Morrow, G.; Pentland, A.; Ryan, J.L.; Ding, I. Curcumin protects against radiation-induced acute and chronic cutaneous toxicity in mice and decreases mRNA expression of inflammatory and fibrogenic cytokines. *Int. J. Radiat. Oncol. Biol. Phys.* **2006**, *65*, 890–898. [[CrossRef](#)]
17. Mancini, M.; Sonis, S. Mechanisms of cellular fibrosis associated with cancer regimen-related toxicities. *Front. Pharmacol.* **2014**, *5*. [[CrossRef](#)] [[PubMed](#)]
18. Wynn, T.A. Integrating mechanisms of pulmonary fibrosis. *J. Exp. Med.* **2011**, *208*, 1339–1350. [[CrossRef](#)] [[PubMed](#)]
19. Ventura, J.; Lobachevsky, P.N.; Palazzolo, J.S.; Forrester, H.; Haynes, N.M.; Ivashkevich, A.; Stevenson, A.W.; Hall, C.J.; Ntargaras, A.; Kotsaris, V.; et al. Localized Synchrotron Irradiation of Mouse Skin Induces Persistent Systemic Genotoxic and Immune Responses. *Cancer Res.* **2017**, *77*, 6389–6399. [[CrossRef](#)]
20. Gieringer, M.; Gosepath, J.; Naim, R. Radiotherapy and wound healing: Principles, management and prospects (review). *Oncol. Rep.* **2011**, *26*, 299–307. [[CrossRef](#)]
21. Cox, J.D.; Stetz, J.; Pajak, T.F. Toxicity criteria of the Radiation Therapy Oncology Group (RTOG) and the European organization for research and treatment of cancer (EORTC). *Int. J. Radiat. Oncol. Biol. Phys.* **1995**, *31*, 1341–1346. [[CrossRef](#)]
22. Girst, S.; Greubel, C.; Reindl, J.; Siebenwirth, C.; Zlobinskaya, O.; Walsh, D.W.; Illicic, K.; Aichler, M.; Walch, A.; Wilkens, J.J.; et al. Proton Minibeam Radiation Therapy Reduces Side Effects in an In Vivo Mouse Ear Model. *Int. J. Radiat. Oncol. Biol. Phys.* **2016**, *95*, 234–241. [[CrossRef](#)]
23. Law, M.P.; Ahier, R.G.; Field, S.B. The Response of Mouse Skin to Combined Hyperthermia and X-rays. *Int. J. Radiat. Biol. Relat. Stud. Phys. Chem. Med.* **1977**, *32*, 153–163. [[CrossRef](#)] [[PubMed](#)]
24. Coggle, J.E.; Lambert, B.E.; Moores, S.R. Radiation effects in the lung. *Environ. Health Perspect.* **1986**, *70*, 261–291. [[CrossRef](#)]
25. Anscher, M.S.; Kong, F.-M.; Jirtle, R.L. The relevance of transforming growth factor  $\beta$ 1 in pulmonary injury after radiation therapy. *Lung Cancer* **1998**, *19*, 109–120. [[CrossRef](#)]
26. Peach, M.S.; Showalter, T.N.; Ohri, N. Systematic Review of the Relationship between Acute and Late Gastrointestinal Toxicity after Radiotherapy for Prostate Cancer. *Prostate Cancer* **2015**, *2015*, 624736. [[CrossRef](#)]
27. Dörr, W.; Hendry, J.H. Consequential late effects in normal tissues. *Radiother. Oncol.* **2001**, *61*, 223–231. [[CrossRef](#)]

28. Collen, E.B.; Mayer, M.N. Acute effects of radiation treatment: Skin reactions. *Can. Vet. J.* **2006**, *47*, 931–935. [[PubMed](#)]
29. Horton, J.A.; Chung, E.J.; Hudak, K.E.; Sowers, A.; Thetford, A.; White, A.O.; Mitchell, J.B.; Citrin, D.E. Inhibition of radiation-induced skin fibrosis with imatinib. *Int. J. Radiat. Biol.* **2013**, *89*, 162–170. [[CrossRef](#)]
30. Panizzon, R.G.; Hanson, W.R.; Schwartz, D.E.; Malkinson, F.D. Ionizing Radiation Induces Early, Sustained Increases in Collagen Biosynthesis: A 48-Week Study in Mouse Skin and Skin Fibroblast Cultures. *Radiat. Res.* **1988**, *116*, 145–156. [[CrossRef](#)] [[PubMed](#)]
31. Law, M.P. Vascular permeability and late radiation fibrosis in mouse lung. *Radiat. Res.* **1985**, *103*, 60–76. [[CrossRef](#)]
32. Randall, K.; Coggle, J.E. Long-term expression of transforming growth factor TGF beta1 in mouse skin after localized beta-irradiation. *Int. J. Radiat. Biol.* **1996**, *70*, 351–360. [[CrossRef](#)] [[PubMed](#)]
33. Formenti, S.C.; Demaria, S. Systemic effects of local radiotherapy. *Lancet Oncol.* **2009**, *10*, 718–726. [[CrossRef](#)]
34. Williams, J.P.; Brown, S.L.; Georges, G.E.; Hauer-Jensen, M.; Hill, R.P.; Huser, A.K.; Kirsch, D.G.; Macvittie, T.J.; Mason, K.A.; Medhora, M.M.; et al. Animal models for medical countermeasures to radiation exposure. *Radiat. Res.* **2010**, *173*, 557–578. [[CrossRef](#)] [[PubMed](#)]
35. Chaze, T.; Hornez, L.; Chambon, C.; Haddad, I.; Vinh, J.; Peyrat, J.P.; Benderitter, M.; Guipaud, O. Serum Proteome Analysis for Profiling Predictive Protein Markers Associated with the Severity of Skin Lesions Induced by Ionizing Radiation. *Proteomes* **2013**, *1*, 40–69. [[CrossRef](#)] [[PubMed](#)]
36. Coggle, J.E. Expression of Transforming Growth Factor- $\beta$ 1 in Mouse Skin During the Acute Phase of Radiation Damage. *Int. J. Radiat. Biol.* **1995**, *68*, 301–309. [[CrossRef](#)]
37. Liao, W.; Hei, T.K.; Cheng, S.K. Radiation-Induced Dermatitis is Mediated by IL17-Expressing gammadelta T Cells. *Radiat. Res.* **2017**, *187*, 454–464. [[CrossRef](#)]
38. Morris, G.M.; Hopewell, J.W. Changes in the cell kinetics of pig epidermis after single doses of X rays. *Br. J. Radiol.* **1988**, *61*, 205–211. [[CrossRef](#)]
39. Jang, W.H.; Shim, S.; Wang, T.; Yoon, Y.; Jang, W.-S.; Myung, J.K.; Park, S.; Kim, K.H. In vivo characterization of early-stage radiation skin injury in a mouse model by two-photon microscopy. *Sci. Rep.* **2016**, *6*, 19216. [[CrossRef](#)]
40. Yamaguchi, Y.; Yoshikawa, K. Cutaneous Wound Healing: An Update. *J. Dermatol.* **2001**, *28*, 521–534. [[CrossRef](#)]



© 2019 by the authors. Licensee MDPI, Basel, Switzerland. This article is an open access article distributed under the terms and conditions of the Creative Commons Attribution (CC BY) license (<http://creativecommons.org/licenses/by/4.0/>).

### 3.2.3 Normal tissue response depends on combined temporal and spatial fractionation of proton minibeam

#### 3.2.3.1 Summary of the study

The ear thickness as an acute toxicity and the amount of fibrous connective tissue as late toxicity were monitored for 150 days after sham irradiation and hypofractionated pMBRT with three different fractionation schemes (FS). Proton minibeam with a size of 222  $\mu\text{m}$  were administered. In FS1, a pattern of 16 minibeam with a ctc distance of 1.8 mm was delivered on the same position on the ear in every fraction (accurate irradiation, high dose modulation). In FS2, this pattern was shifted in each fraction by the half ctc distance of FS1 (inaccurate irradiation high dose modulation). In FS3, 64 minibeam with the half ctc distance of 0.9 mm and only a one-quarter dose of a minibeam of FS1 or FS2 were delivered to the same position in each fraction (accurate irradiation, low dose modulation). FS3 led to the same integral dose pattern after all fractions as FS2.

A fractional dose of 30 Gy was chosen from the X-ray pilot study (chapter 3.2.2). This dose induced a measurable normal tissue response allowing the visibility of reduced normal tissue toxicity when the sparing effect of different fractionation schemes of pMBRT was compared. The X-ray dose corresponds almost equally to the proton dose due to an RBE of around 1.1 [27].

In this study, pMBRT with an integral dose of 30 Gy spares the most the healthy skin of the mouse ear and does not induce fibrotic tissue when it is delivered to the same position in each fraction (FS1). A shift of the minibeam pattern (FS2) induces a stronger ear swelling as well as a slight increase of the absolute area of fibrotic tissue. A significant increase in both ear swelling and collagen deposition is measured after FS3.

In conclusion, both acute and late normal tissue complications depend on both the accuracy of the reirradiation position and the dose modulation of proton minibeam. By using a high reirradiation accuracy and high dose modulation, ear swelling and the amount of fibrotic tissue were almost on the same level as sham-irradiated mice. A lack of accuracy slightly increased the normal tissue complications when a highly dose modulated minibeam pattern is applied. However, this sparing effect still better than that of an accurately delivered pattern with a low dose modulation.

### 3.2.3.2 Contributions

I planned and prepared the experiment in collaboration with Matthias Sammer. Jannis Schauer and Matthias Sammer developed the mouse holder and implemented the positioning of the ear in each fraction at the beamline of the ion microprobe SNAKE. I was responsible for the biological part of this experiment while Matthias Sammer had the responsibility for the physical aspects.

I conducted the irradiation of the ears with the support of Matthias Sammer, Jannis Schauer, Dr. Judith Reindl, Sarah Rudigkeit and Nicole Matejka (irradiation) and Sandra Bicher, Marlon Stein, Benjamin Schwarz, Dr. Stefan Bartzsch (fixation, anesthesia). I conducted the scoring of ear swelling with the help of Matthias Sammer, Jessica Weigel, Sandra Bicher and Kateryna Oleksenko during the follow-up period of 150 days. I planned and organized the histological analysis of the ear samples. The histological samples were prepared and stained by the Research Unit Analytical Pathology at the Helmholtz Center Munich (Dr. Andreas Blutke, Dr. Annette Feuchtinger). I performed data analysis and interpretation. In addition, I wrote the manuscript and designed figure 3. Matthias Sammer designed figures 1 and 2. All co-authors, but especially Matthias Sammer, Prof. Dr. Thomas E. Schmid and Prof. Dr. Günther Dollinger contributed to the scientific discussion, data interpretation, and reviewed the manuscript.

### 3.2.3.3 Publication

The data were presented in the following original peer-reviewed Scientific Letter. It was submitted on January 15<sup>th</sup> in 2020 in the 'International Journal of Radiation Oncology, Biology and Physics'.

#### ***Normal tissue response depends on combined temporal and spatial fractionation of proton minibeam***

Annique C. Dombrowsky \*, Matthias Sammer \*, Jannis Schauer, Kateryna Oleksenko, Sandra Bicher, Benjamin Schwarz, Sarah Rudigkeit, Nicole Matejka, Judith Reindl, Stefan Bartzsch, Andreas Blutke, Annette Feuchtinger, Stephanie E. Combs, Thomas E. Schmid, Günther Dollinger

\* contributed equally to this manuscript

*Submitted*

Note: In the submitted manuscript the reference XXX is a place holder for my publication listed in chapter 3.2.2.

# Normal tissue response depends on combined temporal and spatial fractionation of proton minibeam

## *Short running title: temporally fractionated proton minibeam*

Annique C. Dombrowsky, M.Sc. <sup>\*,1,2</sup>, Matthias Sammer, M.Sc. <sup>\*,3</sup>, Jannis Schauer, M.Sc. <sup>3</sup>,  
Kateryna Oleksenko, B.Sc. <sup>1</sup>, Sandra Bicher, M.Sc. <sup>1,2</sup>, Benjamin Schwarz, M.Sc. <sup>3</sup>,  
Sarah Rudigkeit, M.Sc. <sup>3</sup>, Nicole Matejka, M.Sc. <sup>3</sup>, Judith Reindl, Juniorprof. <sup>3</sup>,  
Stefan Bartzsch, Ph.D. <sup>1,2</sup>, Andreas Blutke, Ph.D. <sup>4</sup>, Annette Feuchtinger, Ph.D. <sup>4</sup>,  
Stephanie E. Combs, Prof. <sup>1,2</sup>, Thomas E. Schmid, Prof. <sup>1,2</sup>, Günther Dollinger, Prof. <sup>3</sup>

\* Both authors contributed equally to this manuscript

<sup>1</sup> Institute of Radiation Medicine, Helmholtz Zentrum München GmbH, 85764 Neuherberg, Germany

<sup>2</sup> Department of Radiation Oncology, Technical University of Munich, School of Medicine, Klinikum rechts der Isar, 81675 München, Germany

<sup>3</sup> Institute for Applied Physics and Metrology, Universität der Bundeswehr München, 85577 Neubiberg, Germany

<sup>4</sup> Research Unit Analytical Pathology, Helmholtz Zentrum München GmbH, 85764 Neuherberg, Germany

**Corresponding author:** Annique C. Dombrowsky, +4989318743041,  
annique.dombrowsky@helmholtz-muenchen.de

**Conflicts of interest:** The authors declare no conflict of interest.

**Funding:** The project was funded by the BMBF project “LET-Verbund” (02NUK031A) and the Deutsche Forschungsgesellschaft Cluster of Excellence: Munich-Centre for Advanced Photonics [MAP C.3.4].

**Data sharing statement:** All data generated and analyzed during this study are included in this published article (and its supplementary information files).

**Statistical analysis:** Annique C. Dombrowsky, +4989318743041,  
annique.dombrowsky@helmholtz-muenchen.de

# Normal tissue response depends on combined temporal and spatial fractionation of proton minibeam

*Short running title: temporally fractionated proton minibeam*

## Abstract

Purpose: Proton minibeam radiotherapy, a spatial fractionation concept, widens the therapeutic window. By reducing normal tissue toxicities, it allows the utilization of higher doses in a hypofractionated regime. Combining temporal fractions with spatial fractionation raises questions of reirradiation accuracies due to the beam pattern.

Methods and Material: Healthy mouse ear pinnae were irradiated with four fractions of 30Gy mean dose, respectively, applying Gaussian proton pencil minibeam of  $\sigma=222\ \mu\text{m}$  in three different schemes. Both acute (swelling) and late skin toxicities (fibrous connective tissue) were evaluated for 153 days after the first fraction.

Results: A pattern of 16 minibeam with a center-to-center distance (ctc) of 1.8mm was delivered to the same position in every fraction and induced the lowest ear swelling and amount of fibrous tissue, while a pattern shift by  $\text{ctc}/2$  between the fractions led to a significant stronger swelling and a slight increase of fibrous tissue. The highest increase of ear thickness and fibrotic tissue was measured when 4x64 minibeam with a ctc of 0.9mm were irradiated.

Conclusion: The highest normal tissue-sparing is achieved after a highly accurate positioning of minibeam. However, even if a precise reirradiation cannot be achieved, the normal tissue toxicities can still be reduced.

## Introduction

Proton minibeam radiotherapy (pMBRT), a spatially fractionated modality in radiotherapy, uses submillimeter proton beam with a center-to-center distance (ctc) of a few millimeters



1 to widen the therapeutic window by modulating the treatment dose [1,2]. Spatial fractionation  
2 bases on the dose-volume effect which states that the tissue tolerance increases when a  
3 mean dose is redistributed into smaller fields [3]. Due to a small-angle scattering of protons  
4 within the tissue, beams widen with depth enabling uniform tumor irradiation for a  
5 unidirectional irradiation mode [2,4]. Irradiation modalities, especially the ctc, mainly depend  
6 on the tumor location and its size [5]. Preclinical experiments *in vitro* [2,6] and *in vivo* [4,7,8]  
7 have already shown the normal tissue-sparing of pMBRT in comparison to open field  
8 irradiation. A single dose of pMBRT showed superior survival and shrank the tumor more  
9 than standard treatment [1,9]. Due to the extraordinary normal tissue-sparing as well as the  
10 potential advantages in tumor control, pMBRT allows hypofractionation with high doses.

11 We hypothesized that the combined tissue-sparing effect of temporal and spatial  
12 fractionation of proton beams is superior to conventional treatments. Therefore, we  
13 questioned if the reirradiation accuracy of proton minibeam (pMB) influences skin toxicity.

## 14 **Methods and Material**

15 Four fractions of 20MeV pencil proton minibeam (4xpMBRT) with a size of  $\sigma=222\pm5\mu\text{m}$   
16 were delivered daily to the right healthy pinna of Balb/c mice. The left ear served as a  
17 control. A mean fractional dose of  $30\pm3.6\text{Gy}$  was applied to induce a strong acute toxicity as  
18 shown in the X-ray pilot study using the same mouse model [10]. Three fractionation  
19 schemes (FS) were tested (Fig.1) and compared to sham-irradiation, using 6-8 mice per  
20 group. Fractions of 16 pMBs at a ctc of 1.8mm were applied and accurately reirradiated in  
21 each fraction (FS1). The same pattern was used for FS2 but shifted by ctc/2 in each fraction,  
22 hence avoiding to hit the previously irradiated beam pattern. As the third scheme (FS3), four  
23 fractions of 64 pMBs were applied with a ctc of 0.9mm. The integral dose pattern of both  
24 FS2 and FS3 coincided after all fractions. Ears were positioned in each fraction according to  
25 the characteristic blood vessel structure achieving an average reposition accuracy of  
26  $110\pm52\mu\text{m}$ . Ear thickness (swelling, acute toxicity) was measured [4,8,10,11] for 153 days

1 after fraction one. On day 153, fibrous connective tissue (FCT) in the dermis of the pinnae  
2 (late toxicity) was stained with Sirius red [10] in three to four equidistant, parallel ear sections  
3 for quantification of the absolute area per ear section (volume fraction). According to the  
4 Delesse principle, the volume fraction can be estimated by the ratio of the area of a  
5 component relative to the entire profile area [12,13].  
6  
7  
8  
9

## 10 11 **Results**

12  
13  
14 The results show that ear thickening depends on the applied dose pattern (Fig.2). FS3 ears  
15 thickened significantly stronger with  $783.7 \pm 50.1 \mu\text{m}$  on day 18 than FS1 ears, which peaked  
16 on day 12 with  $401.1 \pm 14.8 \mu\text{m}$  ( $p < 0.0001$ ), and FS2 ears, which peaked on day 18 with  
17  $558.1 \pm 53.8 \mu\text{m}$  ( $p < 0.05$ ). For the final third of the follow-up ( $t > 100\text{d}$ ), in which a constant ear  
18 thickness was found in each group, the mean thickness of FS1 ears ( $277.55 \pm 2.17 \mu\text{m}$ )  
19 resembled sham ears ( $266.1 \pm 2.4 \mu\text{m}$ ,  $p > 0.05$ ). The final thickness was significantly increased  
20 after FS2 ( $349.1 \pm 14.3 \mu\text{m}$ ,  $p < 0.0001$ ) and FS3 ( $431.5 \pm 18.0 \mu\text{m}$ ,  $p < 0.0001$ ) compared to FS1  
21 indicating long-term toxicities. The absolute area of FCT does not differ between FS1, sham  
22 and control ears. Thus, FS1 does not show any increase of the FCT area. There was a  
23 significant increase of the FCT area after FS3 compared to sham-irradiated animals  
24 ( $p < 0.0001$ , Fig.3). FCT was less pronounced in FS2 than in FS3.  
25  
26  
27  
28  
29  
30  
31  
32  
33  
34  
35  
36  
37  
38  
39

## 40 **Discussion**

41  
42  
43 These results demonstrate that the normal tissue response depends largely on the temporal  
44 and spatial dose distribution. The most benefits were found for FS1 aiming for the irradiation  
45 of the same pattern in each fraction. It keeps the damage within a small area over the  
46 complete treatment time. Despite the integrated mean dose of 120Gy, the inter-beam cells  
47 received only a neglectable dose, enabling an efficient tissue repair of severely hit cells. The  
48 efficient tissue cell repair might have a similar base as the hypothesis of Dilmanian about the  
49 progenitor glial cells in the brain: damaged cells were repaired between the fractions by  
50 proliferation and migration of intact inter-beam cells [14]. The sublethal damage of inter-  
51  
52  
53  
54  
55  
56  
57  
58  
59  
60  
61  
62  
63  
64  
65

1 beam cells can be repaired within 6h [15] enabling the replacement of severely hit in-beam  
2 cells within 24h until the next fraction is delivered. This is especially true for fast proliferating  
3 tissues such as the skin [16]. The total repair of in-beam cells takes a longer recovery time  
4 indicated by the maximum ear swelling 6 days later for FS2 than FS1, suggesting that the  
5 pattern shift in FS2 hampers the repair of the following fractions.  
6  
7  
8  
9

10  
11 FS2 and FS3 resulted in the same temporal integrated dose distribution with a valley dose of  
12 20.8Gy. However, the normal tissue responses differed significantly indicating that the  
13 spatial dose distribution per fraction is critical for the severity of skin toxicities. The  
14 neglectable valley dose in FS2 kept tissue more spared in each fraction than the valley dose  
15 of 5.2Gy per fraction in FS3. In FS3, all cells within the irradiation field received a harmful  
16 dose due to its high valley dose impeding the recovery of damaged cells by migration and  
17 proliferation of inter-beam cells due to their damage.  
18  
19  
20  
21  
22  
23  
24  
25  
26

27  
28 Our results show also a marked thickness increase of FS3 ears on day 153 while FS2 ears  
29 swelled intermediate, and FS1 ears even returned to the same thickness as measured within  
30 the sham group. The extent of FCT in FS2 and FS3 ears significantly contributed to the  
31 increase of the measured ear thickness, as already measured in the X-ray pilot study [10],  
32 while there is no difference in the extent of FCT between sham and FS1. The relation  
33 between ear thickness and absolute area of FCT agrees to previous findings with X-ray  
34 broadbeam irradiation [10].  
35  
36  
37  
38  
39  
40  
41  
42  
43

## 44 **Conclusion**

45  
46  
47 In conclusion, our study demonstrated for the first time the impact of irradiation accuracies  
48 and dose modulation on radiation toxicities in the normal tissue for a combination of  
49 temporal and spatial fractionation. Acute and late side effects were maximally reduced by an  
50 accurate reirradiation of the pattern. Low valley doses per fraction reduce skin toxicities  
51 compared to higher valley doses even though the dose distribution in both coincided after all  
52 fractions.  
53  
54  
55  
56  
57  
58  
59  
60  
61  
62  
63  
64  
65

## References

1. Prezado, Y.; Jouvion, G.; Patriarca, A.; Nauraye, C.; Guardiola, C.; Juchaux, M.; Lamirault, C.; Labiod, D.; Jourdain, L.; Sebric, C., *et al.* Proton minibeam radiation therapy widens the therapeutic index for high-grade gliomas. *Scientific Reports* **2018**, *8*, 16479, doi:10.1038/s41598-018-34796-8.
2. Zlobinskaya, O.; Girst, S.; Greubel, C.; Hable, V.; Siebenwirth, C.; Walsh, D.W.; Multhoff, G.; Wilkens, J.J.; Schmid, T.E.; Dollinger, G. Reduced side effects by proton microchannel radiotherapy: study in a human skin model. *Radiat Environ Biophys* **2013**, *52*, 123-133, doi:10.1007/s00411-012-0450-9.
3. Withers, H.R.; Taylor, J.M.; Maciejewski, B. Treatment volume and tissue tolerance. *Int J Radiat Oncol Biol Phys* **1988**, *14*, 751-759, doi:10.1016/0360-3016(88)90098-3.
4. Girst, S.; Greubel, C.; Reindl, J.; Siebenwirth, C.; Zlobinskaya, O.; Walsh, D.W.; Illicic, K.; Aichler, M.; Walch, A.; Wilkens, J.J., *et al.* Proton Minibeam Radiation Therapy Reduces Side Effects in an In Vivo Mouse Ear Model. *Int J Radiat Oncol Biol Phys* **2015**, *95*, 234-241, doi:10.1016/j.ijrobp.2015.10.020.
5. Sammer, M.; Greubel, C.; Girst, S.; Dollinger, G. Optimization of beam arrangements in proton minibeam radiotherapy by cell survival simulations. *Med Phys* **2017**, *44*, 6096-6104, doi:10.1002/mp.12566.
6. Girst, S.; Marx, C.; Brauer-Krisch, E.; Bravin, A.; Bartzsch, S.; Oelfke, U.; Greubel, C.; Reindl, J.; Siebenwirth, C.; Zlobinskaya, O., *et al.* Improved normal tissue protection by proton and X-ray microchannels compared to homogeneous field irradiation. *Phys Med* **2015**, *31*, 615-620, doi:10.1016/j.ejmp.2015.04.004.
7. Prezado, Y.; Jouvion, G.; Hardy, D.; Patriarca, A.; Nauraye, C.; Bergs, J.; Gonzalez, W.; Guardiola, C.; Juchaux, M.; Labiod, D., *et al.* Proton minibeam radiation therapy spares normal rat brain: Long-Term Clinical, Radiological and Histopathological Analysis. *Sci Rep* **2017**, *7*, 14403, doi:10.1038/s41598-017-14786-y.
8. Sammer, M.; Zahnbrecher, E.; Dobiasch, S.; Girst, S.; Greubel, C.; Illicic, K.; Reindl, J.; Schwarz, B.; Siebenwirth, C.; Walsh, D.W.M., *et al.* Proton pencil minibeam irradiation of an

1  
2 in-vivo mouse ear model spares healthy tissue dependent on beam size. *PloS one* **2019**, *14*,  
3 e0224873, doi:10.1371/journal.pone.0224873.

- 4 9. Prezado, Y.; Jouvion, G.; Guardiola, C.; Gonzalez, W.; Juchaux, M.; Bergs, J.; Nauraye, C.;  
5 Labiod, D.; De Marzi, L.; Pouzoulet, F., *et al.* Tumor Control in RG2 Glioma-Bearing Rats: A  
6 Comparison Between Proton Minibeam Therapy and Standard Proton Therapy. *Int J Radiat*  
7 *Oncol Biol Phys* **2019**, *104*, 266-271, doi:10.1016/j.ijrobp.2019.01.080.  
8  
9  
10  
11  
12 10. XXXX.  
13  
14 11. Sammer, M.; Teiluf, K.; Girst, S.; Greubel, C.; Reindl, J.; Ilicic, K.; Walsh, D.W.M.; Aichler, M.;  
15 Walch, A.; Combs, S.E., *et al.* Beam size limit for pencil minibeam radiotherapy determined  
16 from side effects in an in-vivo mouse ear model. *PloS one* **2019**, *14*, e0221454-e0221454,  
17 doi:10.1371/journal.pone.0221454.  
18  
19  
20  
21  
22 12. Delesse, M.A. Procède mecanique pour determiner la composition des roches. *C. R. Acad.*  
23 *Sci. (Paris)* **1847**, *25*, 544.  
24  
25  
26  
27 13. Howard, C.V.; Reed, M.G. *Three-dimensional measurement in microscopy* 2nd ed.; BIOS  
28 Scientific Publishers: Abingdon, 2004; doi: 10.4324/9780203006399  
29  
30  
31 14. Dilmanian, F.A.; Qu, Y.; Feinendegen, L.E.; Peña, L.A.; Bacarian, T.; Henn, F.A.; Kalef-Ezra,  
32 J.; Liu, S.; Zhong, Z.; McDonald, J.W. Tissue-sparing effect of x-ray microplanar beams  
33 particularly in the CNS: Is a bystander effect involved? *Experimental Hematology* **2007**, *35*,  
34 69-77, doi:10.1016/j.exphem.2007.01.014.  
35  
36  
37  
38  
39 15. Connell, P.P.; Hellman, S. Advances in Radiotherapy and Implications for the Next Century: A  
40 Historical Perspective. *Cancer Research* **2009**, *69*, 383-392, doi:10.1158/0008-5472.Can-07-  
41 6871.  
42  
43  
44  
45 16. Hall, E.J. *Radiobiology for the Radiobiologist* 5 ed.; Lippincott Williams & Wilkins: 0-7817-  
46 2649-2.  
47  
48  
49  
50  
51  
52  
53  
54  
55  
56  
57  
58  
59  
60  
61  
62  
63  
64  
65

## Figure Captions

**Figure 1: Illustration of the three fractionation schemes (FS) for 4xpMBRT.** One fraction of 16 MB was delivered daily on either the same position on the ear (FS1) or shifted by the half distance between two MBs (FS2). FS3 administered 64 MB with a one-quarter MB dose in FS1 or FS2. In every fraction of FS3, the same MB positions were irradiated to result in the same integral dose distribution as FS2.

**Figure 2: Thickness of irradiated mouse ears** for sham irradiation (green), and three different fractionation schemes (FS) of 4xpMBRT (FS1 - red, FS2 – blue, FS3 – yellow). Day zero was taken as the first day of irradiation. Mean±standard error of the mean is depicted.

**Figure 3: Dermal extent of fibrous connective tissue (FCT)** 153 days after fraction one of 4xpMBRT. **(A) Representative histology of the pinnae** after Sirius red staining. Compared to control (ctrl), sham, and FS1 mice, both FS2 and FS3 ears display markedly increased fibrotic tissue in dermis (asterisks). Paraffin sections, bars=100 µm. **(B) Quantification of absolute area of FCT per section length** is obtained from the product of FCT area ratio ( $A_{A(F/E)}$ ) and ear thickness. Given are the means±standard deviations per group. Significance was determined by means of the t-test, \*p<0.05, \*\*p<0.01, \*\*\*\*p<0.0001.

Figure 1

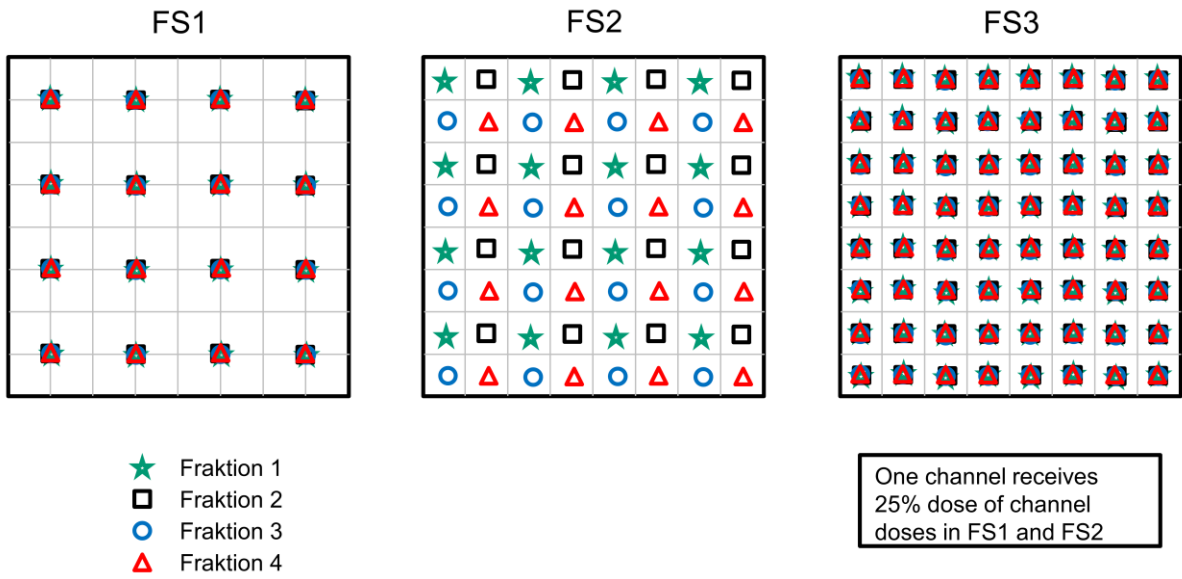
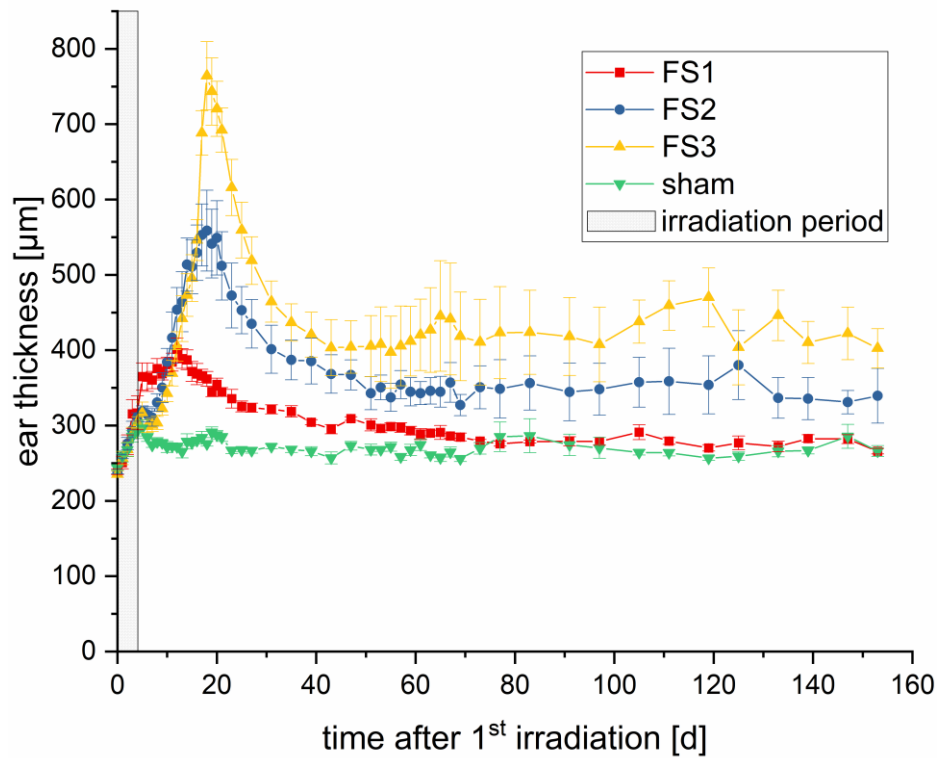


Figure 2



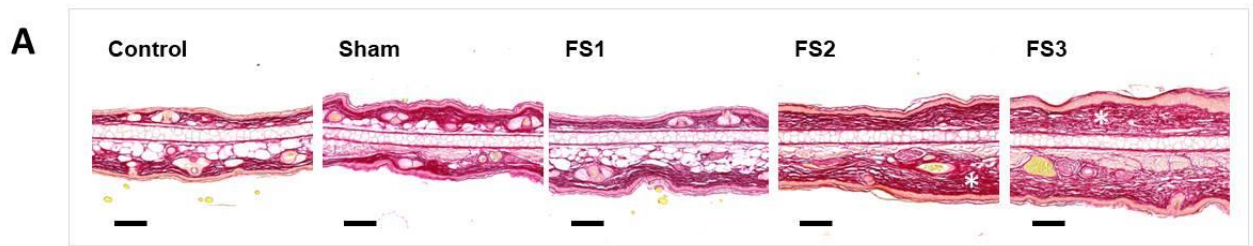


Figure 3A

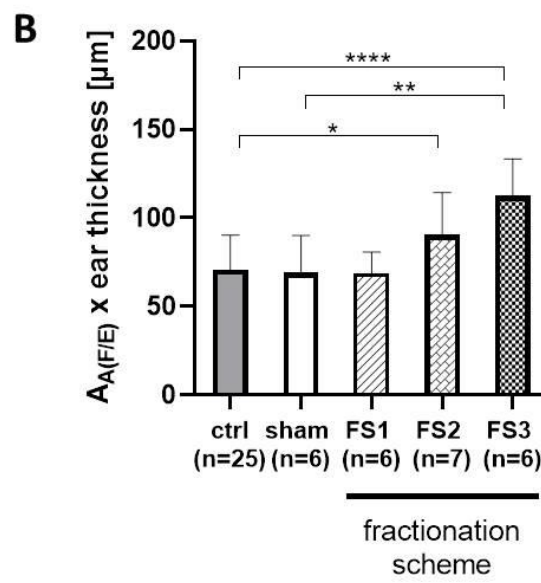


Figure 3B



## 4 Discussion and Conclusion

### 4.1 The Munich Compact Light Source as a new compact X-ray source for MRT

In the past, the radiobiological effect of MRT was mainly studied at large synchrotrons radiation facilities. In order to overcome the spatial limitations [95], costs [95,106] and access restrictions [114] of synchrotrons, compact X-ray sources have recently been developed. However, there are still technical constraints present at these compact X-ray sources, especially regarding dose rate, X-ray energy, and PVDR.

So far, dose rates of compact X-ray sources are far smaller than those of synchrotrons which usually have extremely high dose rates of up to several thousands of Gray per second [55]. At the MuCLS, a mean dose rate of 0.6 Gy/min (0.01 Gy/s) was achieved for microbeam irradiations in the here presented *in vivo* study (chapter 3.1), but also in *in vitro* experiments of Burger *et al.*, (2017) [112]. Despite this dose rate is much lower compared to synchrotrons, it is in the range of dose rates of other compact X-ray sources. As an example, the ThomX machine which is also an ICS is operated at 0.5 Gy/s [109]. Furthermore, a compact microbeam source based on a conventional X-ray tube with a specially designed collimator is able to achieve a similar dose rate of 0.3 Gy/s [110]. Other more powerful compact X-ray sources have also been suggested such as the LFXT which demonstrates a dose rate of 180 Gy/s [95]. However, this is still far smaller than the ultra-high dose rate of synchrotrons. Despite a high dose rate is recommended in order to avoid microbeam blurring due to cardiosynchronous motion [55], the only compact X-ray source used for *in vivo* MRT experiments so far is the CNT X-ray source showing anti-tumor effectiveness at an average dose rate of 1.4 Gy/min (0.023 Gy/s) [53,104,114]. The dose rate of the CNT X-ray source is quite comparable to that of the MuCLS. However, both sources have a lower dose rate than other compact X-ray sources. Nevertheless, the low dose rate of 0.6 Gy/min at the MuCLS was able to inhibit tumor growth inhibition after MRT in this doctoral thesis.

In contrast to the dose rate, the X-ray energy produced at compact X-ray sources is in the same range or only slightly below the used mean energy at synchrotrons [110]. A median beam energy between 70 keV and 120 keV was measured at the NSLS [69] and 100 keV at the ESRF [91]. The CNT X-ray source produces 60 keV X-rays [104], while the ThomX machine generates X-ray energy between 20 keV and 90 keV [109]. Furthermore, simulations at the LFXT showed X-ray energies starting from 20 keV which, however, can rise up to 600 keV [95]. In contrast to other compact X-ray sources, the MuCLS produces only low-energetic X-rays of 15-35 keV [111].

However, from the biological point of view, an energy of around 100 keV to 150 keV gives the minimum of the required penetration depth in tissue for irradiation of deep targets [55]. And from the physical point of view, 100 keV to 150 keV X-rays give the best compromise between a well-defined peak dose profile and a sharp beam penumbra (short electron ranges) [55]. In summary, all compact X-ray sources do not achieve the desired X-ray energy higher than 100 keV except the LFXT. For the MuCLS, technical improvements are required which allow for the generation of higher X-ray energies for preclinical and future clinical trials.

Furthermore, the X-ray energy influences the PVDR which plays an important role in tumor control [54] and increases the therapeutic window [54]. In preclinical experiments at synchrotrons, a PVDR of 20 to 50 is usually applied [55]. This is in agreement with the available PVDR of 15 to 30 at conventional X-ray tubes [110] and of 17 at the CNT X-ray source [104]. However, it contrasts the measured PVDR of about  $210 \pm 20$  at the MuCLS in the *in vivo* study [161]. The increased PVDR can be attributed to almost no scattering material around the target. In addition to the PVDR, the valley dose is also a critical determinant for tumor control [91]. At synchrotrons, tumor growth inhibition could only be shown at a substantial valley dose of 5 Gy to 9 Gy [68] or even higher at 24 Gy [80]. At the MuCLS, a valley dose of 0.2 Gy showed also a trend for tumor inhibition in this doctoral thesis. The reason could be the higher RBE of low-energetic X-rays [162]. The MuCLS produces monochromatic X-rays of 25 keV which are biologically more effective due to a higher LET [162] than synchrotron-generated X-rays in a broader range of different energies peaking at around 70 keV to 120 keV [48,69,91]. At synchrotrons, the biological effectiveness is then mainly conveyed by high-energetic X-rays with a low LET. However, the anti-tumor efficacy of monochromatic low-energetic X-rays at the MuCLS was proven in only one single mouse per treatment group. Therefore, it is necessary to evaluate the tumoricidal effect in a bigger cohort.

In conclusion, the technical settings of compact X-ray sources influence the anti-tumor efficacy due to the relation between dose rate, X-ray energy, PVDR, maximum irradiation time and minimum required lethal tumor dose (valley dose). The technical features of the MuCLS fit a few requirements for MRT such as cost-efficiency and space requirements. However, there are more technical improvements needed in the future in order to increase the dose rate and the X-ray energy at the MuCLS. The implementation of an enlarged linear accelerator or an enlarged storage ring could improve the X-ray energy towards the minimum required energy of 100 keV [161]. Despite that, the tumoricidal effect could even be shown in this doctoral thesis with the current setup of the MuCLS. In the future, the technical requirements of compact X-ray sources for tumor growth inhibition such as X-ray energy and dose rate need to be optimized.

## 4.2 A mouse model for assessment of acute and late normal tissue complications after high-dose irradiation

RT is an integral part of the current treatment strategy of cancer patients [1]. However, conventional treatments induce still severe acute and late side effects in normal tissues [30]. Even after irradiation using modern RT modalities skin toxicities still manifest in 85 % patients [152]. In order to study the benefits of the normal tissue from new treatment modalities (MRT, MBRT), mouse models are of special focus of the current radiobiological research.

In this doctoral thesis, the mouse ear model was used. The thickness of ears of Balb/c mice as an acute marker for swelling increases with increasing dose and resembles also dose-dependently the amount of fibrotic tissue as a late side effect after hypofractionated X-ray RT. Therefore, measuring ear thickness in Balb/c mice can be used as a predictor for radiation-induced fibrosis. With this correlation, the mouse ear model is superior to other mouse models in both quantifying acute and late side effects dose-dependently and predicting late side effects based on the measured severity of early toxicities. The mouse ear model in Balb/c mice contrasts with measuring of the ear thickness in a different mouse strain (C57BL/6J) which did not show a dose-dependency between ear thickness and peak dose after MRT [163]. However, C57BL/6J mice showed an increased amount of TGF $\beta$ 1 over time which correlated with the degree of skin injury and fibrosis 90 days after a 2-fraction RT [164]. The correlation between the amount of TGF $\beta$ 1, acute, and late side effects in the skin does not agree to the results of this doctoral thesis which could be caused by the use of different assays. The measurement of total and active TGF $\beta$ 1 in tissue is more sensitive than the quantification of the amount of TGF $\beta$ 1-expressing cells which does not reflect the amount of TGF $\beta$ 1 expressed by a single cell.

Furthermore, the use of score tables for the evaluation of the severity of skin injuries is commonly used in human and mouse studies. As an example, in CDF1 mice acute skin injuries were scored after irradiation of the food skin by a skin score table [165]. Also, the degree of skin injury was measured in pigs by using a toxicity grading system [166]. However, the ranking of the severity of skin injuries by score tables is a personally subjective, non-quantitative tool for assessment of early side effects. This limitation overcomes the measurement of the ear thickness in the mouse ear model which displays a quantitative tool. There are also other objective tools for evaluation of early side effects such as erythema in patients with psoriasis measuring the coloration of the images according to a digital color code [167,168]. Moreover, this thesis showed that the skin tolerates high X-ray doses of 30 Gy in a hypofractionated regime. This is in agreement with single irradiations of the pig skin which show that tolerated doses of the skin raise up to 30 Gy [166]. Therefore, the use of high-dose fractions (hypofractionation) becomes more relevant for fractionation modalities especially in stereotactic RT [40] using doses from 7.7 Gy to 30 Gy in up to four treatment sessions [169].

Hypofractionation is interesting for spatial fractionation and RT using charged particles. Due to the unique dose deposition profile of both modalities, the normal tissue benefits from an increased sparing effect. The normal tissue-sparing of spatial fractionation (MRT) was demonstrated in a rat skin model at in-beam doses of 835 Gy to 1,335 Gy [123] and in the brain of healthy rats at up to 5,000 Gy [62]. In addition, proton therapy spares the normal tissue more than X-ray therapy due to a reduced dose deposition proximal and especially distal to the tumor [170]. In turn, this means that the proton dose can be raised until the same complication in the shallow normal tissue is detectable as found after X-ray RT. However, it is still lower than the X-ray dose due to the slightly higher RBE of protons [27].

In conclusion, both the dose-dependency and the correlation of acute and late toxicities can be evaluated in the mouse ear model which is therefore superior to other mouse models. The tolerance of the skin against high X-ray doses of 30 Gy was also shown in this mouse model. Therefore, this mouse model is suitable for measuring skin toxicity after high-dose fractions such as it can be delivered in a combined treatment of temporal and spatial fractionation. The influence of a combined temporal and spatial fractionation with protons on the skin toxicity will be investigated in chapter 4.3.

### **4.3 Skin toxicity depend on spatial dose modulation and reirradiation accuracy after hypofractionated pMBRT**

Although several new RT modalities were introduced in the last years, there is still inevitable toxicity in the normal tissue [152]. The reduction of side effects can be achieved in two ways: (1) temporal fractionation splits the total dose into several small doses [39] and (2) spatial fractionation decreases the volume of destroyed cells [39]. In addition, both RT modalities showed an increased anti-tumor efficacy [66,68,69,80,122].

This doctoral thesis questioned whether the reirradiation position of high-dose fractions of proton minibeam influences the severity of side effects in the mouse ear model. Already in 2015, the potential of proton minibeam for a hypofractionated regime was suggested by the group of Dilmanian [127]. They showed the successful implementation of a minibeam collimator at an existing particle beamline and proposed the administration of proton minibeam from the same direction on every other day for lung and liver tumors [127]. When irradiating these tumors, the patient's skin is almost always affected [39]. Therefore, this doctoral thesis is focusing on skin toxicities after hypofractionated pMBRT from the same direction on every day as suggested by Dilmanian [127]. The best overall tissue-sparing measured by the thickness of irradiated ears is achieved when fractions with a high dose modulation were administered with a high reirradiation accuracy (FS1) compared to accurately applied fractions with a low dose modulation (FS3). This data indicates that the low valley dose in FS1 spares the tissue more than the high valley dose in FS3. In agreement with this result are MRT studies showing a valley dose-dependent normal tissue-sparing [92,171]. This is also confirmed for

pMBRT by the irradiation of ears at different valley doses and a constant mean dose [172]. This study of Sammer *et al.* shows a decreased ear thickness with decreasing valley dose [172]. In addition, a high PVDR which increases with decreasing valley dose spares the most the skin [172]. The PVDR was also determined as a critical parameter for the treatment efficacy of MRT [171] and should be as high as possible for normal tissue-sparing [92,173]. Moreover, a shift of highly dose modulated fractions (FS2) leads to intermediate skin toxicity. This can be explained by the generation of an intermediately modulated dose. While FS1 is keeping the valley dose constant after all fractions, FS2 deposits the high peak dose at this position on the ear where the low valley dose was the day before. This leads to a smoothing of dose distribution over time. However, the skin toxicity after FS2 is still gentler than after FS3 since in-beam cells of FS2 can be recovered between each fraction. The recovery of in-beam cells was already suggested in MRT studies showing the migration and proliferation of normal brain cells from the valley to the peak regions in order to replace damaged in-beam cells [87]. Since the skin is a fast proliferating organ [8], the damage is repaired within 24 h [12]. At this time the next fraction is administered.

Moreover, the results of this doctoral thesis show that the ears are thick and the amount of fibrotic tissue is increased at the end of the follow-up period of 150 days. In detail, the amount of fibrotic tissue and the ear thickness are significantly increased after hypofractionated pMBRT with a low dose modulation (FS3), while there was no increased accumulation of fibrotic tissue and no increase in ear thickness on that day after hypofractionated pMBRT with a high dose modulation (FS1). This indicates a correlation between ear thickness and the amount of fibrotic tissue which is in agreement with the correlation of ear thickness and fibrosis after X-ray hypofractionation in the pilot study (chapter 3.2.2). The amount of fibrotic tissue contributes to a chronic increase in ear thickness after hypofractionated pMBRT. This is in line with the results of the pilot study. In addition to massive collagen deposition, chronic inflammation and epidermal hyperplasia can contribute to chronic ear thickness as already shown in the X-ray pilot study.

While this doctoral thesis focused on normal tissue complications, the group of Serduc investigated the anti-tumor efficiency of high-dose fractions of X-ray MRT [126]. The setup irradiating from three different ports [126] is different from that of this doctoral thesis. The lifespan of gliosarcoma-bearing rats could significantly be increased after hypofractionated X-ray MRT [126]. In contrast to protons, X-ray MRT administered from three ports does not irradiate a uniform dose within the tumor [126]. Therefore, the anti-tumor efficacy of hypofractionated pMBRT should be studied in the future.

In conclusion, acute and late toxicities of the skin depend especially on the reirradiation accuracy of a high-dose fraction of pMBRT. This influences the total spatial dose modulation after all four fractions. In the future, the contribution of chronic inflammation and epidermal hyperplasia to ear thickening should be analyzed in irradiated ears. Furthermore, the anti-tumor efficiency of fractionated pMBRT should be evaluated.

## Acknowledgments

I would like to express my special gratitude to Prof. Dr. Stephanie E. Combs for giving me the opportunity to perform my doctoral thesis at the Institute of Radiation Medicine.

I am also very grateful to my primary doctoral advisor, Prof. Dr. Thomas E. Schmid, for supporting me throughout the entire Ph.D. phase, especially during the writing phase. His advice and constant support helped me to further expand my knowledge and to improve myself in scientific work. Thank you for your ongoing interest in my project and for bringing in many helpful ideas if something unexpected happened in my *in vivo* and *in vitro* experiments.

I would also like to especially thank Prof. Dr. Franz Pfeiffer as my second doctoral adviser for his great advice and feedback during the thesis committee meetings. Many thanks also to Prof. Dr. Günther Dollinger and Dr. Daniela Schilling as my thesis committee members for your committed support in all scientific aspects during my Ph.D. phase and valuable discussions during the thesis committee meetings.

Moreover, I want to thank Dr. Karin Burger and Matthias Sammer for their ongoing support and discussion of the data of the animal trials we performed in collaboration. Thanks to Dr. Stefan Bartzsch and Prof. Dr. Jan J. Wilkens for supporting my studies with their physical knowledge and your persistent contribution to the publication of my data.

I also want to thank all my colleagues for their support throughout this entire process. My special thanks go to Marlon Stein, Ann-Kristin Porth, Sandra Bicher, Dr. Katarina Ilicic and my colleagues of the University of the Bundeswehr for their persevering help and incredible support at any time of day and night at any day of the week during the animal experiments in Garching.

Thanks to Dr. Elke Beyreuther for sharing your knowledge on how to implant tumors in mouse ears. Thanks to Dr. Martin Dierolf, Benedikt Günther, Dr. Klaus Achterhold and Dr. Bernhard Gleich for their technical support during the animal experiment at the MuCLS. I also want to thank for their scientific input for fruitful collaboration. I like also to acknowledge Dr. Annette Feuchtinger and Dr. Andreas Blutke for their help in tissue sample processing, analysis, and interpretation of the data.

All my love and thanks for the ongoing support and continuous encouragement provided by my husband and family. Thank you that you were just always there for me and thank you for your open ears which supported me a lot in difficult times.

## List of figures

- Figure 1. Schematic illustration of the dose deposition profile of X-rays (top) and protons (bottom) in a tissue with a tumor (blue cells) located in a depth of 10-15 cm. Radiation in the form of X-rays or protons is generated by an external source on the left (not shown). High radiation energy (dose) is depicted as red, medium energy is orange, and low energy is yellow. Radiation-damaged cells of the tumor and the healthy tissue are marked by a yellow flash. ....3
- Figure 2. Illustration of the biological effectiveness of radiation in dependence of their linear energy transfer (LET). On the left, low LET radiation produces sparsely ionizing events that generate only a low number of reparable DNA lesions. Therefore it has a low biological effectiveness. On the right, high LET radiation ionizes densely the matter within a cell producing a high number of irreparable DNA lesions which lead to a high biological effectiveness.....6
- Figure 3. Principle of immunohistochemical staining of an antigen (blue) on a glass slide (grey) targeted by a primary antibody (green) and a directly labeled secondary antibody (orange). .....23

## Abbreviations

BB	Broadbeam
CLS	Compact Light Source
CNT	Carbon nanotube
ctc	Center-to-center
CTCAE	Common Terminology Criteria for Adverse Events
DAB	3,3'-diamino-benzidine, chromogenic substrate
DSB	DNA double-strand break
DNA	Deoxyribonucleic acid
EBRT	External beam radiotherapy
ESRF	European synchrotron radiation facility
FaDu	An established squamous tumor cell line
FITC	Fluorescein isothiocyanate
FS	Fractionation scheme
GEM	Genetically engineered mouse
GRID	Kind of s spatially fractionated radiotherapy, sieve therapy
H&E	Hematoxylin and eosin
HR	Homologous recombination
H2AX	Histone of the H2A family
ICS	Inverse Compton Scattering Source
IHC	Immunohistochemistry
IR	Ionizing radiation
LET	Linear energy transfer
LFXT	Line focus X-ray tube
LINAC	Linear accelerator
MBRT	Minibeam radiation therapy
MRT	Microbeam radiation therapy



MT	Masson's Trichrome
MuCLS	Beamline at the Compact Light Source in Munich
NHEJ	Non-homologous end-joining
NOD	Non-obese diabetic
NSLS	National Synchrotron Light Source
OH	Hydroxyl group
pMBRT	Proton minibeam radiation therapy
pMRT	Proton microbeam radiation therapy
PVDR	Peak-to-dose valley ratio
RBE	Relative biological effectiveness
RIBE	Radiation-induced bystander effect
RNA	Ribonucleic acid
ROS	Reactive oxygen species
RT	Radiation therapy
SARRP	Small animal radiation research platform
s.c.	Subcutaneous
SCID	Severe combined immunodeficiency
SNAKE	Superconducting Nanoprobe for Applied nuclear (Kern-) physics Experiments
SOBP	Spread-out Bragg peak
SSB	DNA single-strand break
TCD <sub>50</sub>	Tumor control dose 50%
TGD	Tumor growth delay assay
TGFβ	Transforming growth factor beta
TME	Tumor microenvironment
USA	United States of America
XRT	Fractionated radiation therapy
γH2AX	A phosphorylated variant within the histone H2A family

## List of symbols

cm	centimeter
cm <sup>2</sup>	square centimeter
cm <sup>3</sup>	cubic centimeter
Gy	Gray
Gy/min	Gray per minute
Gy/s	Gray per second
h	hour
keV	kiloelectronvolt
keV/ $\mu$	kiloelectronvolt per micrometer
kGy/s	kilogray per second
kVp	kilovolt peak
MeV	megelectronvolt
min	minute
m <sup>2</sup>	square meter
mm	millimeter
mm <sup>3</sup>	cubic millimeter
nm	nanometer
photons/s	photons per second
$\mu$ m	micrometer
°C	centigrade

## References

1. Baskar, R.; Lee, K.A.; Yeo, R.; Yeoh, K.W. Cancer and radiation therapy: current advances and future directions. *International journal of medical sciences* **2012**, *9*, 193-199, doi:10.7150/ijms.3635.
2. Quante, A.S.; Ming, C.; Rottmann, M.; Engel, J.; Boeck, S.; Heinemann, V.; Westphalen, C.B.; Strauch, K. Projections of cancer incidence and cancer-related deaths in Germany by 2020 and 2030. *Cancer medicine* **2016**, *5*, 2649-2656, doi:10.1002/cam4.767. Epub 2016 Jun 29.
3. Durante, M.; Loeffler, J.S. Charged particles in radiation oncology. *Nature Reviews Clinical Oncology* **2009**, *7*, 37, doi:10.1038/nrclinonc.2009.183.
4. Bentzen, S.M. Preventing or reducing late side effects of radiation therapy: radiobiology meets molecular pathology. *Nat Rev Cancer* **2006**, *6*, 702-713, doi:10.1038/nrc1950.
5. Thomadsen, B. *Brachytherapy: Applications and Techniques*, 2nd ed. P Devlin, R Cormack, C Holloway & A Stewart. New York: Demos Medical Publishing, 2016. Hardcover: 576 pp. Price: \$250.00, ISBN 978-1620700822. *Medical Physics* **2017**, *44*, 4981-4981, doi:10.1002/mp.12417.
6. Amaldi, U.; Kraft, G. Radiotherapy with beams of carbon ions. *Rep. Prog. Phys* **2005**, *68*, 1861-1882, doi:10.1088/0034-4885/68/8/R04.
7. Dietrich, A.; Koi, L.; Zöphel, K.; Sihver, W.; Kotzerke, J.; Baumann, M.; Krause, M. Improving external beam radiotherapy by combination with internal irradiation. *The British Journal of Radiology* **2015**, *88*, 20150042, doi:10.1259/bjr.20150042.
8. Hall, E.J. *Radiobiology for the Radiobiologist* 5 ed.; Lippincott Williams & Wilkins: Philadelphia, USA, 0-7817-2649-2.
9. Reisz, J.A.; Bansal, N.; Qian, J.; Zhao, W.; Furdui, C.M. Effects of ionizing radiation on biological molecules--mechanisms of damage and emerging methods of detection. *Antioxid Redox Signal* **2014**, *21*, 260-292, doi:10.1089/ars.2013.5489.
10. Desouky, O.; Ding, N.; Zhou, G. Targeted and non-targeted effects of ionizing radiation. *Journal of Radiation Research and Applied Sciences* **2015**, *8*, 247-254, doi:10.1016/j.jrras.2015.03.003.
11. Trikalinos, T.A.; Terasawa, T.; Ip, S.; Raman, G.; Lau, J. AHRQ Comparative Effectiveness Technical Briefs. In *Particle Beam Radiation Therapies for Cancer*, Agency for Healthcare Research and Quality (US): Rockville (MD), **2009**.
12. Connell, P.P.; Hellman, S. Advances in Radiotherapy and Implications for the Next Century: A Historical Perspective. *Cancer Research* **2009**, *69*, 383-392, doi:10.1158/0008-5472.Can-07-6871.
13. Halperin, E.C. Particle therapy and treatment of cancer. *The Lancet Oncology* **2006**, *7*, 676-685, doi:10.1016/S1470-2045(06)70795-1.
14. Zlobinskaya, O.; Girst, S.; Greubel, C.; Hable, V.; Siebenwirth, C.; Walsh, D.W.; Multhoff, G.; Wilkens, J.J.; Schmid, T.E.; Dollinger, G. Reduced side effects by proton microchannel radiotherapy: study in a human skin model. *Radiat Environ Biophys* **2013**, *52*, 123-133, doi:10.1007/s00411-012-0450-9. Epub 2012 Dec 28.
15. Joiner, M.; Van der Kogel, A. *Basic Clinical Radiobiology* 4 ed.; Hodder Education: London, United Kingdom, 2009; pp. 1-391, 978 0 340 929 667.
16. Newhauser, W.D.; Zhang, R. The physics of proton therapy. *Physics in medicine and biology* **2015**, *60*, R155-R209, doi:10.1088/0031-9155/60/8/r155.
17. Jette, D.; Chen, W. Creating a spread-out Bragg peak in proton beams. *Physics in medicine and biology* **2011**, *56*, N131-N138, doi:10.1088/0031-9155/56/11/n01.
18. Ling, C.C.; Gerweck, L.E.; Zaider, M.; Yorke, E. Dose-rate effects in external beam radiotherapy redux. *Radiotherapy and Oncology* **2010**, *95*, 261-268, doi:10.1016/j.radonc.2010.03.014.

19. Hall, S.; Rudrawar, S.; Zunk, M.; Bernaitis, N.; Arora, D.; McDermott, C.M.; Anoopkumar-Dukie, S. Protection against Radiotherapy-Induced Toxicity. *Antioxidants (Basel, Switzerland)* **2016**, *5*, doi:10.3390/antiox5030022.
20. Marín, A.; Martín, M.; Liñán, O.; Alvarenga, F.; López, M.; Fernández, L.; Büchser, D.; Cerezo, L. Bystander effects and radiotherapy. *Reports of Practical Oncology & Radiotherapy* **2015**, *20*, 12-21, doi:10.1016/j.rpor.2014.08.004.
21. Hubenak, J.R.; Zhang, Q.; Branch, C.D.; Kronowitz, S.J. Mechanisms of injury to normal tissue after radiotherapy: a review. *Plast Reconstr Surg* **2014**, *133*, 49e-56e, doi:10.1097/01.prs.0000440818.23647.0b.
22. Wang, Z.-Z.; Li, W.-J.; Zhang, H.; Yang, J.-S.; Qiu, R.; Wang, X. Comparison of clonogenic assay with premature chromosome condensation assay in prediction of human cell radiosensitivity. *World Journal of Gastroenterology : WJG* **2006**, *12*, 2601-2605, doi:10.3748/wjg.v12.i16.2601.
23. Hanahan, D.; Weinberg, Robert A. Hallmarks of Cancer: The Next Generation. *Cell* **2011**, *144*, 646-674, doi:10.1016/j.cell.2011.02.013.
24. Baskar, R.; Dai, J.; Wenlong, N.; Yeo, R.; Yeoh, K.-W. Biological response of cancer cells to radiation treatment. *Frontiers in Molecular Biosciences* **2014**, *1*, doi:10.3389/fmolb.2014.00024.
25. Willers, H.; Dahm-Daphi, J.; Powell, S.N. Repair of radiation damage to DNA. *Br J Cancer* **2004**, *90*, 1297-1301, doi:10.1038/sj.bjc.6601729.
26. Deriano, L.; Roth, D.B. Modernizing the nonhomologous end-joining repertoire: alternative and classical NHEJ share the stage. *Annual review of genetics* **2013**, *47*, 433-455, doi:10.1146/annurev-genet-110711-155540.
27. Ilicic, K.; Combs, S.E.; Schmid, T.E. New insights in the relative radiobiological effectiveness of proton irradiation. *Radiation oncology (London, England)* **2018**, *13*, 6-6, doi:10.1186/s13014-018-0954-9.
28. Mohamad, O.; Sishc, B.; Saha, J.; Pompos, A.; Rahimi, A.; Story, M.; Davis, A.; Kim, D.W. Carbon Ion Radiotherapy: A Review of Clinical Experiences and Preclinical Research, with an Emphasis on DNA Damage/Repair. *Cancers* **2017**, *9*, 66, doi:10.3390/cancers9060066.
29. Zhang, X.; Ye, C.; Sun, F.; Wei, W.; Hu, B.; Wang, J. Both Complexity and Location of DNA Damage Contribute to Cellular Senescence Induced by Ionizing Radiation. *PloS one* **2016**, *11*, e0155725, doi:10.1371/journal.pone.0155725.
30. Collen, E.B.; Mayer, M.N. Acute effects of radiation treatment: Skin reactions. *The Canadian Veterinary Journal* **2006**, *47*, 931-935.
31. Wang, J.-S.; Wang, H.-J.; Qian, H.-L. Biological effects of radiation on cancer cells. *Mil Med Res* **2018**, *5*, 20-20, doi:10.1186/s40779-018-0167-4.
32. Barnett, G.C.; West, C.M.L.; Dunning, A.M.; Elliott, R.M.; Coles, C.E.; Pharoah, P.D.P.; Burnet, N.G. Normal tissue reactions to radiotherapy: towards tailoring treatment dose by genotype. *Nature reviews. Cancer* **2009**, *9*, 134-142, doi:10.1038/nrc2587.
33. Wynn, T.A. Integrating mechanisms of pulmonary fibrosis. *J Exp Med* **2011**, *208*, 1339-1350, doi:10.1084/jem.20110551.
34. Dracham, C.B.; Shankar, A.; Madan, R. Radiation induced secondary malignancies: a review article. *Radiation oncology journal* **2018**, *36*, 85-94, doi:10.3857/roj.2018.00290.
35. Abughazaleh, R.D.; Tracy, T.S. Therapeutic Index. In *Wiley Encyclopedia of Clinical Trials*, **2007**; doi: 10.1002/9781118445112.stat07121;pp. 1-11.
36. Prezado, Y.; Sarun, S.; Gil, S.; Deman, P.; Bouchet, A.; Le Duc, G. Increase of lifespan for glioma-bearing rats by using minibeam radiation therapy. *Journal of synchrotron radiation* **2012**, *19*, 60-65, doi:10.1107/S0909049511047042. Epub 2011 Nov 25.
37. Withers, H.R. Radiation biology and treatment options in radiation oncology. *Cancer Res* **1999**, *59*, 1676s-1684s.
38. Prasanna, A.; Ahmed, M.M.; Mohiuddin, M.; Coleman, C.N. Exploiting sensitization windows of opportunity in hyper and hypo-fractionated radiation therapy. *Journal of thoracic disease* **2014**, *6*, 287-302, doi:10.3978/j.issn.2072-1439.2014.01.14.

39. Papiez, L.; Timmerman, R. Hypofractionation in radiation therapy and its impact. *Med Phys* **2008**, *35*, 112-118, doi:10.1118/1.2816228.
40. Milano, M.T.; Constine, L.S.; Okunieff, P. Normal tissue toxicity after small field hypofractionated stereotactic body radiation. *Radiation oncology (London, England)* **2008**, *3*, 36-36, doi:10.1186/1748-717X-3-36.
41. Ansel, D.J.; Bravin, A.; Romanelli, P. Microbeam radiosurgery using synchrotron-generated submillimetric beams: a new tool for the treatment of brain disorders. *Neurosurgical Review* **2011**, *34*, 133-142, doi:10.1007/s10143-010-0292-3.
42. Frey, B.; Rückert, M.; Weber, J.; Mayr, X.; Derer, A.; Lotter, M.; Bert, C.; Rödel, F.; Fietkau, R.; Gaipl, U.S. Hypofractionated Irradiation Has Immune Stimulatory Potential and Induces a Timely Restricted Infiltration of Immune Cells in Colon Cancer Tumors. *Frontiers in immunology* **2017**, *8*, 231-231, doi:10.3389/fimmu.2017.00231.
43. Barlow, M.L.; Battaglia, N.; Gerber, S.A.; Lord, E.M. Hypofractionated radiotherapy treatment preserves immune function and improves tumor control vs. hyperfractionated treatment. *The Journal of Immunology* **2016**, *196*, Supplement 213.213.
44. Quinn, T.J.; Hamstra, D. Hypofractionation in Prostate Cancer Using Proton Beam. *International Journal of Radiation Oncology • Biology • Physics* **2019**, *105*, 723-726, doi:10.1016/j.ijrobp.2019.08.006.
45. Asur, R.; Butterworth, K.T.; Penagaricano, J.A.; Prise, K.M.; Griffin, R.J. High dose bystander effects in spatially fractionated radiation therapy. *Cancer Letters* **2015**, *356*, 52-57, doi:10.1016/j.canlet.2013.10.032.
46. Gil, S.; Sarun, S.; Biète, A.; Prezado, Y.; Sabés, M. Survival Analysis of F98 Glioma Rat Cells Following Minibeam or Broad-Beam Synchrotron Radiation Therapy. *Radiation Oncology* **2011**, *6*, 1-9, doi:10.1186/1748-717x-6-37.
47. Grotzer, M.A.; Schültke, E.; Bräuer-Krisch, E.; Laissue, J.A. Microbeam radiation therapy: Clinical perspectives. *Physica Medica* **2015**, *31*, 564-567, doi:10.1016/j.ejmp.2015.02.011.
48. Prezado, Y.; Fois, G.R. Proton-minibeam radiation therapy: a proof of concept. *Med Phys* **2013**, *40*, 031712, doi:10.1118/1.4791648.
49. Sabatasso, S.; Laissue, J.A.; Hlushchuk, R.; Graber, W.; Bravin, A.; Brauer-Krisch, E.; Corde, S.; Blattmann, H.; Gruber, G.; Djonov, V. Microbeam radiation-induced tissue damage depends on the stage of vascular maturation. *Int J Radiat Oncol Biol Phys* **2011**, *80*, 1522-1532, doi:10.1016/j.ijrobp.2011.03.018.
50. Brauer-Krisch, E.; Requardt, H.; Regnard, P.; Corde, S.; Siegbahn, E.; LeDuc, G.; Brochard, T.; Blattmann, H.; Laissue, J.; Bravin, A. New irradiation geometry for microbeam radiation therapy. *Physics in medicine and biology* **2005**, *50*, 3103-3111, doi:10.1088/0031-9155/50/13/009.
51. Ibahim, M.J.; Crosbie, J.C.; Yang, Y.; Zaitseva, M.; Stevenson, A.W.; Rogers, P.A.; Paiva, P. An evaluation of dose equivalence between synchrotron microbeam radiation therapy and conventional broad beam radiation using clonogenic and cell impedance assays. *PloS one* **2014**, *9*, e100547, doi:10.1371/journal.pone.0100547.
52. Guardiola, C.; Prezado, Y.; Roulin, C.; Bergs, J.W.J. Effect of X-ray minibeam radiation therapy on clonogenic survival of glioma cells. *Clin Transl Radiat Oncol* **2018**, *13*, 7-13, doi:10.1016/j.ctro.2018.07.005.
53. Chtcheprov, P.; Burk, L.; Yuan, H.; Inscoe, C.; Ger, R.; Hadsell, M.; Lu, J.; Zhang, L.; Chang, S.; Zhou, O. Physiologically gated microbeam radiation using a field emission x-ray source array. *Med Phys* **2014**, *41*, 081705, doi:10.1118/1.4886015.
54. Livingstone, J.; Stevenson, A.W.; Häusermann, D.; Adam, J.-F. Experimental optimisation of the X-ray energy in microbeam radiation therapy. *Physica Medica: European Journal of Medical Physics* **2018**, *45*, 156-161, doi:10.1016/j.ejmp.2017.12.017.
55. Bartzsch, S.; Corde, S.; Crosbie, J.C.; Day, L.; Donzelli, M.; Krisch, M.; Lerch, M.; Pellicoli, P.; Smyth, L.M.L.; Tehei, M. Technical advances in x-ray microbeam radiation therapy. *Physics in medicine and biology* **2020**, *65*, 02tr01, doi:10.1088/1361-6560/ab5507.

56. Curtis, H.J. The use of a deuteron microbeam for simulating the biological effects of heavy cosmic-ray particles. *Radiat. Res. Suppl* **1967**, *7*, doi:10.2307/3583719.
57. Zeman, W.; Curtis, H.J.; Gebhard, E.L.; Haymaker, W. Tolerance of mouse-brain tissue to high-energy deuterons. *Science (New York, N.Y.)* **1959**, *130*, 1760-1761, doi:10.1126/science.130.3391.1760-a.
58. Martinez-Rovira, I.; Gonzalez, W.; Brons, S.; Prezado, Y. Carbon and oxygen minibeam radiation therapy: An experimental dosimetric evaluation. *Med Phys* **2017**, *44*, 4223-4229, doi:10.1002/mp.12383.
59. Girst, S.; Greubel, C.; Reindl, J.; Siebenwirth, C.; Zlobinskaya, O.; Walsh, D.W.; Ilicic, K.; Aichler, M.; Walch, A.; Wilkens, J.J., *et al.* Proton Minibeam Radiation Therapy Reduces Side Effects in an In Vivo Mouse Ear Model. *Int J Radiat Oncol Biol Phys* **2015**, *95*, 234-241, doi:10.1016/j.ijrobp.2015.10.020.
60. Kundu, M.R.; White, S.M.; Gopalswamy, N.; Lim, J. Millimeter, Microwave, Hard X-Ray, and Soft X-Ray Observations of Energetic Electron Populations in Solar Flares. *The Astrophysical Journal Supplement Series* **1994**, *90*, 599, doi:10.1086/191881.
61. Laissue, J.A.; Blattmann, H.; Slatkin, D.N. Alban Köhler (1874-1947): Erfinder der Gittertherapie. *Zeitschrift für Medizinische Physik* **2012**, *22*, 90-99, doi:10.1016/j.zemedi.2011.07.002.
62. Slatkin, D.N.; Spanne, P.; Dilmanian, F.A.; Gebbers, J.O.; Laissue, J.A. Subacute neuropathological effects on rats of microplanar beams of x-rays from a synchrotron wiggler. *Proc. Natl. Acad. Sci. USA* **1995**, *92*, doi:10.1073/pnas.92.19.8783.
63. Schültke, E.; Balosso, J.; Breslin, T.; Cavaletti, G.; Djonov, V.; Esteve, F.; Grotzer, M.; Hildebrandt, G.; Valdman, A.; Laissue, J. Microbeam radiation therapy - grid therapy and beyond: a clinical perspective. *The British journal of radiology* **2017**, *90*, 20170073-20170073, doi:10.1259/bjr.20170073.
64. Slatkin, D.N.; Spanne, P.; Dilmanian, F.A.; Sandborg, M. Microbeam radiation therapy. *Med Phys* **1992**, *19*, 1395-1400, doi:10.1118/1.596771.
65. Laissue, J.A.; Geiser, G.; Spanne, P.O.; Dilmanian, F.A.; Gebbers, J.O.; Geiser, M.; Wu, X.Y.; Makar, M.S.; Micca, P.L.; Nawrocky, M.M., *et al.* Neuropathology of ablation of rat gliosarcomas and contiguous brain tissues using a microplanar beam of synchrotron-wiggler-generated X rays. *International journal of cancer* **1998**, *78*, 654-660, doi:10.1002/(SICI)1097-0215(19981123)78:5<654::AID-IJC21>3.0.CO;2-L.
66. Bouchet, A.; Serduc, R.; Laissue, J.A.; Djonov, V. Effects of microbeam radiation therapy on normal and tumoral blood vessels. *Physica Medica* **2015**, *31*, 634-641, doi:10.1016/j.ejmp.2015.04.014.
67. Serduc, R.; Christen, T.; Laissue, J.; Farion, R.; Bouchet, A.; Sanden, B.; Segebarth, C.; Brauer-Krisch, E.; Le Duc, G.; Bravin, A., *et al.* Brain tumor vessel response to synchrotron microbeam radiation therapy: a short-term in vivo study. *Physics in medicine and biology* **2008**, *53*, 3609-3622, doi:10.1088/0031-9155/53/13/015.
68. Uyama, A.; Kondoh, T.; Nariyama, N.; Umetani, K.; Fukumoto, M.; Shinohara, K.; Kohmura, E. A narrow microbeam is more effective for tumor growth suppression than a wide microbeam: an in vivo study using implanted human glioma cells. *Journal of synchrotron radiation* **2011**, *18*, 671-678, doi:10.1107/S090904951101185X.
69. Dilmanian, F.A.; Button, T.M.; Le Duc, G.; Zhong, N.; Pena, L.A.; Smith, J.A.; Martinez, S.R.; Bacarian, T.; Tammam, J.; Ren, B., *et al.* Response of rat intracranial 9L gliosarcoma to microbeam radiation therapy. *Neuro-oncology* **2002**, *4*, 26-38, doi:10.1093/neuonc/4.1.26.
70. Laissue, J.A.; Geiser, G.; Spanne, P.O.; Dilmanian, F.A.; Gebbers, J.O.; Geiser, M.; Wu, X.Y.; Makar, M.S.; Micca, P.L.; Nawrocky, M.M., *et al.* Neuropathology of ablation of rat gliosarcomas and contiguous brain tissues using a microplanar beam of synchrotron-wiggler-generated X rays. *Int. J. Cancer* **1998**, *78*, 654-660, doi:10.1002/(SICI)1097-0215(19981123)78:5<654::AID-IJC21>3.0.CO;2-L.
71. Smilowitz, H.M.; Blattmann, H.; Brauer-Krisch, E.; Bravin, A.; Di Michiel, M.; Gebbers, J.O.; Hanson, A.L.; Lyubimova, N.; Slatkin, D.N.; Stepanek, J., *et al.* Synergy of gene-mediated immunoprophylaxis and microbeam radiation therapy for advanced intracerebral rat 9L gliosarcomas. *J Neurooncol* **2006**, *78*, 135-143, doi:10.1007/s11060-005-9094-9.
72. Regnard, P.; Le Duc, G.; Brauer-Krisch, E.; Tropres, I.; Siegbahn, E.A.; Kusak, A.; Clair, C.; Bernard, H.; Dallery, D.; Laissue, J.A., *et al.* Irradiation of intracerebral 9L gliosarcoma by a single array of

- microplanar x-ray beams from a synchrotron: balance between curing and sparing. *Physics in medicine and biology* **2008**, *53*, 861-878, doi:10.1088/0031-9155/53/4/003.
73. Serduc, R.; Bouchet, A.; Brauer-Krisch, E.; Laissue, J.A.; Spiga, J.; Sarun, S.; Bravin, A.; Fonta, C.; Renaud, L.; Boutonnat, J., *et al.* Synchrotron microbeam radiation therapy for rat brain tumor palliation-influence of the microbeam width at constant valley dose. *Physics in medicine and biology* **2009**, *54*, 6711-6724, doi:10.1088/0031-9155/54/21/017.
74. Serduc, R.; van de Looij, Y.; Francony, G.; Verdonck, O.; van der Sanden, B.; Laissue, J.; Farion, R.; Brauer-Krisch, E.; Siegbahn, E.A.; Bravin, A., *et al.* Characterization and quantification of cerebral edema induced by synchrotron x-ray microbeam radiation therapy. *Physics in medicine and biology* **2008**, *53*, 1153-1166, doi:10.1088/0031-9155/53/5/001.
75. Dilmanian, F.A.; Morris, G.M.; Zhong, N.; Bacarian, T.; Hainfeld, J.F.; Kalef-Ezra, J.; Brewington, L.J.; Tammam, J.; Rosen, E.M. Murine EMT-6 Carcinoma: High Therapeutic Efficacy of Microbeam Radiation Therapy. *Radiation Research* **2003**, *159*, 632-641, doi:10.1667/0033-7587(2003)159[0632:MECHTE]2.0.CO;2.
76. Miura, M.; Blattmann, H.; Brauer-Krisch, E.; Bravin, A.; Hanson, A.L.; Nawrocky, M.M.; Micca, P.L.; Slatkin, D.N.; Laissue, J.A. Radiosurgical palliation of aggressive murine SCCVII squamous cell carcinomas using synchrotron-generated X-ray microbeams. *Br J Radiol* **2006**, *79*, 71-75, doi:10.1259/bjr/50464795.
77. Bouchet, A.; Sakakini, N.; El Atifi, M.; Le Clec'h, C.; Brauer, E.; Moisan, A.; Deman, P.; Rihet, P.; Le Duc, G.; Pelletier, L. Early Gene Expression Analysis in 9L Orthotopic Tumor-Bearing Rats Identifies Immune Modulation in Molecular Response to Synchrotron Microbeam Radiation Therapy. *PLoS ONE* **2013**, *8*, e81874, doi:10.1371/journal.pone.0081874.
78. Dilmanian, F.A.; Qu, Y.; Feinendegen, L.E.; Pena, L.A.; Bacarian, T.; Henn, F.A.; Kalef-Ezra, J.; Liu, S.; Zhong, Z.; McDonald, J.W. Tissue-sparing effect of x-ray microplanar beams particularly in the CNS: is a bystander effect involved? *Exp Hematol* **2007**, *35*, 69-77, doi:10.1016/j.exphem.2007.01.014.
79. Slatkin, D.N.; Spanne, P.; Dilmanian, F.A.; Gebbers, J.O.; Laissue, J.A. Subacute neuropathological effects of microplanar beams of x-rays from a synchrotron wiggler. *Proceedings of the National Academy of Sciences* **1995**, *92*, 8783-8787, doi:10.1073/pnas.92.19.8783.
80. Serduc, R.; Christen, T.; Laissue, J.; Farion, R.; Bouchet, A.; Boudewijn van der, S.; Christoph, S.; Elke, B.-K.; Géraldine Le, D.; Alberto, B., *et al.* Brain tumor vessel response to synchrotron microbeam radiation therapy: a short-term in vivo study. *Physics in medicine and biology* **2008**, *53*, 3609, doi:10.1088/0031-9155/53/13/015.
81. Bouchet, A.; Potez, M.; Coquery, N.; Rome, C.; Lemasson, B.; Brauer-Krisch, E.; Remy, C.; Laissue, J.; Barbier, E.L.; Djonov, V., *et al.* Permeability of Brain Tumor Vessels Induced by Uniform or Spatially Microfractionated Synchrotron Radiation Therapies. *Int J Radiat Oncol Biol Phys* **2017**, *98*, 1174-1182, doi:10.1016/j.ijrobp.2017.03.025.
82. Bouchet, A.; Lemasson, B.; Christen, T.; Potez, M.; Rome, C.; Coquery, N.; Le Clec'h, C.; Moisan, A.; Brauer-Krisch, E.; Leduc, G., *et al.* Synchrotron microbeam radiation therapy induces hypoxia in intracerebral gliosarcoma but not in the normal brain. *Radiother Oncol* **2013**, *108*, 143-148, doi:10.1016/j.radonc.2013.05.013. Epub 2013 May 31.
83. Sprung, C.N.; Yang, Y.; Forrester, H.B.; Li, J.; Zaitseva, M.; Cann, L.; Restall, T.; Anderson, R.L.; Crosbie, J.C.; Rogers, P.A. Genome-wide transcription responses to synchrotron microbeam radiotherapy. *Radiat Res* **2012**, *178*, 249-259, doi:10.1667/rr2885.1.
84. Yang, Y.; Swierczak, A.; Ibahim, M.; Paiva, P.; Cann, L.; Stevenson, A.W.; Crosbie, J.C.; Anderson, R.L.; Rogers, P.A.W. Synchrotron microbeam radiotherapy evokes a different early tumor immunomodulatory response to conventional radiotherapy in EMT6.5 mammary tumors. *Radiotherapy and Oncology* **2019**, *133*, 93-99, doi:10.1016/j.radonc.2019.01.006.
85. Ibahim, M.J.; Yang, Y.; Crosbie, J.C.; Stevenson, A.; Cann, L.; Paiva, P.; Rogers, P.A. Eosinophil-Associated Gene Pathways but not Eosinophil Numbers are Differentially Regulated between Synchrotron Microbeam Radiation Treatment and Synchrotron Broad-Beam Treatment by 48 Hours Postirradiation. *Radiat Res* **2016**, *185*, 60-68, doi:10.1667/rr14115.1.
86. Prise, K.M.; Schettino, G.; Vojnovic, B.; Belyakov, O.; Shao, C. Microbeam studies of the bystander response. *Journal of radiation research* **2009**, *50 Suppl A*, A1-A6, doi:10.1269/jrr.09012s.

87. Dilmanian, F.A.; Qu, Y.; Feinendegen, L.E.; Peña, L.A.; Bacarian, T.; Henn, F.A.; Kalef-Ezra, J.; Liu, S.; Zhong, Z.; McDonald, J.W. Tissue-sparing effect of x-ray microplanar beams particularly in the CNS: Is a bystander effect involved? *Experimental Hematology* **2007**, *35*, 69-77, doi:10.1016/j.exphem.2007.01.014.
88. Lyng, F.M.; Seymour, C.B.; Mothersill, C. Production of a signal by irradiated cells which leads to a response in unirradiated cells characteristic of initiation of apoptosis. *Br J Cancer* **2000**, *83*, 1223-1230, doi:10.1054/bjoc.2000.1433.
89. Prise, K.M.; Belyakov, O.V.; Folkard, M.; Michael, B.D. Studies of bystander effects in human fibroblasts using a charged particle microbeam. *Int J Radiat Biol* **1998**, *74*, 793-798, doi:10.1080/095530098141087.
90. Fernandez-Palomo, C.; Schultke, E.; Smith, R.; Brauer-Krisch, E.; Laissue, J.; Schroll, C.; Fazzari, J.; Seymour, C.; Mothersill, C. Bystander effects in tumor-free and tumor-bearing rat brains following irradiation by synchrotron X-rays. *Int J Radiat Biol* **2013**, *89*, 445-453, doi:10.3109/09553002.2013.766770. Epub 2013 Feb 26.
91. Prezado, Y.; Thengumpallil, S.; Renier, M.; Bravin, A. X-ray energy optimization in minibeam radiation therapy. *Med. Phys* **2009**, *36*, doi:10.1118/1.3232000.
92. Brauer-Krisch, E.; Serduc, R.; Siegbahn, E.A.; Le Duc, G.; Prezado, Y.; Bravin, A.; Blattmann, H.; Laissue, J.A. Effects of pulsed, spatially fractionated, microscopic synchrotron X-ray beams on normal and tumoral brain tissue. *Mutation research* **2010**, *704*, 160-166, doi:10.1016/j.mrrev.2009.12.003.
93. Dilmanian, F.A.; Zhong, Z.; Bacarian, T.; Benveniste, H.; Romanelli, P.; Wang, R.; Welwart, J.; Yuasa, T.; Rosen, E.M.; Ansel, D.J. Interlaced X-ray microplanar beams: a radiosurgery approach with clinical potential. *Proc. Natl. Acad. Sci. USA* **2006**, *103*, doi:10.1073/pnas.0603567103.
94. Gil, S.; Sarun, S.; Biete, A.; Prezado, Y.; Sabés, M. Survival Analysis of F98 Glioma Rat Cells Following Minibeam or Broad-Beam Synchrotron Radiation Therapy. *Radiation Oncology* **2011**, *6*, 37, doi:10.1186/1748-717x-6-37.
95. Bartzsch, S.; Oelfke, U. Line focus x-ray tubes-a new concept to produce high brilliance x-rays. *Phys Med Biol* **2017**, *62*, 8600-8615, doi:10.1088/1361-6560/aa910b.
96. Zhang, L.; Yuan, H.; Burk, L.M.; Inscoe, C.R.; Hadsell, M.J.; Chtcheprov, P.; Lee, Y.Z.; Lu, J.; Chang, S.; Zhou, O. Image-guided microbeam irradiation to brain tumour bearing mice using a carbon nanotube x-ray source array. *Physics in medicine and biology* **2014**, *59*, 1283-1303, doi:10.1088/0031-9155/59/5/1283. Epub 2014 Feb 20.
97. Kellerer, A.M. Electron Spectra and the RBE of X Rays. *Radiation Research* **2002**, *158*, 13-22, doi:10.1667/0033-7587(2002)158[0013:esatro]2.0.co;2.
98. Fournier, P.; Cornelius, I.; Donzelli, M.; Requardt, H.; Nemoz, C.; Petasecca, M.; Brauer-Krisch, E.; Rosenfeld, A.; Lerch, M. X-Tream quality assurance in synchrotron X-ray microbeam radiation therapy. *Journal of synchrotron radiation* **2016**, *23*, 1180-1190, doi:10.1107/s1600577516009322.
99. Dilmanian, F.A.; Qu, Y.; Liu, S.; Cool, C.D.; Gilbert, J.; Hainfeld, J.F.; Kruse, C.A.; Latterra, J.; Lenihan, D.; Nawrocky, M.M., et al. X-ray microbeams: Tumor therapy and central nervous system research. *Nucl Instrum Methods Phys Res A* **2005**, *548*, 30-37, doi:10.1016/j.nima.2005.03.062.
100. Wright, M. Microbeam radiosurgery: An industrial perspective. *Physica Medica* **2015**, *7*, doi:10.1016/j.ejmp.2015.04.003.
101. Donzelli, M.; Bräuer-Krisch, E.; Nemoz, C.; Brochard, T.; Oelfke, U. Conformal image-guided microbeam radiation therapy at the ESRF biomedical beamline ID17. **2016**, *43*, 3157-3167, doi:10.1118/1.4950724.
102. Serduc, R.; Brauer-Krisch, E.; Siegbahn, E.A.; Bouchet, A.; Pouyatos, B.; Carron, R.; Pannetier, N.; Renaud, L.; Berruyer, G.; Nemoz, C., et al. High-precision radiosurgical dose delivery by interlaced microbeam arrays of high-flux low-energy synchrotron X-rays. *PloS one* **2010**, *5*, e9028, doi:10.1371/journal.pone.0009028.
103. Bräuer-Krisch, E.; Adam, J.-F.; Alagoz, E.; Bartzsch, S.; Crosbie, J.; DeWagter, C.; Dipuglia, A.; Donzelli, M.; Doran, S.; Fournier, P., et al. Medical physics aspects of the synchrotron radiation therapies: Microbeam radiation therapy (MRT) and synchrotron stereotactic radiotherapy (SSRT). *Physica Medica* **2015**, *31*, 568-583, doi:10.1016/j.ejmp.2015.04.016.



104. Hadsell, M.; Zhang, J.; Laganis, P.; Sprenger, F.; Shan, J.; Zhang, L.; Burk, L.; Yuan, H.; Chang, S.; Lu, J., *et al.* A first generation compact microbeam radiation therapy system based on carbon nanotube X-ray technology. *Applied physics letters* **2013**, *103*, 183505, doi:10.1063/1.4826587.
105. Anschel, D.J.; Romanelli, P.; Benveniste, H.; Foerster, B.; Kalef-Ezra, J.; Zhong, Z.; Dilmanian, F.A. Evolution of a focal brain lesion produced by interlaced microplanar X-rays. *Minimally invasive neurosurgery : MIN* **2007**, *50*, 43-46, doi:10.1055/s-2007-976514.
106. Sedor, J. Neutron Sources and Synchrotrons. In *In International Partnerships in Large Science Projects*, DIANE Publishing: **1998**; pp. 86-92.
107. Donzelli, M.; Bräuer-Krisch, E.; Nemoz, C.; Brochard, T.; Oelfke, U. Conformal image-guided microbeam radiation therapy at the ESRF biomedical beamline ID17. *Medical Physics* **2016**, *43*, 3157-3167, doi:10.1118/1.4950724.
108. Wu, J.; Hei, T.K. Focus small to find big - the microbeam story. *International journal of radiation biology* **2018**, *94*, 782-788, doi:10.1080/09553002.2017.1364801.
109. Jacquet, M.; Suortti, P. Radiation therapy at compact Compton sources. *Phys Med* **2015**, *31*, 596-600, doi:10.1016/j.ejmp.2015.02.010.
110. Bartzsch, S.; Cummings, C.; Eismann, S.; Oelfke, U. A preclinical microbeam facility with a conventional x-ray tube. *Medical physics* **2016**, *43*, 6301-6308, doi:10.1118/1.4966032.
111. Eggl, E.; Dierolf, M.; Achterhold, K.; Jud, C.; Gunther, B.; Braig, E.; Gleich, B.; Pfeiffer, F. The Munich Compact Light Source: initial performance measures. *Journal of synchrotron radiation* **2016**, *23*, 1137-1142, doi:10.1107/s160057751600967x.
112. Burger, K.; Ilicic, K.; Dierolf, M.; Gunther, B.; Walsh, D.W.M.; Schmid, E.; Eggl, E.; Achterhold, K.; Gleich, B.; Combs, S.E., *et al.* Increased cell survival and cytogenetic integrity by spatial dose redistribution at a compact synchrotron X-ray source. *PloS one* **2017**, *12*, e0186005, doi:10.1371/journal.pone.0186005.
113. Yuan, H.; Zhang, L.; Frank, J.E.; Inscoe, C.R.; Burk, L.M.; Hadsell, M.; Lee, Y.Z.; Lu, J.; Chang, S.; Zhou, O. Treating Brain Tumor with Microbeam Radiation Generated by a Compact Carbon-Nanotube-Based Irradiator: Initial Radiation Efficacy Study. *Radiat Res* **2015**, *184*, 322-333, doi:10.1667/rr13919.1.
114. Zhang, L.; Yuan, H.; Inscoe, C.; Chtcheprov, P.; Hadsell, M.; Lee, Y.; Lu, J.; Chang, S.; Zhou, O. Nanotube x-ray for cancer therapy: a compact microbeam radiation therapy system for brain tumor treatment. *Expert review of anticancer therapy* **2014**, *14*, 1411-1418, doi:10.1586/14737140.2014.978293.
115. Peucelle, C.; Nauraye, C.; Patriarca, A.; Hierso, E.; Fournier-Bidoz, N.; Martínez-Rovira, I.; Prezado, Y. Proton minibeam radiation therapy: Experimental dosimetry evaluation. *Medical Physics* **2015**, *42*, 7108-7113, doi:10.1118/1.4935868.
116. Burns, F.J.; Albert, R.E.; Bennett, P.; Sinclair, I.P. Tumor Incidence in Rat Skin after Proton Irradiation in a Sieve Pattern. *Radiation Research* **1972**, *50*, 181-190, doi:10.2307/3573477.
117. Girst, S.; Greubel, C.; Reindl, J.; Siebenwirth, C.; Zlobinskaya, O.; Dollinger, G.; Schmid, T.E. The influence of the channel size on the reduction of side effects in microchannel proton therapy. *Radiat Environ Biophys* **2015**, *54*, 335-342, doi:10.1007/s00411-015-0600-y. Epub 2015 May 9.
118. Girst, S.; Marx, C.; Brauer-Krisch, E.; Bravin, A.; Bartzsch, S.; Oelfke, U.; Greubel, C.; Reindl, J.; Siebenwirth, C.; Zlobinskaya, O., *et al.* Improved normal tissue protection by proton and X-ray microchannels compared to homogeneous field irradiation. *Phys Med* **2015**, *31*, 615-620, doi:10.1016/j.ejmp.2015.04.004. Epub 2015 Apr 27.
119. Girst, S.; Greubel, C.; Reindl, J.; Siebenwirth, C.; Zlobinskaya, O.; Walsh, D.W.; Ilicic, K.; Aichler, M.; Walch, A.; Wilkens, J.J., *et al.* Proton Minibeam Radiation Therapy Reduces Side Effects in an In Vivo Mouse Ear Model. *Int J Radiat Oncol Biol Phys* **2016**, *95*, 234-241, doi:10.1016/j.ijrobp.2015.10.020
120. Sammer, M.; Teiluf, K.; Girst, S.; Greubel, C.; Reindl, J.; Ilicic, K.; Walsh, D.W.M.; Aichler, M.; Walch, A.; Combs, S.E., *et al.* Beam size limit for pencil minibeam radiotherapy determined from side effects in an in-vivo mouse ear model. *PloS one* **2019**, *14*, e0221454-e0221454, doi:10.1371/journal.pone.0221454.

121. Sammer, M.; Greubel, C.; Girst, S.; Dollinger, G. Optimization of beam arrangements in proton minibeam radiotherapy by cell survival simulations. *Med Phys* **2017**, *44*, 6096-6104, doi:10.1002/mp.12566.
122. Prezado, Y.; Jouvion, G.; Patriarca, A.; Nauraye, C.; Guardiola, C.; Juchaux, M.; Lamirault, C.; Labiod, D.; Jourdain, L.; Sebric, C., *et al.* Proton minibeam radiation therapy widens the therapeutic index for high-grade gliomas. *Scientific Reports* **2018**, *8*, 16479, doi:10.1038/s41598-018-34796-8.
123. Zhong, N.; Morris, G.M.; Bacarian, T.; Rosen, E.M.; Avraham Dilmanian, F. Response of Rat Skin to High-Dose Unidirectional X-Ray Microbeams: A Histological Study. *Radiation Research* **2003**, *160*, 133-142, doi:10.1667/3033.
124. Schültke, E.; Juurlink, B.H.; Ataelmannan, K.; Laissue, J.; Blattmann, H.; Brauer-Krisch, E.; Bravin, A.; Minczewska, J.; Crosbie, J.; Taherian, H., *et al.* Memory and survival after microbeam radiation therapy. *European journal of radiology* **2008**, *68*, S142-146, doi:10.1016/j.ejrad.2008.04.051.
125. Henry, T.; Ureba, A.; Valdman, A.; Siegbahn, A. Proton Grid Therapy. *Technology in Cancer Research & Treatment* **2016**, *0*, doi:10.1177/1533034616681670.
126. Serduc, R.; Brauer-Krisch, E.; Bouchet, A.; Renaud, L.; Brochard, T.; Bravin, A.; Laissue, J.A.; Le Duc, G. First trial of spatial and temporal fractionations of the delivered dose using synchrotron microbeam radiation therapy. *Journal of synchrotron radiation* **2009**, *16*, 587-590, doi:10.1107/s0909049509012485.
127. Dilmanian, F.A.; Eley, J.G.; Krishnan, S. Minibeam therapy with protons and light ions: physical feasibility and potential to reduce radiation side effects and to facilitate hypofractionation. *Int J Radiat Oncol Biol Phys* **2015**, *92*, 469-474, doi:10.1016/j.ijrobp.2015.01.018.
128. Donzelli, M.; Oelfke, U.; Brauer-Krisch, E. Introducing the concept of spiral microbeam radiation therapy (spiralMRT). *Physics in medicine and biology* **2019**, *64*, 065005, doi:10.1088/1361-6560/aaff23.
129. Demidenko, E. Three endpoints of in vivo tumour radiobiology and their statistical estimation. *International journal of radiation biology* **2010**, *86*, 164-173, doi:10.3109/09553000903419304.
130. Teicher, B.A. Tumor models for efficacy determination. *Molecular Cancer Therapeutics* **2006**, *5*, 2435-2443, doi:10.1158/1535-7163.Mct-06-0391.
131. Begg, A.C. Analysis of growth delay data: potential pitfalls. *Br J Cancer Suppl* **1980**, *4*, 93-97.
132. Hill, R.P.; Milas, L. The proportion of stem cells in murine tumors. *International Journal of Radiation Oncology\*Biophysics* **1989**, *16*, 513-518, doi:10.1016/0360-3016(89)90353-2.
133. Trott, K.R. Tumour stem cells: the biological concept and its application in cancer treatment. *Radiotherapy and Oncology* **1994**, *30*, 1-5, doi:10.1016/0167-8140(94)90002-7.
134. Baumann, M.; Krause, M.; Hill, R. Exploring the role of cancer stem cells in radioresistance. *Nat Rev Cancer* **2008**, *8*, 545-554, doi:10.1038/nrc2419.
135. Rofstad, E.K. Local Tumor Control following Single Dose Irradiation of Human Melanoma Xenografts: Relationship to Cellular Radiosensitivity and Influence of an Immune Response by the Athymic Mouse. *Cancer Research* **1989**, *49*, 3163-3167.
136. Krause, M.; Dubrovskaya, A.; Linge, A.; Baumann, M. Cancer stem cells: Radioresistance, prediction of radiotherapy outcome and specific targets for combined treatments. *Advanced Drug Delivery Reviews* **2017**, *109*, 63-73, doi:10.1016/j.addr.2016.02.002.
137. Sanmamed, M.F.; Chester, C.; Melero, I.; Kohrt, H. Defining the optimal murine models to investigate immune checkpoint blockers and their combination with other immunotherapies. *Ann Oncol* **2016**, *27*, 1190-1198, doi:10.1093/annonc/mdw041.
138. Richmond, A.; Su, Y. Mouse xenograft models vs GEM models for human cancer therapeutics. *Disease Models & Mechanisms* **2008**, *1*, 78-82, doi:10.1242/dmm.000976.
139. Okada, S.; Vaeteewoottacharn, K.; Kariya, R. Application of Highly Immunocompromised Mice for the Establishment of Patient-Derived Xenograft (PDX) Models. *Cells* **2019**, *8*, 889, doi:10.3390/cells8080889.

140. Murgai, M.; Giles, A.; Kaplan, R. Physiological, Tumor, and Metastatic Niches: Opportunities and Challenges for Targeting the Tumor Microenvironment. *Crit Rev Oncog* **2015**, *20*, 301-314, doi:10.1615/critrevoncog.2015013668.
141. Fridman, R.; Benton, G.; Aranoutova, I.; Kleinman, H.K.; Bonfil, R.D. Increased initiation and growth of tumor cell lines, cancer stem cells and biopsy material in mice using basement membrane matrix protein (Cultrex or Matrigel) co-injection. *Nature Protocols* **2012**, *7*, 1138-1144, doi:10.1038/nprot.2012.053.
142. Chan, J.K.C. The Wonderful Colors of the Hematoxylin–Eosin Stain in Diagnostic Surgical Pathology. *International Journal of Surgical Pathology* **2014**, *22*, 12-32, doi:10.1177/1066896913517939.
143. Duraiyan, J.; Govindarajan, R.; Kaliyappan, K.; Palanisamy, M. Applications of immunohistochemistry. *J Pharm Bioallied Sci* **2012**, *4*, S307-S309, doi:10.4103/0975-7406.100281.
144. Kalyuzhny, A.E. *Immunohistochemistry*, Nature, S. ed.; 2016; 978-3-319-30891-3.
145. Ivashkevich, A.; Redon, C.E.; Nakamura, A.J.; Martin, R.F.; Martin, O.A. Use of the  $\gamma$ -H2AX assay to monitor DNA damage and repair in translational cancer research. *Cancer Letters* **2012**, *327*, 123-133, doi:10.1016/j.canlet.2011.12.025.
146. Gieringer, M.; Gosepath, J.; Naim, R. Radiotherapy and wound healing: principles, management and prospects (review). *Oncology reports* **2011**, *26*, 299-307, doi:10.3892/or.2011.1319.
147. Singh, M.; Alavi, A.; Wong, R.; Akita, S. Radiodermatitis: A Review of Our Current Understanding. *American Journal of Clinical Dermatology* **2016**, *17*, 277-292, doi:10.1007/s40257-016-0186-4.
148. Matthews, N.H.; Moustafa, F.; Kaskas, N.M.; Robinson-Bostom, L.; Pappas-Tauffer, L. *41 - Dermatologic Toxicities of Anticancer Therapy*; Saunders: Philadelphia, 2020; pp. 621-648, 9781455728657
149. Mendelsohn, F.A.; Divino, C.M.; Reis, E.D.; Kerstein, M.D. Wound Care After Radiation Therapy. *Advances in Skin & Wound Care* **2002**, *15*, 216-224, doi:10.1097/00129334-200209000-00007.
150. Martin, M.T.; Vulin, A.; Hendry, J.H. Human epidermal stem cells: Role in adverse skin reactions and carcinogenesis from radiation. *Mutation Research/Reviews in Mutation Research* **2016**, *770*, 349-368, doi:10.1016/j.mrrev.2016.08.004.
151. Ryan, J.L. Ionizing radiation: the good, the bad, and the ugly. *The Journal of investigative dermatology* **2012**, *132*, 985-993, doi:10.1038/jid.2011.411.
152. Bray, F.N.; Simmons, B.J.; Wolfson, A.H.; Nouri, K. Acute and Chronic Cutaneous Reactions to Ionizing Radiation Therapy. *Dermatol Ther (Heidelb)* **2016**, *6*, 185-206, doi:10.1007/s13555-016-0120-y.
153. Hegedus, F.; Mathew, L.M.; Schwartz, R.A. Radiation dermatitis: an overview. *International journal of dermatology* **2017**, *56*, 909-914, doi:10.1111/ijd.13371.
154. Assaw, S. The use of modified Massion's trichrome staining in collagen evaluation in wound healing study. *Malaysian Journal of Veterinary research* **2012**, *3*, 39-47.
155. Lattouf, R.; Younes, R.; Lutomski, D.; Naaman, N.; Godeau, G.; Senni, K.; Changotade, S. Picrosirius Red Staining: A Useful Tool to Appraise Collagen Networks in Normal and Pathological Tissues. *Journal of Histochemistry & Cytochemistry* **2014**, *62*, 751-758, doi:10.1369/0022155414545787.
156. Constantine, V.S.; Mowry, R.W. Selective staining of human dermal collagen. I. An analysis of standard methods. *J Invest Dermatol* **1968**, *50*, 414-418, doi:10.1038/jid.1968.67.
157. Costa, G.; Araujo, S.; Xavier Júnior, F.; Morais, G.; Silveira, J.; Viana, D.; Evangelista, J. PICROSIRIUS RED AND MASSON'S TRICHROME STAINING TECHNIQUES AS TOOLS FOR DETECTION OF COLLAGEN FIBERS IN THE SKIN OF DOGS WITH ENDOCRINE DERMATOPATHOLOGIES. *Ciência Animal Brasileira* **2019**, *20*, doi:10.1590/1089-6891v20e-55398.
158. Avraham, T.; Yan, A.; Zampell, J.C.; Daluvoy, S.V.; Haimovitz-Friedman, A.; Cordeiro, A.P.; Mehrara, B.J. Radiation therapy causes loss of dermal lymphatic vessels and interferes with lymphatic function by TGF-beta1-mediated tissue fibrosis. *American journal of physiology. Cell physiology* **2010**, *299*, C589-605, doi:10.1152/ajpcell.00535.2009.
159. Huggenberger, R.; Detmar, M. The Cutaneous Vascular System in Chronic Skin Inflammation. *Journal of Investigative Dermatology Symposium Proceedings* **2011**, *15*, 24-32, doi:10.1038/jidsymp.2011.5.

160. Beyreuther, E.; Bruchner, K.; Krause, M.; Schmidt, M.; Szabo, R.; Pawelke, J. An optimized small animal tumour model for experimentation with low energy protons. *PLoS one* **2017**, *12*, e0177428, doi:10.1371/journal.pone.0177428
161. Burger, K. Microbeam Radiation Therapy at a Compact Synchrotron X-ray Source. PhD thesis, Technical University of Munich **2017**.
162. Hill, M.A. The variation in biological effectiveness of X-rays and gamma rays with energy. *Radiat Prot Dosimetry* **2004**, *112*, 471-481, doi:10.1093/rpd/nch091.
163. Potez, M.; Bouchet, A.; Wagner, J.; Donzelli, M.; Brauer-Krisch, E.; Hopewell, J.W.; Laissue, J.; Djonov, V. Effects of Synchrotron X-Ray Micro-beam Irradiation on Normal Mouse Ear Pinnae. *Int J Radiat Oncol Biol Phys* **2018**, *101*, 680-689, doi:10.1016/j.ijrobp.2018.02.007.
164. Kumar, S.; Kolozsvary, A.; Kohl, R.; Lu, M.; Brown, S.; Kim, J.H. Radiation-induced skin injury in the animal model of scleroderma: implications for post-radiotherapy fibrosis. *Radiation oncology (London, England)* **2008**, *3*, 40-40, doi:10.1186/1748-717X-3-40.
165. Sørensen, B.S.; Horsman, M.R.; Alsner, J.; Overgaard, J.; Durante, M.; Scholz, M.; Friedrich, T.; Bassler, N. Relative biological effectiveness of carbon ions for tumor control, acute skin damage and late radiation-induced fibrosis in a mouse model. *Acta Oncologica* **2015**, *54*, 1623-1630, doi:10.3109/0284186X.2015.1069890.
166. Kim, J.W.; Lee, D.W.; Choi, W.H.; Jeon, Y.R.; Kim, S.H.; Cho, H.; Lee, E.J.; Hong, Z.Y.; Lee, W.J.; Cho, J. Development of a porcine skin injury model and characterization of the dose-dependent response to high-dose radiation. *J Radiat Res* **2013**, *54*, 823-831, doi:10.1093/jrr/rrt016.
167. Choi, J.W.; Kwon, S.H.; Youn, J.I.; Youn, S.W. Objective measurements of erythema, elasticity and scale could overcome the inter- and intra-observer variations of subjective evaluations for psoriasis severity. *European journal of dermatology : EJD* **2013**, *23*, 224-229, doi:10.1684/ejd.2013.1931.
168. Raina, A.; Hennessy, R.; Rains, M.; Allred, J.; Hirshburg, J.M.; Diven, D.G.; Markey, M.K. Objective measurement of erythema in psoriasis using digital color photography with color calibration. *Skin research and technology : official journal of International Society for Bioengineering and the Skin (ISBS) [and] International Society for Digital Imaging of Skin (ISDIS) [and] International Society for Skin Imaging (ISSI)* **2016**, *22*, 375-380, doi:10.1111/srt.12276.
169. Blomgren, H.; Lax, I.; Näslund, I.; Svanström, R. Stereotactic High Dose Fraction Radiation Therapy of Extracranial Tumors Using An Accelerator: Clinical experience of the first thirty-one patients. *Acta Oncologica* **1995**, *34*, 861-870, doi:10.3109/02841869509127197.
170. DeLaney, T.F. Proton therapy in the clinic. *Frontiers of radiation therapy and oncology* **2011**, *43*, 465-485, doi:10.1159/000322511.
171. Duncan, M.; Donzelli, M.; Pelliccioli, P.; Brauer-Krisch, E.; Davis, J.A.; Lerch, M.L.F.; Rosenfeld, A.B.; Petasecca, M. First experimental measurement of the effect of cardio-synchronous brain motion on the dose distribution during microbeam radiation therapy. *Medical Physics* 10.1002/mp.13899, doi:10.1002/mp.13899.
172. Sammer, M.; Zahnbrecher, E.; Dobiash, S.; Girst, S.; Greubel, C.; Ilicic, K.; Reindl, J.; Schwarz, B.; Siebenwirth, C.; Walsh, D.W.M., *et al.* Proton pencil minibeam irradiation of an in-vivo mouse ear model spares healthy tissue dependent on beam size. *PLoS one* **2019**, *14*, e0224873, doi:10.1371/journal.pone.0224873.
173. Prezado, Y.; Renier, M.; Bravin, A. A new method of creating minibeam patterns for synchrotron radiation therapy: a feasibility study. *J. Synchrotron Rad* **2009**, *16*, doi:10.1107/s0909049509012503.